ANTENNAS AND PROPAGATION FOR BODY AREA NETWORKS AT 60 GHZ

by

XIANYUE WU

A thesis submitted to
the University of Birmingham
for the degree of
DOCTOR OF PHILOSOPHY

School of Electronic, Electrical & Computer Engineering
College of Engineering and Physical Sciences
University of Birmingham
September 2013

ABSTRACT

The advent of wireless body area networks (WBANs) and their use in a wide range of applications from consumer electronics to military purposes, dictates the need to investigate to the behaviour of antennas and wave propagation on the body in depth. Although this area has been extensively studied in the past decade, some issues are still not satisfactorily solved for communication systems for WBANs at ISM bands and UWB such as compact and high efficiency antenna design, privacy and security, interference mitigation and achieving high data rates. This thesis proposed an alternative wireless solution for body area networks by adopting 60 GHz radio. On-body channels at 60 GHz have been characterised using monopole and horn antennas. Horn antennas achieve significantly improved path gain in the stable channels but are susceptible to shadowing in the mobile channels due to body movements. However, interference mitigation and covertness for 60 GHz WBANs at the physical layer are improved due to high attenuation of 60 GHz signals. Significant increase of carrier-to-interference ratio is observed for 60 GHz WBANs compared to 2.45 GHz. A model of estimating the maximum detection distance at a threshold probability for detecting a WBAN wearing soldier in a battlefield is proposed. Fixed-beam directional antennas and reconfigurable antennas are designed for 60 GHz WBANs and channel measurements using these antennas are conducted. Results show beam-reconfigurability of the antenna improves the link performance compared to fixed-beam antennas at 60 GHz.

To My Parents

ACKNOWLEDGEMENTS

My first debt of gratitude must go to my supervisors Professor Peter S. Hall and Dr. Costas Constantinou. They patiently provided the vision, encouragement and advice necessary for me to proceed through the doctoral program and complete my thesis. I want to thank them for their unflagging encouragement and serving as role models to me as a junior member of academia.

I had a great opportunity to visit the University of Virginia as a part of my PhD. The whole experience was unique and I would like to acknowledge Professor John Lach for his great advice.

I would like to thank examiners of my thesis, Professor William Scanlon and Dr. Alexandros Feresidis, for their time and feedback on my work.

I would also like to express my deep gratitude to my colleague, Dr. Yuriy I. Nechayev, who has been very supportive and generous in sharing his knowledge. I am very greatful to Mr. Alan Yates for providing all the technical support. Special thanks to my other brilliant colleagues and very nice friends, Dr. Zhengpeng Wang, Dr. Lida Akhoonzadeh-Asl, Dr. Mohammad Hmaid, Dr. Zhenhua Hu, Mr. Xiao Li, Mr. Philip Asare from the

University of Virginia and Dr. Nacer Chahat from the University of Renne 1 for their kind help and friendship.

I also want to thank Engineering and Physical Sciences Research Council for providing me the opportunity and partial funding to pursue my PhD degree.

Last but not least, I would like to thank my beloved parents, for their endless support, love and understanding.

ACRONYMS

AFD	Average Fade Duration
BAN	Body Area Network
BSN	Body Sensor Network
CDF	Cumulative Distribution Function
CIR	Carrier to Interference Ratio
DOA	Direction Of Arrival
DRA	Dielectric Resonator Antenna
DSSS	Direct Sequence Spread Spectrum
EBG	Electromagnetic Band Gap
ECG	Electrocardiography
EEG	Electroencephalography
EMG	Electromyography
FCC	Federal Communications Commission
FDA	Food and Drug Administration
FDTD	Finite Difference Time Domain
FHSS	Frequency-Hopping Spread Spectrum
ISM	Industrial Scientific and Medical

LCR	Level Crossing Rate
LOS	Line Of Sight
LTCC	Low Temperature Co-fired Ceramic
MBAN	Medical Body Area Network
MEMS	Microelectromechanical System
MICS	Medical Implant Communication Service
NBI	Narrowband Interference
NLOS	Non Line Of Sight
OMT	Orthomode Transducer
PCB	Printed Circuit Board
pdf	Probability Density Function
PDP	Power Delay Profile
PIFA	Planar Inverted-F Antenna
ROC	Receiver Operating Characteristic
RSSI	Received Signal Strength Indicator
RMS	Root Mean Square
SAR	Radiation Absorption Rate
SINR	Signal to Interference plus Noise Ratio
SIW	Substrate Integrated Waveguide
SNR	Signal to Noise Ratio
UWB	Ultra-wide Band
VNA	Vector Network Analyser
WBAN	Wireless Body Area Network
WLAN	Wireless Local Area Network

CONTENTS

List of Figures

List of Tables

Chapter 1

Introduction

1.1 Introduction to Body Area Networks

The rapid growth in low-power integrated circuits, miniaturization of electronic devices and their computing capability, combined with advanced mobile and personal wireless communications systems has enabled the creation of wireless body area network (WBAN[1]) and its related wearable technologies. The term "WBAN" refers to human-self and human-to-human networking with the use of wearable and implantable wireless devices. It is considered to be a key type of network node in the Internet of Things [1] and future 5G mobile networks [2]. Recently, there has been increasing interest in this technology from both academia and industry. The technology of wireless body area networks is now considered to be probably the first successful application in the consumer electronics market. A study shows wearable devices already accounted for $800 million and should come to over $1.5 billion in the next couple of years [3]. Devices such as Nike+© [4] and the Fitbit© [5] trackers are very popular in the market. They

---

[1] The term "BAN" (Body Area Network) is also widely used. The two terms are interchangable in this thesis.

measure and track everyday activity such as steps, distance taken, calories burned, stairs climbed and even the sleep quality and transmit these data to smartphones. Moreover, studies forecast the smartphone market will be saturated in 2015, especially in the smartphone high end market [6]. Hence, there should be some new revolutionary products introduced to continue the trend spearheaded by the mobile phone over last few decades, which has become smaller and smarter for people's daily use. Technology giants such as Google, Apple and Samsung chose wearable electronics as they were reported to working on research and development of wearable devices. Apple and Samsung are know to be designing smartwatches, while Google Glass is already in the early adopter program and is available for developers and consumers to test. Although there is an argument about which is the better place to introduce customers to a computer they can wear [7], we know these devices will definitely be more smarter and more powerful than the previous wearable electronics and networking of these devices around the human body will become very important.

Another potential application of body area networks is healthcare. According to the World Health Organization, the aging population and sedentary lifestyle are becoming significant problems which cause millions of people to suffer from obesity, hypertension, cardiovascular diseases or other chronic diseases [8]. A wireless body area network can be formed of a number of intelligent physiological sensors, which is called the body sensor network (BSN) and can achieve continuous monitoring and logging vital parameters of patients no matter their location for early detection of medical conditions. The early detection can give doctors more time to react before a patient's condition becomes critical, decrease the chances of prolonged illness, disability or death, shorten length of stay during hospital treatment, and allow staff time be used more effectively. Medical sensors can be wearable, implantable and ingestible [9]. The monitored information includes electrocardiography (ECG), electromyography (EMG), electroencephalography (EEG), body motion, blood pressure, etc. The information will then be transmitted wirelessly to medical practitioners or carers in real time. The U.S. Federal Communications Commission (FCC) has approved the use of spectrum between 2360 and 2400 MHz for medical body area networks (MBANs), which will probably push electronic health monitoring to take a big step forward. Although there are a wide range of commercial medical sensors available in the market such as proteus© [9] and Metria™ [10], this technology is still at a primitive stage. There are many factors that prevent the widespread adoption of this technology in healthcare. Some are technological, while some are not: for example, medical sensors should collect, store, and transmit information reliably with long battery life and this information should be validated before being forwarded to doctors. But how to validate such information is still unresolved. Other technological factors include lack of seamless integration with infrastructure networks, privacy and security considerations and standardization and interoperability [11]. Beyond user concerns, medical sensor manufacturers have to confront sophisticated and expensive regulatory processes, for example FCC certification and Food and Drug Administration (FDA) approval, to get products to market. Once these sensors are in widespread adoption, how to integrate them into the healthcare system is a tough question because it involves a complex web of stakeholders such as users, emergency services, caregivers, physicians, researchers, etc. Ownership and liability issues must be solved and all stakeholder interests must be protected [12]. Once these problems are solved, MWBANs are expected to be a breakthrough invention in healthcare. In academia, the field of body sensor networks for medical applications has been receiving intensive research attention in recent years. The leading institutions include Imperial College London Hamlyn Centre, MIT Media lab, UCLA Wireless Health Institute, University of Virginia Centre for Wireless Health [13–16], etc. Research projects undertaken include a fall detection system using inertial sensors for elderly people, assessing the efficacy of ankle foot orthoses for children with walking disabilities as a result of cerebral palsy by using body sensors [16], and so on.

Other applications of this technology include sports, military and specialized occupations such as fire fighters. For example, BSN/BANs were proposed to be used as a feedback system for improving the quality of athletes' training [17, 18]. For the military, a body area network can be formed of a number of physiological sensors and wearable equipment such as a head-mounted display on the soldier. These advanced systems are thought to attain enhanced mobility and increased survivability for soldiers. More details of military applications will be discussed in Chapter 7.

1.2 Technological Issues on Body Area Networks

While BSN/WBAN will undoubtedly play an important role in many aspects of our daily life, many issues still remain to be addressed before this technology is widely applied, as summarized, but not limited to, the following:

- **Battery life**: Battery is a key concern for most mobile devices, especially for wearable devices due to their smaller form factor. Most of the power consumption is accounted for in the following three categories: data collection, processing and transmission. A study shows that wireless communications consumes the most power in such systems [19], and in order to reduce the amount of data transmitted, on-node processing is introduced and information compression ratio-information fidelity tradeoff is addressed in the BSN design. Technologies for extending battery life are widely studied such as wireless power transfer and energy harvesting from body motion.

- **Human computer interface**: This is a very interesting topic for consumer electronics. In the PC era, keyboards and mice are the main interfaces between human and computer. Since introduction of first generation iPhone, touch screens are dominant the mobile devices such as mobile phones and tablet computers. What is the interface for wearable devices? Google Glass gives an answer: voice. Besides, some more fancy wearable interfaces were introduced such as Sixthsense [20] and OmniTouch [21]. By using projection and sensing technologies with hand gestures, these wearable system enables graphical, interactive, multitouch input on arbitrary, everyday surfaces. The advantages of these technologies are that they eliminate the use of screens, which will significantly reduce the form factor of devices and improve user experience.

- **Interoperability**: WBAN systems would have to work with other devices, and allow information exchange across different standards and devices. Interoperability is very important in the healthcare environment and military applications.

- **Security and privacy**: Security can mean that BANs may interfere with other systems, for example, industrial scientific and medical (ISM) band-based medical sensor networks in hospitals will have to coexist with other equipment working in these bands. Also there is a fear that the outside systems may be able to interfere with BANs either to deny use or to insert false data; this is again a problem for medical sensor networks. Privacy means the data can only be accessed by the people who have authorisation, especially in the healthcare applications.

- **Sensor validation**: The medical sensed information must be validated against errors in the sensors themselves and cope with other hardware and communication constraints such as unreliable wireless links, interference and limited power reserves.

- **Data consistency and quality**: In healthcare, multiple signs or symptoms are needed for diagnosis. Also, by using multiple sensors with redundant or complementary data can maximize the information content and reduce random and systematic errors. Sensor fusion is widely studied for body sensor networks to improve data quality and consistency [22].

1.3 Why Study Antennas and Propagation?

As discussed earlier, the body area network field is an interdisciplinary area. However, this thesis will only focus on studies of antennas and propagation of body area networks. In the conventional mobile communications, the propagation channel is time varying because multiple radio waves scattered from the local environment cause multipath effect and multiple users are using a common communication medium which would cause interference. Unlike mobile communications, where the base stations are fixed and the mobile units are moving around in a scattering propagation environment, both transmitter and receiver in body area network channels move and change their relative positions. Hence, significant variations in the channels of the WBANs are not only due to local scattering but also because of changes in the geometry of the body. Even when standing or sitting, the body is subject to many small movements such as breathing. During some vigorous activities such as doing sports, the body dynamics will cause significant deterioration of channel performance in terms of shadowing and scattering effects, polarisation mismatch, etc. Besides, the local geometry change and presence of the body may also affect the performance of antennas in terms of impedance match, radiation pattern, efficiency, etc. These issues must be well understood before designing reliable wireless systems for body area networks enabling maximum channel capacity and minimum power consumption.

1.4 Summary of the Project

Research hypothesis The research hypothesis is that WBANs at 60 GHz will have significantly better performance over those at lower frequencies, in terms of co-existence with adjacent WBANs, immunity to interference and interference into other systems. These benefits are expected to be obtained with more advanced BAN architectures and antennas that have higher gain and some reconfigurability.

Objectives In response to this hypothesis, our primary studies of 60 GHz BANs will attempt to establish channel characteristics and the degree of shadowing, and how such shadowing can be overcome using directional or reconfigurable antennas. Comparisons with low frequency BANs in terms of directionality, security and susceptibility will also be made. The specific objectives of this research were as follows:

1. To conduct the first on-body channel measurement campaign at 60 GHz using monopole and horn antennas and to establish wearable antenna design requirements at 60 GHz
2. To investigate interference and covertness[2] of wireless body area networks at 60 GHz using directional antenna and omni-directional antennas and make comparisons with 2.45 GHz WBANs
3. To develop planar antennas with high gain for on-body channels and investigate the antenna performance when in close proximity to the human phantom[3]/body

---

[2] Covertness is defined as a measure of a wireless communications system's immunity to detection by an intercepting receiver [23].

[3] A phantom is a simulated biological body or a physical model simulating the characteristics of the biological tissues [24].

4. To investigate and implement reconfigurable antennas which lead to reduced susceptibility to shadowing for on-body channels

1.5 Layout of the Thesis

The thesis is composed of 10 chapters. An overview of each chapter is given below.

Chapter 2 discusses the background of antennas and propagation for body area networks at frequencies below 10 GHz. The literature review covers wearable antenna design for both on-body and off-body channels, multiple antenna systems, body channel characterisation, inter-user interference among different WBANs, and the use of human phantoms in modelling BANs.

Chapter 3 introduces 60 GHz body area networks and their challenges and advantages over low frequency ones are addressed.

Chapter 4 reviews the methods used in the body channel measurements and advantages and limitations of network analyser and cable-based method are discussed. The equipment used in the measurements are briefly described.

Chapter 5 presents on-body channel measurements using monopole and horn antennas. Statistical analysis is performed on the measured data. Antenna requirements for different channels are arrived at based on the measured results. The polarisation dependence of path gain for different on-body channels is also investigated.

Chapter 6 investigates the co-channel interference between two adjacent WBANs in the indoor environment at 60 GHz and 2.45 GHz. Both horn and monopole antennas are used at 60 GHz. The monopole antennas are used at 2.45 GHz. The interference signal magnitude and carrier-to-interference ratio are measured and characterised.

Chapter 7 studies the covertness of WBANs in military applications. A model is proposed to estimate the probability of detection when a soldier wearing a WBAN system on the body. The detection channel in the model was decomposed into two channels: the free space propagation channel and a body area channel in local environment. The body area channel was characterised by measurements with horn and monopole antennas with body motions in the local area. Comparison of the maximum detection distances at a certain threshold probability of detection between 60 GHz and 2.45 GHz are made.

Chapter 8 presents two planer high gain antennas for on-body channels at 60 GHz: a printed Yagi-Uda antenna and a substrate integrated waveguide antenna. Antenna performance was studied in terms of measurements in close proximity to the phantom and on the real human body.

Chapter 9 briefly reviews the techniques for beamforming and introduces a stripline Butler matrix at 60 GHz. Two substrate integrated waveguide slot arrays were designed working around 60 GHz. They can achieve beam reconfigurability by using frequency scanning. On-body channel measurements with arm-swing movements were conducted using the substrate integrated waveguide slot array to demonstrate beam-reconfigurability for the link performance improvement.

Chapter 10 summarises some important conclusions derived from the study and proposes possible future extensions for this work.

CHAPTER 2

OVERVIEW OF ANTENNAS AND PROPAGATION FOR WIRELESS BODY AREA NETWORKS

2.1 Introduction

MOST research on wireless body area networks is conducted in unlicensed frequency bands such as the ISM bands at 434 MHz, 915 MHz, 2.45 GHz, and the ultra-wide band (UWB) ranging from 3.1 GHz to 10.6 GHz [25–42, 42–50, 50–66]. Even lower frequencies in the 403 MHz band are used for medical implant communication services (MICS). All these frequency bands are covered in the newly developed IEEE 802.15.16 standard for wireless body area networks. The different frequency bands have their advantages and disadvantages. Thus, at lower frequencies radiowaves propagate around and into the human body with little attenuation. However, the data rates achievable at these frequencies are low due to limited bandwidth. Also, signals are more likely to interfere each other due to longer propagation distance and lack of the radiation control.

Besides, the size of the antennas employed has to be quite large due to relatively large wavelength at these frequencies. The situation is reversed at the higher frequency bands. Therefore, the choice of the frequency of operation is a compromise between propagation losses, antenna size, potential for interference and the required data rates.

2.2 Basic Concepts and Theories

Before reviewing wireless body area networks, some basic concepts and theories are introduced, which are used in the following chapters.

2.2.1 Cumulative Distribution Function

In probability theory and statistics, the cumulative distribution function (CDF) describes the probability that a real-valued random variable X with a given probability distribution will be found at a value less than or equal to x. In the case of a continuous distribution, it gives the area under the probability density function from minus infinity to x. The CDF of X is the function given by

$$F_X(x) = \mathrm{P}(X \leqslant x) \tag{2.2.1}$$

where the right-hand side represents the probability that the random variable X takes on a value less than or equal to x.

2.2.2 Level Crossing Rate and Average Fade Duration

The level crossing rate (LCR) at a specified envelope level A is defined as the rate (in crossings per second) at which the envelope crosses the level A in the positive (or negative) going direction as shown in Figure 2.1. The total number of crossings N over a T-second length of data divided by T seconds becomes the LCR:

$$n(r-A)=\frac{N}{T} \tag{2.2.2}$$

The average fade duration (AFD) is the average duration that the envelope remains below a specified level A. It is defined as the sum of N fades at level A dividing by N:

$$\bar{t}(r-A)=\frac{\sum\limits_{i=1}^{n} t_i}{N} \tag{2.2.3}$$

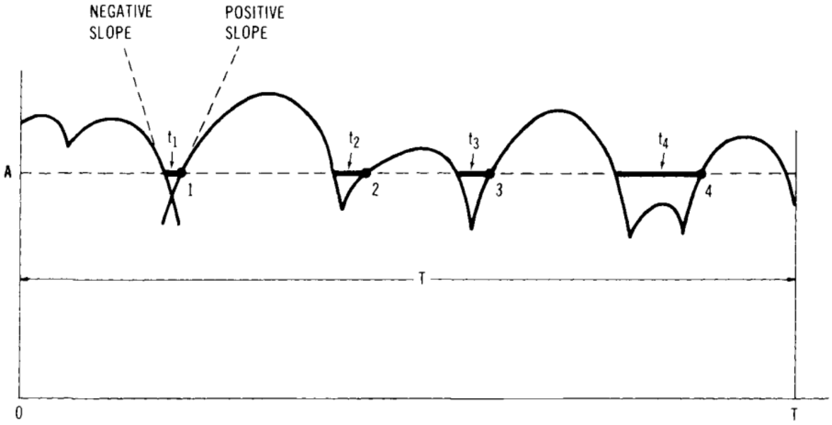

Figure 2.1: Level crossing rate and average fade duration.

The product of Equation 2.2.2 and 2.2.3 becomes a CDF as shown here:

$$n(A)\cdot\bar{t}(A)=\frac{N}{T}\cdot\frac{\sum\limits_{i=1}^{n} t_i}{N}=\frac{\sum\limits_{i=1}^{n} t_i}{T}=\mathrm{P}(X\leqslant A) \tag{2.2.4}$$

Equation 2.2.4 provides a relationship among three parameters: LCR, AFD and CDF.

$$\mathrm{LCR}\cdot\mathrm{AFD}=\mathrm{CDF} \tag{2.2.5}$$

2.2.3 Two-port Network and S-Parameters

A two-port network is an electrical circuit or device with two pairs of terminals to connect to external circuits. Two terminals form a port if the currents applied to them satisfy the essential requirement known as the port condition: the electric current entering one terminal must equal the current emerging from the other terminal on the same port [67].

The two-port network model is commonly used in circuit analysis to isolate portions of larger circuits. A two-port network is considered as a “black box” with its properties specified by a matrix of numbers. This allows the response of the network to signals applied to the ports to be calculated easily, without solving for all the internal voltages and currents in the network. In thesis, the radio channels and a two-port travelling wave antenna are considered to be the two-port networks.

S-parameters are defined in terms of incident and reflected waves at ports. S-parameters are used primarily at UHF and microwave frequencies where it becomes difficult to measure voltages and currents directly. The definition is:

$$\begin{bmatrix} b_1 \\ b_2 \end{bmatrix} = \begin{bmatrix} S_{11} & S_{12} \\ S_{21} & S_{22} \end{bmatrix} \begin{bmatrix} a_1 \\ a_2 \end{bmatrix} \tag{2.2.6}$$

where the a_k are the incident waves and the b_k are the reflected waves at port k. Figure 2.2 shows an example of a two-port network with its S-parameters.

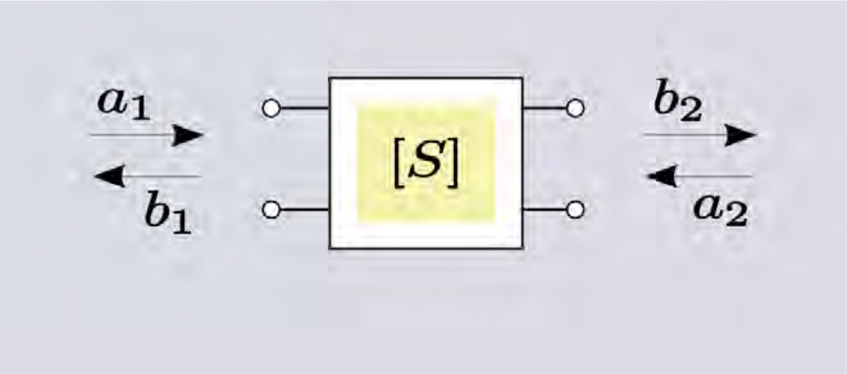

Figure 2.2: Example of two-port network and S-parameters.

2.2.4 Path Loss and Path Gain

Path loss is the power density reduction (attenuation) of an electromagnetic wave when it propagates through space. This term is commonly used in wireless communications and radio propagation. Path loss may be caused due to many effects, such as free-space loss, refraction, diffraction, reflection, aperture-medium coupling loss, and absorption in the medium. Path loss is also influenced by terrain contours, environment, propagation medium (e.g. human body in WBAN scenario), the distance between the transmitter and the receiver (e.g. geometry change due to body movements in WBANs), and the height and location of antennas (e.g. antenna placement on different parts of the body). Path loss (P_L) is defined as the ratio of transmit power (P_t) to receiver power (P_r):

$$P_L = \frac{P_t}{P_r} \tag{2.2.7}$$

Path gain (P_G) is defined as the ratio of receiver power to transmit power:

$$P_G = \frac{P_r}{P_t} \tag{2.2.8}$$

Free-space path loss (FSPL) is the loss in signal strength of an electromagnetic wave that would result when the signals travel in a line-of-sight path through free space without obstacles nearby to cause reflection or diffraction. The equation for FSPL is

$$\mathrm{FSPL} = \left(\frac{4\pi d}{\lambda}\right)^2 \tag{2.2.9}$$

where λ is the signal wavelength, f is the signal frequency, d is the distance from the transmitter, c is the speed of light in a vacuum.

2.3 Radio Channel Characterisation for WBANs

Knowledge of the properties of the propagation channels used in WBAN systems is required for designing reliable communication systems, including developing future communication standards and designing efficient transceivers. The most efficient utilisation of the propagation channel is of great importance for WBAN applications since these devices have to be small and have a limited power supply from batteries. The propagation channels behave very differently depending on the position of the antennas on or in the body, the movements performed by the user, and the surrounding environment.

Different applications require different types of communication channels. In general, three types of transmission channel can be distinguished:

1. off-body channel: communication of a body-worn device with an external device either on a object or another human body;
2. on-body channel: communication between two devices, both of which are mounted on the same human body;

3. in-body channel: communication between a device implanted into a human body and a device mounted on the surface of the body. Communication links between an implant and an off-body device or another implant are also of interest, although they are more difficult to implement in practice due to their high power demands.

Channels for body area networks are usually categorized according to the positions on the body at which the transmit and receive antennas are placed: for example, abdomen-to-chest, and abdomen-to-head. Most attention has been given to the channels between a position on the abdomen where a communication hub is likely to be placed, and positions on the head, wrist, chest, back, and ankle [27, 28]. Propagation between an implant and a device placed near it on the surface of the body has been also investigated [68–72].

2.3.1 Channel measurements and empirical models

Most of the propagation studies reported in the literature take an empirical approach [25–46, 50, 54–66]. Various on-body propagation channels are measured while the test subject either adopts a certain posture or performs certain movements [27, 28, 30, 35, 40]. These measurements are usually performed in an indoor environment [27, 28, 30, 34, 35], although anechoic [35, 40] and outdoor environments [35, 73] have also been researched.

Most researchers have used a network analyser for transmission loss measurements [27, 34, 35, 40]. This approach has an advantage of high accuracy and dynamic range provided by network analysers. However, the disadvantage is that the antennas have to be connected to the network analyser by coaxial cables which can distort the measurement results [34, 74–77]. In order to circumvent this problem a few research groups have used fibre optic cables to connect the antennas to the network analyser [76, 78]. Others [28, 30, 79] employed small wearable transmitters and receivers to measure propagation path loss by recording received signal strength indicator (RSSI).

A large number of propagation studies have been devoted to UWB propagation channels [50, 54–66], as UWB has been found a good candidate for future BAN standards, providing high data rates in on-body as well as in-body communication links. However, existing BAN standards utilise a number of narrow frequency bands, such as 400 MHz and 2.45 GHz. Propagation channels at these frequencies have also been studied along with some other license free bands.

Narrowband channel characterisation

Measurements in various ISM frequency bands have been researched carefully mostly by research groups in the UK, Belgium, Japan, and Australia [25–46]. The majority of the studies have been concerned with the 2.45 GHz ISM band.

It was found that the polarisation perpendicular to the surface of the body produces stronger signal at 2.45 GHz [26, 80, 81] which is attributed to the fact that the creeping surface waves supported by the human body are polarised this way, while tangentially polarised waves attenuate quickly as they propagate around the body [82]. Besides, perpendicularly polarised antennas are usually less prone to the proximity effects of the body, such as detuning and radiation efficiency reduction.

A surface wave propagates along a boundary between two different media (typically one is air), without otherwise radiating. Useful surface waves for WBANs should be tightly coupled to the boundary (i.e., human body), and propagate with low loss. The more tightly the wave is bound to a dielectric layer, the slower the group velocity, the less the wave extends into space, and the easier it is to launch and gather the surface wave using finite-height, or in some cases, zero-height, antennas [80]. The term “creeping waves” is usually used to describe all types of azimuthally propagating waves on a cylinder (e.g. around the torso in the WBAN scenario) [83]. More detailed studies of surface waves and creeping waves around the human body were conducted in [80, 84].

Propagation in the vicinity of the human body is combination of space waves, surface waves and diffracted waves. Which is dominant depends on the position of the antennas and body movements. The space wave is the case when there is a direct line-of-sight (LOS) between the two antennas, and the surface wave and diffracted wave occur when the antennas are shadowed. The on-body path gain vs. the conformal distance between the antennas at 2.45 GHz is presented in [47] where LOS links were found to follow a power law attenuation with distance, and the non-line-of-sight (NLOS) links attenuated exponentially. A model for the path loss variation with the distance and frequency was derived in [37]. And the path loss around the torso was measured in [34, 40] and was found to increase exponentially in the shadow region. A model for path loss variation around the torso which includes the waves reflected by the environment was suggested in [34].

The body channels were found to fade significantly when the human body moved while performing various everyday activities. There are many possible reasons resulting in the observed fading. It could be due to the changing distance between the antennas, changing relative orientations between the antennas or the antenna to the body, due to shadowing by parts of the body, or it could be caused by combining several arriving multipath components at the receiver. Unlike the cellular communications, where the multipath fading is much faster than the other types of fading, in WBAN scenarios the scale of multipath fading and the scale of variation of shadowing, or other types of slow fading were found to be much more similar. Nevertheless, it is possible to separate short-term and long-term fading. The short-term fading for 2.45 GHz WBAN was found to follow a Rician [29, 34, 38, 41, 42] or a Nakagami-m [30, 32, 34] probability distribution due to different channels, body movements and environments, while the long-term fading at 2.45 GHz was best fit to either a log-normal [27, 34, 38, 42] or a gamma [41] distribution. The channel variations were found to be non-stationary, so that the parameters of both the short-term and long-term fading change with time. Some attempts to fit on-body fading data to a single probability distribution have also been made in [35]. And in [46], a three-state Fritchman model was suggested to characterise channel fading.

Second order statistics such as level crossing rate (LCR) and average fade duration (AFD), and also Doppler spread spectrum were investigated in [29, 30, 32, 39, 42]. The Doppler spread was found to be less than about 16 Hz. The time delay spread of narrowband channels has not been researched intensively, although in [34] it was found to be less than the order of a few tens of nanoseconds, which is much less than the symbol rates of Bluetooth or Zigbee, and therefore validates the narrowband approximation for these systems.

UWB channel characterisation

A UWB (3–10 GHz) propagation channel can be fully characterised by its channel impulse response or the channel transfer function. In the case of body-area communications, these are both random functions of time delay and frequency, respectively, randomly changing in time, since the channels are not stationary. Several statistics describing the channel impulse response are required for designing a reliable and efficient communication system. They include the average energy within the received pulse, or average path loss, the distribution of the power within the pulse given by the power delay profile (PDP), the distribution of the amplitude of each delay bin of the pulse, and the distribution of the number of paths within each bin, which are required to specify the link budget and RAKE receiver requirements [85]. Time delay characteristics such as mean delay or root-mean-square (RMS) delay spread are necessary for defining the optimal symbol rate. Besides, knowing the direction of arrival of different multipath components helps in designing antenna systems.

UWB propagation channels have been investigated by a large number of research teams from around the world [50, 54–66]. With the exception of [56, 60, 86], most measurements in these investigations were performed with a network analyser. The path loss averaged across the whole UWB band was derived in most studies. Variation of the average path loss with the antenna separation was studied in [56, 61, 62, 64, 66, 86], where a variety of antenna positions around the torso were considered. The path loss variation with distance was usually expressed in a form of a linear fit to the logarithmic path loss data versus distance d expressed in either linear [61] or logarithmic units [57, 62, 66]. The latter corresponds to a power law distance variation of a form $P \propto d^{-\gamma}$, while the former represents an exponential fall off, $P \propto e^{-\alpha d}$. The exponent was found to take a range of values between 2 and 4, depending on the scenario. It was closer to 2 when antennas were on the same side of the body and closer to 4 when on the opposite sides. For propagation around the torso even higher values of up to 6 were reported in [57].

The probability distribution of the pulse amplitudes was found to be log-normal in [57, 66]. The small-scale distribution of the energies in each bin was also found to be log-normal, or Nakagami [57]. Time delay parameters, such as mean excess delay and delay spread, were also investigated in [55, 86] and in [62], where the Nakagami distribution was found to be most adequate for the description of the delay spread. The maximum value of the

RMS delay spread did not exceed 12 ns and was usually less than 6 ns. The variation of RMS delay spread with distance was given in [55]. The PDP was found in [57] to fall off exponentially with the time delay, while in [64], a dual-slope linear model was suggested for the PDP. The correlations between the taps in a multi-tap model of the received pulse were derived in [64], and a first-order Markov model was suggested for path arrival probabilities in [60]. A comprehensive model of a UWB channel was developed in [61].

Off-body UWB channels have been investigated in [50, 56, 58, 59], where variation of channel parameters such as path loss and time delay spread was found for a variable distance between the off-body antenna and the body and for various orientations of the body in indoor environments. The small-scale variation of the total signal power was found to have a normal distribution in [59] and modelling of the PDP for off-body links was considered in [58].

2.3.2 Simulations and human phantoms

Simulating radiowave propagation around a human body on a computer appears to be an attractive option for characterizing body area channels because it does not require expensive equipment and time-consuming human trials, and, on the other hand, allows for a more detailed description of the propagation phenomena in the form of electric field distributions and 3-dimensional radiation patterns which would be notoriously difficult to obtain through measurements. The simulations become particularly valuable when in-body channels are studied. However, this approach is limited because the body is electrically large at most frequencies of interest, and therefore most simulation methods require prohibitively large processing and memory resources. Nevertheless, such simulations have been attempted in [82, 87–109].

The finite difference time domain (FDTD) is a good method for simulations of WBAN links because it can relatively easily handle large lossy dielectric objects of complex shapes, such as a human body. Two commercial simulation software packages have been used to study on-body and in-body channels, namely, CST Microwave Studio© [110], and Remcom XFdtd© [111]. Both of these provide an accurate model of the human body as an option, such as SAM phantom. The movements of the human body can be represented in the simulations by using an animation software package, as was done in [92, 93]. A few non-commercial FDTD simulators specifically designed for simulating a human body have also been presented in the literature [106, 109].

Variation of the path loss and delay spread around the torso was obtained with Remcom XFdtd© simulations in [82, 108] for a number of ISM frequency bands. In [108], simulations were performed on several different human body models, and the path loss in LOS and NLOS scenarios was found to follow a power law increase with distance, with the exponents varying from 2 to 3.4 on different bodies due to different phantom dimensions. Similarly, UWB channel parameters, such as path loss and delay profile, have been investigated through simulations in [94, 96, 105, 106]. Moreover, in [96, 105] a statistical UWB channel model was derived for a number of transmission links, based on FDTD simulations of a body adopting various static postures [96, 103, 105, 106]. The effects of human morphology on antenna performance and propagation were investigated in [102], by comparing simulation results derived with different body models.

At the moment, computations of the fields around the whole body below 3 GHz in an FDTD simulator can take up to several hours, which restricts the possibilities for studying various channels and movements. Moreover, including the effect of the environment on on-body channels is virtually impossible due to the extremely large size of the overall computational volume. This is caused by the fact that the simulated body is electrically large on one hand, but on the other the antennas mounted on the body can have features much smaller than the wavelength, thus requiring fine meshing in the computational domain. Methods to overcome this problem were proposed in [88, 91, 98] through the use of hybrid models in which the antennas are simulated by a method different from that used for the whole body. These problems could also be resolved by employing a ray-tracing technique [100, 101, 107] which is expected be particularly important for simulating mm-wave channels [112]. Other ways of improving the efficiency of FDTD simulations were also suggested in [89, 90].

2.3.3 Characterisation of Dynamic Body Effects

The dynamic human body effect is a crucial factor for communications of wireless body area network. The following chapters will show this dynamic has significant effects on channel performance. In general, these links are susceptible to strong fading because of amount of causes, such as changing distance and orientation between the antennas, shadowing by body parts and polarisation mismatch. The characteristics of these channels will greatly depend on the position of the antennas on the body and the body movements. Therefore, characterisation of the body movements is very important if wireless communication channels are to be characterised sufficiently and accurately.

A method to characterise body movements and channel performance simultaneously based on motion capture has been proposed. Figure 2.3 shows the process of making an animated human body. Four steps are needed to create a 3D animated human model: scanning the human body to obtain a body surface; capturing body movement and antenna position using motion capture equipment such as VICON© [113] with simultaneous wireless channel measurements; creating an animated model using movement data and body surface data; and creating static models for EM simulation from animated frames [114]. The relationship between body movements and channel performance can be fully analysed and measurement result can be validated using simulation results. Based on this method, a simulated study on an animated human walking movement for body are network was carried out at 1-6 GHz band in [114]. Initial measurement study based on this method for 60 GHz on-body channels have been investigated in [115]. Note that this method is not used in the studies described in the following chapters, but it is very useful and recommended for on-body channel characterisation.

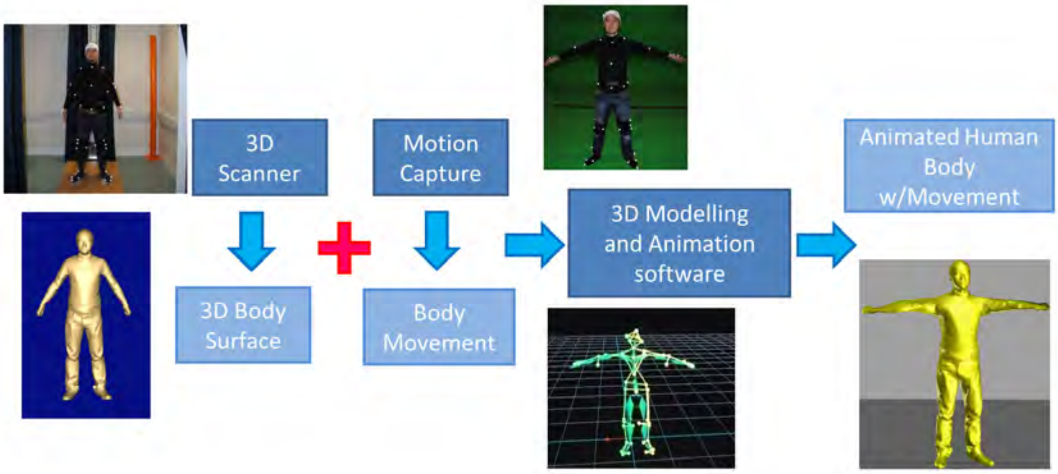

Figure 2.3: The processes of making an animated human body with Motion Capture [114].

2.4 Wearable Antenna Design

There are three primary requirements for wearable antennas. First, the antenna should be low profile, lightweight, robust, and conformal to the body; second, the antenna should be insensitive to the proximity to the human body; third, the antenna needs a radiation pattern which can minimize the channel loss and interference and also meet the requirements for human radiation exposure such as radiation absorption rate (SAR). Antenna matching and efficiency are important issues for wearable antenna design, which will be affected by the close presence of the human body. In most designs, the radiating elements are shielded from the body by introducing a ground plane or an electromagnetic band-gap (EBG) backing layer. Antenna efficiency can be improved by employing such a ground plane. The radiation pattern of the antenna and its influence on the observed path gain are important issues for wireless body area networks. Measurements show that the path gain is highly dependent on the antenna type and link geometry. The positions of antenna placement also determine the propagation mode of electromagnetic waves. For example, for the head-to-waist link, a surface wave or creeping wave is dominant propagation [81] while in waist-to-wrist link, the space wave is dominant when there is no obstacle between the transmitter and receiver.

2.4.1 On-body conventional antennas

Narrowband antennas

Many conventional antennas have been investigated for body-worn applications such as planar dipoles, monopoles, planar inverted-F antennas (PIFAs) and microstrip patches. These antennas can be manufactured onto a printed circuit board (PCB) which makes them a practical antenna type due to their low cost and straightforward fabrication.

The performance of different types of conventional antennas in on-body channels below 3 GHz were investigated and compared in [42, 47, 48]. Based on these studies, monopole antennas achieve the lowest path loss and least fading compared to all the other types of antennas. Planar inverted-F antennas are the second best for their performance in the on-body channels. Other types of antenna such as dipoles, loops, and printed-F antennas were found to have high losses in the proximity to the body. Due to broadside radiation characteristics, microstrip patch antennas are more suitable for off-body communications.

It was observed [47] that a quarter-wavelength monopole is suitable for various on-body channels since it achieves an omnidirectional pattern with maximum radiation along the body surface which make less chance to lose LOS between the transmitter and receiver. Besides, the polarisation of monopole antennas is normal to the body surface which matches the polarisation of the surface wave and hence improves the link performance. One disadvantage of monopole antennas is it height, to solve this problem a reduced height monopole with disc loading was proposed at 2.45 GHz [42]. However, it is still too large to be integrated into small wearable devices.

There is a contradiction on microstrip antennas: they are ideal candidates for on-body applications because of their low profile and conformal structure but they normally provide off-body radiation patterns. A high mode microstrip patch antenna at 2.45 GHz was proposed to maximise coupling between body-worn devices on a curved body surface such as around the torso, by launching creeping waves. The measured results show that it only has a 2 dB extra path loss compared to monopole antennas [116]. A microstrip patch antenna with pattern switching ability was proposed in [117]. It can switch between on-body propagation mode and off-body propagation mode using shorting pins.

A surface wave antenna which applies principles of Yagi-Uda antennas to the dipoles placed parallel to a body surface was proposed at 2.45 GHz [26]. This antenna exploits the fact that a dipole near a surface excites surface waves in the direction along its axis, and achieves better performance than the conventional Yagi antenna in the proximity to the human body. Despite being flat, this antenna achieves path loss similar to those of a monopole.

One major disadvantage of narrowband antennas working below 3 GHz is their size. As known, the normal resonant antenna size should be equivalent to a length of half a wavelength, which makes these antennas too big for body-worn applications. Hence, miniaturization techniques are applied in wearable antenna design. These techniques include inductive and capacitive loading, use of multiple folded arms with dipole and monopole-like antennas, use of high permittivity and/or permeability materials, use of EBG structures, feeding the resonant antenna with a parasitic element, etc. In theory, any electrically small antenna may be matched at any frequency. However, in practice, it may be difficult to match a small antenna with the desired efficiency. For example, an asymmetric meandered flare antenna working at 300 MHz was proposed for body-worn applications [118]. The size of the antenna is 30×4 cm^2 and achieves reasonably good performance but the gain of the antenna is below -10 dBi.

Another drawback of these antennas is that it is difficult to achieve directional radiation patterns and good radiation control which are advantageous for improving link performance and reducing interference. Antenna arrays are, in general, too big for on-body applications at most frequencies of interest. However, there are still a few examples of on-body antenna arrays in the literature. In [119], an eight-element patch array working from 325 MHz to 1000 MHz was proposed for body-worn through-wall radar application. The array is 1.75 m long and conformed to the size of a soldier's extended arms. This array achieves a reasonably good performance but pattern distortion occurs at higher frequencies. A beam-switched monopole array was proposed for on-body applications at 2.45 GHz in [120]. The array is formed of a driven disk-loaded monopole with 4 parasitic disks. By shorting the parasitic elements, beam switching is achieved. Although some attempts have been made to achieve a high gain switched beam antenna [120], these antennas have large size and poor beam control ability. Achieving high angular resolution of radiation pattern for a small antenna array is very difficult at these frequencies.

UWB antennas

Recently, many efforts have been made to investigate the UWB wearable antenna design [49–53]. Unlike narrowband antennas, the UWB antennas need not only good impedance matching and radiation characteristics but also the ability to preserve the pulse shape of the signal. Some additional parameters must be considered in the design of UWB antennas such as frequency domain transfer function, impulse response and time spread. Most of UWB antennas proposed for WBAN communications are variants of monopole/dipole antennas [50–52, 121], and slot antennas [49, 53]. Antenna performance in close proximity to the human body is also investigated in terms of signal fidelity, SAR, and radiation efficiency [49–53].

There are many advantages for antennas used in UWB WBANs. First, the size of antenna becomes small as frequency increases. Second, high gain of antennas can be achieved. A study shows a UWB Vivaldi antenna can achieve up to 10 dBi gain [122]. Although there are implementations of beamforming techniques at UWB band reported in the open literature such as one using a Butler matrix [123], antenna arrays with beamforming abilities are still too large for body-worn applications.

2.4.2 Textile antennas

Textile antennas have attracted considerable attention from researchers worldwide. This type of antenna has been demonstrated to have comparable performance to their conventional antenna counterparts, while they are light weight, more flexible, and easy to integrate into clothes. Because these advantages, they are very promising candidates for wireless body area networks. Many conventional types of antenna have been implemented in textile both for narrowband and UWB applications. Textile microstrip patch antennas have been demonstrated in [124–127]. Others include slot antennas [128], dipole antennas [129], Planar inverted-F antennas (PIFA) [130], loop antennas [131], spirals [132], etc. Lots of effort have been made to investigate the effect of bending and crumpling for textile antennas [124, 125, 129, 130]. Studies show both bending and crumpling have significant adverse effects on antenna impedance matching, impedance bandwidth, and radiation pattern. However, employing an EBG ground plane for such an antenna can reduce these effects and also minimise its SAR value [133].

2.5 Interference and Covertness for WBANs

Interference issues are a vital consideration in wireless body area networks design. W-BANs are very mobile when a user moves. Also, it is expected that multiple WBANs are not coordinated, but are fully autonomous. Hence, one WBAN may cause severe interference to another WBAN or other networks when it moves into the range of other networks, especially in densely populated environments such as shopping malls, hospital wards, etc. This event is sometimes referred as a "network collision" [134]. The nature of human movements means the network collisions may be either very short, i.e. people passing by on the street, or very long, i.e. family members stay with patient at hospital for hours. The cellular approach for interference mitigation [135] may be not applicable to WBANs because of the mobile and variable nature of WBANs. As discussed in [135], the interference issue is usually handled at the MAC layer or at higher layers of OSI model, but it also needs to be understood at the physical layer, and techniques at the physical layer can be applied to mitigate interference.

For interference, an off-body scenario is most likely, so it is similar to off-body communication characterisation. There have been intensive studies of off-body communications at ISM bands [136–138] and UWB [58, 59, 139], but the interference study from an antennas and propagation perspective has attracted less attention.

2.5.1 Narrowband interference

Gilbert, Rodda *et al.* at NICTA [134, 140, 141] performed a comprehensive study of co-channel interference in WBANs based on indoor measurements at 2.45 GHz. Custom-designed channel sounders were used and five subjects were considered simultaneously in the study. Factors such as distance, orientation and body movements were considered and interfering signal strength and signal-to-interference ratio were measured and characterised. It was found that interference for WBANs is not well determined by direct person-to-person distance, body movements and orientation are more significant and finally signals and interference are independent random processes.

Another study for inter-WBAN interference was conducted based on simulation [140]. 14 subjects with isotropic antennas on the body were simulated in the indoor environment at 2.45 GHz and 60 GHz. Signal coverage and carrier-to-interference ratio (CIR) were calculated and compared at both frequencies. The study indicates that using 60 GHz reduces interference significantly due to high signal attenuation and the CIR is improved by more than 20 dB compared to employing 2.45 GHz WBANs. However, body movements and orientation were not considered in this study, which proved to be important factors in modelling interference between WBANs.

Other than using higher frequencies, other techniques at the physical layer can be applied to reduce interference between WBANs. A method of interference cancellation using multiple antenna systems to improve the signal to interference plus noise ratio (SINR) for WBANs is proposed in [142]. By measuring the interference signals at the two branches of a two-antenna receiving system at transmission free periods, the interference can be cancelled using measured signals during transmission. Based on this method, a 7 dB interference rejection gain was achieved for the belt-to-head channel when the transmission interval was set to 60 ms. The desired signal transmitter was kept shutdown for 40 μs between these intervals to measure the interference signal.

Interference does not only arise from adjacent WBANs, but also from the environment. For example, the spectrum around 2.45 GHz is very congested. Many standards are working at this frequency such WiFi, Bluetooth, and Zigbee. A measurement study was conducted using mobile WBAN to collect RF noise at 2.45 GHz in various environments. Five receivers were placed on five positions on a subject, who was walking through different environments. Results show the significant spectrum activity was detected during 5% of the duration of the measurements [143].

2.5.2 UWB interference

Before reviewing the interference for UWB radio, two spread-spectrum techniques, Direct-Sequence Spread Spectrum (DSSS) and Frequency-Hopping Spread Spectrum (FHSS), will be briefly reviewed. Both techniques can provide secure communications by improving resistance to interference, noise and jamming, and prevent detection.

In DSSS, each data bit is spread to a sequence of much faster chips. By doing this, a wider bandwidth is required to transmit this data, resulting in a spread of energy in the frequency domain which is slightly above the noise floor of typical narrowband receivers.

FHSS in principle is exactly the same in terms of spreading the signal energy in the wide frequency spectrum to achieve the advantages of wideband communications. However, the wide bandwidth is achieved by hopping the frequency based on a pseudorandom code. Because the frequency changes very fast, the probability of detection and interference becomes small. This technique is used in Bluetooth.

Like spread-spectrum techniques, UWB shares the same advantages of expanded bandwidth, but the method of achieving it is different. In UWB communications, the signal is short duration pulse which inherently has wide bandwidth without using spreading codes or modulations. Also, the short pulse with the duty cycle of less than 0.5 percent provides very low transmission power and additional covertness compared to spread-spectrum techniques where the narrowband signals are always present.

Because a low power spectral density of less than -41.3 dBm/MHz is required for UWB communications by FCC, UWB systems will not cause significant interference to existing narrowband systems. However, the UWB signal is vulnerable to narrowband interference (NBI) of a high power level from existing narrowband wireless systems. Some NBI suppression techniques have been proposed such as adaptive notch filters and an optimal pre/post-rake UWB transceivers [144, 145], but these methods increase system complexity.

Based on the author's knowledge, there is no quantitative study on RF covertness for WBAN from antennas and propagation point of view.

2.6 Summary

There have been a great number of studies on antenna design and propagation channel characterisation for wireless body area networks at ISM narrow bands and UWB. Many issues have been thoroughly investigated such as antenna performance in close proximity to the human body, understanding the path loss for body channels and its variation with movements, radio propagation modes on the human body, etc. On the other hand, there are limited studies on interference and covertness for WBANs at the physical layer.

Although current wireless solutions for WBANs have been developed for many years, some issues are still not satisfactorily solved for such wireless communication systems. These include compact and high efficiency antennas for body-worn applications, high levels of security and immunity to interference and detection and also high speed communications with data rates up to Gbit/s.

UWB seems to be more competitive than narrowband technologies in terms of above-mentioned requirements. However, the adoption of UWB in the market is not very successful. In 2006, IEEE 802.15.3a, a standard to provide a higher speed for wireless personal area networks using UWB, was withdrawn. In 2009, the Bluetooth Special Interest Group dropped the development of UWB as part of an alternative MAC/PHY for Wireless US-B. It has even been claimed that UWB was dead in the PC and consumer electronics segments [146].

As the time of writing, more attention has been transferred from UWB to 60 GHz radio. In the following chapters, the alternative wireless solution at 60 GHz will be proposed for WBAN. As mentioned in the beginning of this Chapter, the choice of the frequency of operation is a trade-off between the propagation losses, the antenna size, interference and the achievable data rates. The advantages and challenges of 60 GHz will discussed and possible solutions will be suggested to overcome these challenges.

CHAPTER 3

INTRODUCTION TO 60 GHZ WIRELESS BODY AREA NETWORKS

3.1 Introduction

ALTHOUGH wireless body area networks have advanced in recent years, many applications are still not well served by current standards and technology, and the perceived low security has led to slow uptake of the technology [147]. In particular, there is no wireless solution currently for applications that require high levels of electromagnetic energy control in order to minimise interference to other equipment and also minimise susceptibility to observation and jamming, coupled with providing high data rates. Some of the general applications that need these features include:

- Secure and high-bandwidth wireless links for dismounted soldiers on the battlefield for body condition monitoring and for integrating a modular system of weapons and their sighting systems.

- Delivery of high-definition, uncompressed, medical-standard video and audio data in hospital and clinical environments.
- Wearable systems for high rate data used in crowded environments, such as sports events, shopping malls, etc.

The use of millimetre wavelengths has the potential to meet these aspirations. The band around 60 GHz has drawn increased attention from researchers despite earlier issues associated with the cost of producing commercial products [148, 149]. With advances in millimetre-wave chipsets manufacturing, led by for example INTEL and IBM, the band has been opened by various regulatory authorities, and standards such as IEEE 802.15.3c for wireless Personal Area Networks [150] and IEEE 802.11ad for multi-gigabit speed wireless Local Area Networks [151] have recently appeared. The band has significant advantages for body area networks, in particular,

- Very small size of equipment on the body.
- High signal integrity and low visibility at the RF level, due to good radiation control using directional or reconfigurable antennas and high attenuation beyond the body area.
- Gigabits per second data rates.

There has been no intensive research concerning on-body millimetre-wave antennas and propagation, as previous studies were mainly focused on the effects of weather in outdoor environments and furniture in indoor ones [152]. These typical indoor characteristics will be present in body area networks, but in general the physical distances are much shorter and body motion will increase the possibility of shadowing. There are also no standards for millimetre-wave body area networks and little understanding of their links' susceptibility to shadowing due to body movements.

3.2 Benefits and challenges for 60 GHz WBANs

The primary advantages of 60 GHz communications are small RF components and antennas, lower interference, visibility and susceptibility to interference, a wide available spectrum (57-64 GHz) and high data rates [148, 153]. Concerns relate to possible high cost and high path attenuation, leading to low received signal levels. However, the very high signal fall-off with distance will give a considerable advantage over microwave BANs. High gain antennas can be used to offset the channel loss, but can also lead to increased susceptibility to shadowing. For example, in an indoor environment, such as a base station to TV link, shadowing due to loss of line of sight as a human stands in the way, can be overcome by switching the antenna to a reflected ray, either off the wall or the ceiling. This strategy also leads to higher security, as the energy would be confined to a vertical cylinder surrounding the body, thus giving good BAN to BAN and BAN to fixed base station isolation, except when needed, when the BAN antennas would switch to an outward facing beam. This has long been an aspiration for microwave BANs, but the low directivity of small antennas prevents it.

The challenges are as follows: The mechanisms of radio propagation and its interaction with the human body at MM wavelengths have not been well studied. There is a need for new and advanced antennas to realise two key advantages [154, 155]: First, the antenna is more directional and hence, by appropriate beam control, provides additional security (by low interference on receive and low signature on transmit) at the physical layer. Second, the shadowing effect from the human body is much more significant and makes NLOS communication very difficult [156]. Reconfigurable antennas can overcome this problem, by switching to non-obscured ray paths. In addition, even if it is possible to lower the cost of the chipset, packaging 60 GHz circuits remains a significant technical and cost challenge. Because on-body antennas are so small, it may be optimal to make them part of the package, or even to integrate them as part of the die.

3.3 60 GHz Wireless Communications

The millimetre-wave band, especially the unlicensed spectrum around 60 GHz is an ideal candidate for future high-bandwidth commercial wireless communication systems. The free spectrum around 60 GHz is substantial compared to microwave frequencies. A reasonably good agreement in spectrum regulation at 60 GHz can be found among many countries. Frequencies allocated are 56-64 GHz in North America and Korea, 59-66 GHz in Europe and Japan. Studies show the attenuation at 60 GHz is much more severe than at lower frequencies such as 2.45 GHz. Three factors contribute to this high attenuation: smaller antenna aperture at 60 GHz, loss due to atmospheric conditions and higher penetration loss of materials as well as reflection and diffraction loss [157]. But this high attenuation facilitates high spatial reuse of these frequencies. In addition, because of the quasi-optical characteristics of 60 GHz signals, shadowing effects are much more severe, which makes non-line-of-sight communications very difficult. Hence, 60 GHz communication is most suitable for short-range applications requiring gigbit per second wireless data transfer.

Another advantage of the 60 GHz band that it has little civil commercial value at present while the band in 400 MHz to 3 GHz is very congested and very expensive. The spectrum auction for 4G mobile communication at 800 MHz and 2.6 GHz cost £2.3 billion in the

UK.

Many potential applications for 60 GHz radio are proposed. Due to high demand in high speed in cellular data, mobile broadband could move to a higher frequency band. Samsung has developed a millimetre-wave based mobile system for the future 5G mobile communications. It can achieve more than 1 Gb/s data rate while the transmitter and receiver are 2 km apart in a line-of-sight connection. For non-line-of-sight communications, the range shrinks to about 200 to 300 meters [158]. Future wireless local area networks (WLAN) will also adopt 60 GHz spectrum based on the IEEE 802.11ad and WiGig standards [151]. Some WLAN device manufacturers have proposed hybrid 2.5/5/60 GHz WLAN solution which use lower frequencies for normal operation and 60 GHz for short-range high-speed line-of-sight communications. Besides, 60 GHz wireless technology has the potential to replace cables for high rate multimedia streams such as WirelessHD.

3.4 Review of 60 GHz Antennas

Due to the characteristics of 60 GHz signals, some additional requirements are needed for antenna design. First, a high gain, directional radiation pattern is desired. This is because of high attenuation at 60 GHz, where high antenna gain can boost the signal. Also, studies show achieving gigbit per second data rates requires high antenna gain, especially in relatively long ranges. For example, to achieve 5 Gb/s data rate at 20 m, a combined antenna gain of 25 and 37 dBi are needed for line-of-sight and non-line-of-sight links, respectively, with no shadowing [159]. In addition, narrow-beam antennas with line-of-sight links can mitigate multipath effects. Multipath is normally eliminated using modulation schemes such as equalisation, diversity, or multicarrier techniques at microwave frequencies, but achieving these techniques at 60 GHz is deemed to be impractical, or too expensive. Second, because the size of antenna at 60 GHz is of the order of a few millimetres which makes it easy to be integrated into the transceiver package or eventually onto the chip itself. However, challenges must be overcome such as low on-chip efficiencies and lossy package interconnects. Third, a switched-beam antenna or a phased antenna array are required to overcome shadowing. The human body is considered as the main obstacle in indoor communications at 60 GHz [160]. In the indoor environment, switched-beam antennas are proposed to overcome shadowing caused by human activity.

Because of the integration requirements, many traditional antennas are implemented by PCB or other substrate based methods. These antennas include dipoles [161], microstrip path antennas [162], slot antennas [163], Yagi-Uda antennas [164], reflector antennas [165], horn antennas [166]. Most of them are directional antennas. To achieve high antenna gain, arrays of multiple radiating elements are formed for dipole and slot antennas.

Some antennas are more suitable to work at millimetre-wave frequencies such as dielectric resonator antenna (DRA) and lens antennas. DRAs are generally formed of a dielectric resonator of various shapes mounted on a metal surface. Electromagnetic waves are radiated into the dielectric resonator from the feed on the metal surface and bounce back and forth between the walls of resonator, forming standing waves. Because the dielectric resonator is not entirely enclosed by a conductive boundary, it can radiate as an antenna. An advantage of DRAs is that they have low losses and are more efficient due to lack of metal parts, which are very lossy at very high frequencies. Many DRAs have been designed at 60 GHz [167]. In geometric optics, a lens acts as a concentrator, gathering energy of light over an area and concentrating it to a point. Due to the quasi-optical characteristics of millimetre-waves, this principle can be applied to make lens antennas. The lens can provide a high gain, narrow beamwidth radiation pattern with high efficiency, and it can also act as a beamformer for multi-beam antennas [168]. A Rotman lens is a type of beam-forming network which can be implemented using microstrip lines. It is compact, reliable, cost-effective and wide band without the need for switches or phase shifters [169]. Other beamforming techniques include the Butler matrix, Blass matrix, frequency scanning, and phased arrays. More details on such techniques will be discussed in Chapter 9. An exhaustive review on beamforming techniques can be found in [170].

Some novel technologies are introduced to implement millimetre-wave antennas, such as the substrate integrated waveguide (SIW) and low temperature co-fired ceramic (LTCC). SIW is formed of two periodic rows of metallic vias or slots connecting the top and bottom ground planes on the both sides of a dielectric substrate. The advantages of SIW structures are compact, low loss, flexible and cost-effective. They are a promising solution to achieve the integration of complete system-on-substrate by integrating active circuits, passive components and radiating elements on the same substrate at millimetre-wave frequencies. Many of RF components have been developed using SIW technology such as power dividers, antennas, Butler matrices, filters and couplers [171–175]. LTCC is a multilayer platform technology used in fabrication of components, modules and packages which integrates passive components such as filters and antennas in the same package up to millimetre-wave frequencies. Components can be assembled in a number of layers (up to 70 layers) and 3D integration enables miniaturisation of modules. Other advantages of LTCC are low conductor and dielectric losses, good thermal conductivity, cost efficiency, stability and hermeticity. One challenge of this technology is achieving the required fabrication precision at millimetre-wave frequencies. Many antennas have been developed using LTCC technology at 60 GHz [176–180]. Combinations of SIW and LTCC technologies have been implemented to design antennas working up to 140 GHz [181].

3.5 Summary

This chapter introduces 60 GHz wireless body area networks, and gives the reasons why we need 60 GHz WBANs and the challenges we may face when implementing them. Then, 60 GHz wireless communications and 60 GHz antennas are briefly reviewed. Requirements for 60 GHz antennas are proposed. This chapter presents a general requirements overview for the following chapters, where 60 GHz wearable antennas are designed based on the requirements proposed and body channels are investigated to test the hypothesis stated above. Finally, solutions are provided to overcome the challenges.

Chapter 4

Measurement Methods

4.1 Introduction

It is unrealistic to characterise body channels with body movements by simulation because the human body becomes electrically large at 60 GHz and doing full body simulation with numerous body movement snapshots is prohibitively expensive computationally. Hence, most work done in this thesis is based on measurements, except for antenna design and characterisation, where just antennas and a small block of a numerical phantom have been simulated. For body channel characterisation, there are generally two measurement methods: the first method collects data using a vector network analyser (VNA) to measure S_{21} between a transmit antenna and a receive antenna. Both antennas are connected to the VNA using coaxial cables. The second method records the RSSI or link quality indicator of a signal transmitted from a self-contained transmitter module at a given sampling frequency. Both transmitter module and receiver module are designed using commercial-off-the shelf parts, such as antennas, amplifiers oscillators, microcontroller, memories, etc. The data collected by the receiver will store in the memories on the module. The main advantage of this method is that it does not require the use of any cables. In this work, the first measurement method was adopted because of its flexibility, and simplicity and also the basic properties of body channel can be well established using this method.

4.2 Equipment in the Measurements

This section describes the equipment used in the measurements including the VNA, antennas, cables, and amplifiers.

4.2.1 Vector Network Analyser

The vector network analyser is the key instrument in the cable-based measurements. The VNA used is a Rohde & Schwarz© ZVA67. It is a four-port VNA with working frequency up to 67 GHz. One major concern of this instrument is its dynamic range. In order to maximise the dynamic range at 60 GHz, the direct access port of the VNA are used to eliminate losses in the directional coupler when using bi-directional ports. With IF bandwidth of 1 kHz, a 76 dB dynamic range. This dynamic range is calculated, so that the difference between the RMS noise level of the VNA and the received signal level when two cables were connected together through the direct access ports of the VNA. can be achieved at 60 GHz with 10 dBm output power. The trade-off between the sweep speed of the VNA and the dynamic range is an important issue for channel measurements of WBANs. The sweep speed is controlled by the IF bandwidth of the VNA and is expected to be fast enough to capture the effects of body movements on radio channels, but increasing the IF bandwidth will increase the noise level, hence reduce the dynamic range. In order to achieve a good compromise, a 1 kHz IF bandwidth was adopted for most measurements in this thesis, except higher dynamic range is needed for 60 GHz on-body channel measurements using monopole antennas.

4.2.2 Antennas

The following antennas working at 60 GHz were used in the measurements: monopoles, 20 dBi standard gain horns, scalar horns with an orthomode transducer, a printed Yagi-Uda array, a substrate integrated waveguide antenna, and a substrate integrated waveguide slot antenna. The 60 GHz monopole antenna is made of a semi-rigid coaxial cable (Anritsu© V086MM-30CM). The inner conductor of coaxial cable was machined to be a quarter-wavelength longer than the outer conductor and a metal disc with 20 mm diameter was mounted on the top of the outer conductor acting as a ground plane. The measured results show this antenna achieves a good impedance bandwidth and ominidirectional pattern in the azimuth plane. The 20 dBi standard gain horn is a commercial rectangular horn antenna from Flann© with series 240 model 25240. The scalar horn with orthomode transducer is also a commercial antenna from Millitech©. There are two ports on the orthomode transducer and it can achieve two orthogonal polarisation simultaneously. The last three antennas were designed in this work and will be introduced in Chapter 8 and 9. Some measurements were also conducted at 2.45 GHz for comparison. Monopole antennas at 2.45 GHz and a wideband horn antenna from Q-par with model number WBH1-18S were used in these measurements.

4.2.3 Cables

During on-body measurements, cable assemblies can be easily damaged due to repeated flexing after multiple uses, especially at 60 GHz. This is due to mechanical stress and twisting caused by body movements. Replacement of the cables is very expensive. Extra caution during body movements is required during the measurements. Metal-shielded cables were introduced in the later measurements, but they cause more stress on the antenna connectors because they are heavier than plastic-shielded cables. Furthermore, their use makes more difficult to place antennas on the body. The length of the 60 GHz cables is chosen 2 m because longer cables will introduce much more loss which is difficult to compensate. However, the use of these relatively short cables gives rise to additional restrictions on the body movements. A small piece of semi-rigid coaxial (Anritsu© V086MM-30CM) was used to connect the antenna and the flexible cable. Because the semi-rigid cable can support stress from both the antenna and the flexible cable, it makes placement of the antenna on the body more easy. Also, one major concern about cables is that the effect of unwanted scattering from the cables will result in a negative effect on the measured channel data. Besides, the cables may radiate as an antenna at lower frequencies, but at 60 GHz, radiation from the cables is very low, especially from metal-shielded cables. By using semi-rigid cables, cables were carefully routed to avoid being in the path of the measured channel. Hence, the unwanted scattering of signals from the cables can be minimised thanks to the quasi-optical characteristics of 60 GHz waves.

4.2.4 Amplifiers

In order to improve the overall measurement system dynamic range at 60 GHz, two amplifiers were used, namely, a 58 to 62 GHz medium power amplifier (Spacek Labs Inc. model no: SP604-13-12W) and a 55 to 65 GHz low noise amplifier (Spacek Labs Inc. model no: SL6010-15-6).

4.3 Radio Channel Measurement Method

Channel measurements characterising wireless body area networks involve putting antennas on the human bodies. There are two factors which make these channel measurements different and even more difficult than other radio channel measurements. Firstly, geometry changes due to body movements result in dramatic changes of the channel properties and these changes must be captured by the measurements. Secondly, the measured data include both antennas and the channel properties and de-embedding antennas from the measured transmission channel is very difficult. In addition, body movements have a significant effect on the measured channel data, but it is impossible to repeat the movements exactly, even when the human subject appears to perform periodic movements. Hence, characterisation of body dynamics becomes important as well. Finally, the system designer is primarily interested in models extracted from a large number of measurements. It is desirable to measure channels of body area networks in a person's daily life and in different environments. However, due to the restrictions imposed by the instrument and cables, this is hard to achieve.

Figure 4.1 shows the on-body channel measurement with the VNA and cables. For on-body channels, both the transmit and receive antennas are on the same body. For off-body channels, the second antenna is placed on the object in the vicinity of the subject, or on another person nearby.

In the on-body channel measurement setup, flexible coaxial cables are used to connect antennas to the VNA. The amplitude and phase of S_{21} or signal can be measured. The VNA is typically bench-mounted close to the subject. The normalisations of measured data were performed before or after each measurement. The normalisation process is fol-

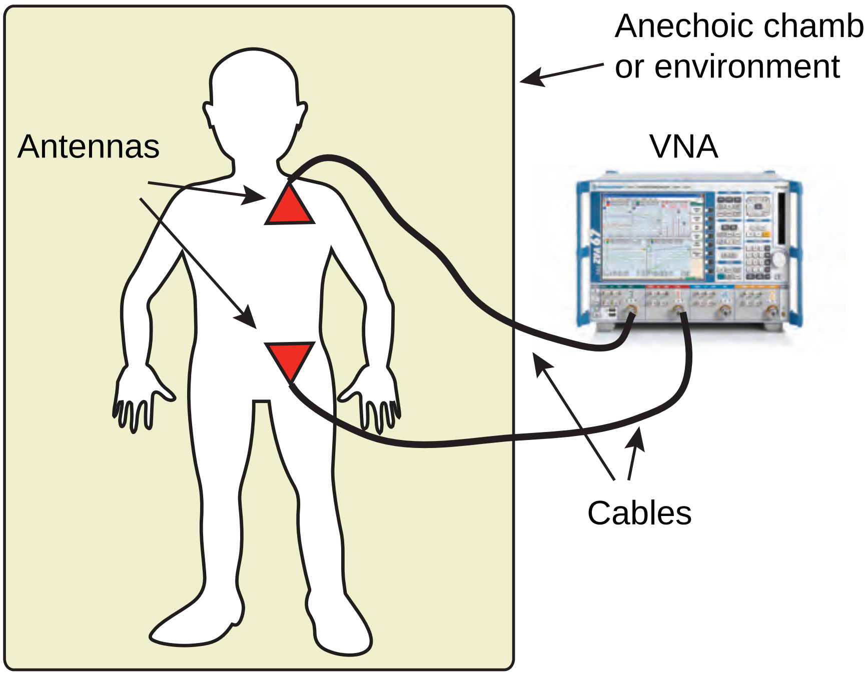

Figure 4.1: On-body channel measurement with vector network analyser (VNA) and cables.

lowing: 1)the cables from input port and output port of the VNA were connected through a through calibration kit; 2)S_{21} was measured with cable movements; 3)using RMS value of measured cable data to normalise the measured channel data. One exception is in covertness measurement where a 4m-free-space normalisation using two horn antennas at 60 GHz was performed, which will be described in Chapter 7.

Table 4.1 summarises the details of VNA parameters for channel measurements conducted in this thesis.

4.4 Antenna Radiation Pattern and Gain Measurement Method

Figure 4.2 shows the block diagram for 60 GHz antenna radiation pattern and gain measurement setup. The frequency multiplier and mixer were used in this measurement to

Table 4.1: VNA parameters for channel measurements

Measurement	Power	IF BW	Noise floor[1]	Sweep time	Samplings
60GHz channel(mono)[5]	10 dB	100Hz	−91.6dB	200.7s	20001
60GHz channel(horn)[5]	10 dB	1kHz	−85.7dB	62.1s	60001
60GHz interference[6]	0 dB	1kHz	−110dB	62.1s	60001
2.45GHz interference[6]	0 dB	1kHz	−97dB	62.1s	60001
60GHz CIR[6]	10 dB	1kHz	−110dB	62.1s	60001
2.45GHz CIR[6]	10 dB	1kHz	−97dB	62.1s	60001
60GHz detection[7]	0 dB	1kHz	−56.5dB	62.1s	60001
60GHz channel(Yagi)[8.6]	10 dB	100Hz	−89.6dB	10s	1001
60GHz channel(slot ant.)[9.4]	10 dB	1kHz	−70.4dB	135.3ms	504

[1] This is the RMS noise floor after normalisation.

up-convert and down-convert the signal frequency. The interface of 60 GHz side of the multiplier and mixer is the WR15 waveguide. Hence, the waveguide transitions were designed to feed the antennas in this measurement. Figure 4.3 shows the measurement setup inside the anechoic chamber. The mixer was placed underneath the rotating table, so it rotates with table during the pattern measurement. A bent waveguide was used to connect the mixer with the antenna under test (AUT) and make sure the AUT aligned with the horn antenna. Due to this setup, the phase center of the AUT cannot coincide

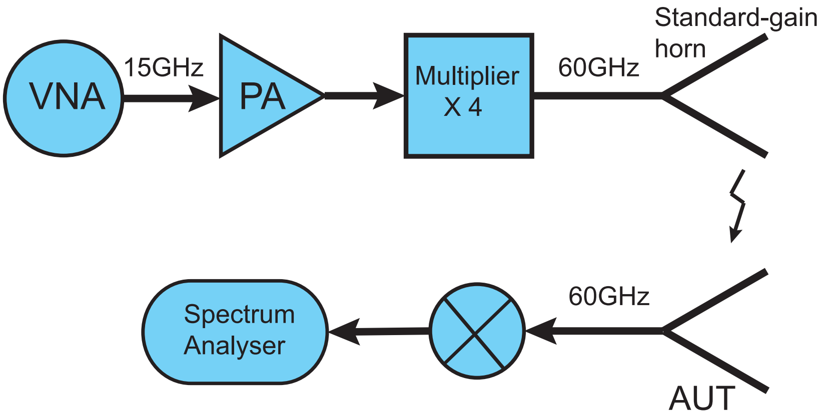

Figure 4.2: Block diagram for 60 GHz antenna radiation pattern measurement.

with the rotating axis of the rotating table. Hence, measurement errors are expected. For the gain measurement, the gain-transfer method was used. This technique utilizes a gain standard (with a known gain) to determine absolute gains. The procedure requires two sets of measurements. In one set, using the AUT as the receiving antenna, the received power into a matched load is recorded. In the other set, the AUT is replaced by the standard gain antenna (20dBi standard gain horn in this thesis) and the received power into a matched load is recorded. In both sets, the geometrical arrangement is maintained intact except replacing the receiving antennas, and the input power is maintained the same. Hence, by comparison of two measured powers, the relative gain between the AUT and standard gain antenna can yield the absolute gain of the AUT.

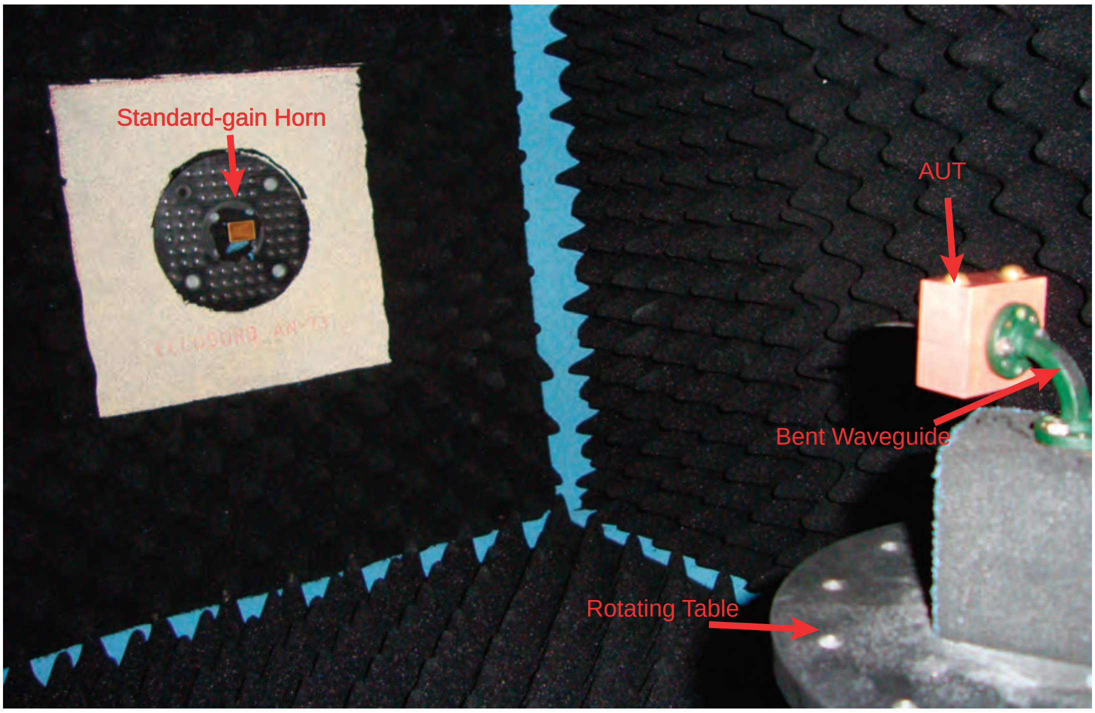

Figure 4.3: 60 GHz antenna radiation pattern measurement.

4.5 Summary

In this chapter, the channel measurement methods for body area networks were briefly reviewed. The equipment and the measurement arrangements were described. The advantages and limitations of the cable-based method were also addressed. Antenna radiation pattern and gain measurement methods are also introduced.

CHAPTER 5

60 GHZ ON-BODY CHANNELS CHARACTERISATION USING MONOPOLE AND HORN ANTENNAS

5.1 Introduction

In this chapter, a number of on-body propagation links between body-mounted antennas are investigated experimentally at 60 GHz. The antennas used in these measurements are monopole and horn antennas. One is omni-directional with low gain and the other is directional with high gain. Variations of the carrier wave magnitude with random body movements were measured and a statistical analysis for the changing on-body channels was performed. The investigated links were chosen to represent a body area network which consists of a number of wearable devices placed on different parts of the human body. As shown in Figure 5.1, these locations include positions on the waist (e.g. mobile phone, or other body area aggregator), head (e.g. headphones, Google glasses), wrist (e.g. smart watch, physiological sensor), chest and upper arm (e.g. repeater nodes necessary to establish longer links). Besides, the effect of polarisation on the path gain was also analysed by using Millitech© orthomode transducers (OMT) [182] in the measurements.

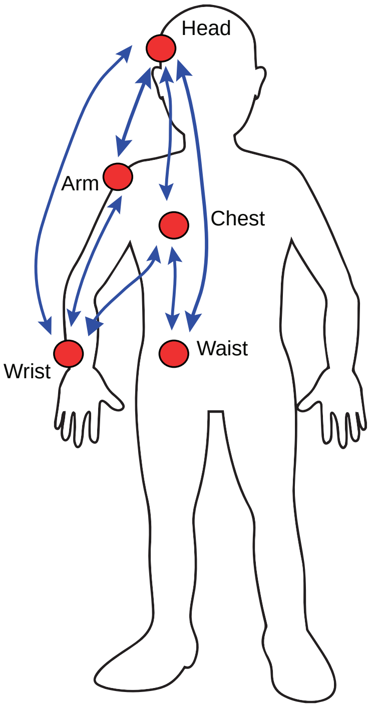

Figure 5.1: Antenna positions and channels investigated in the measurements.

5.2 Measurement Procedure

On-body channel measurements were conducted in an anechoic chamber using a Rohde & Schwarz ZVA 67 VNA. The direct access ports of source and receiver were used to maximise dynamic range of the measurements by bypassing the directional couplers in the VNA. The received signal magnitudes were measured during the measurements. Figure 5.2 shows antennas used in the measurements. In monopole measurements, two quarter-wavelength monopole antennas with a circular ground plane of a 25 mm diameter were connected to the VNA through two 2 m long coaxial cables. The loss in the cables was measured as the cables were flexed randomly during a through calibration, before and after the measurements. It was found that the stress caused by rapid movements lead to deterioration of the cable performance, as the loss in the cable increased by 0.7 dB after the measurements were done, and the standard deviation of the logarithmic loss increased from 0.3 to 0.5 dB. In the horn measurements, two 17 dBi scalar horn antennas [183] at 60 GHz from Millitech© were used. Each horn was connected to two ports of a 4-port VNA through an OMT, two waveguide-to-coaxial connector adaptors and two armored coaxial cables. Thus, two orthogonal polarizations of each scalar horn could be accessed simultaneously.

The settings for the analyser sweep were different for horn and monopole measurements. For monopole measurements, the VNA was set to 60 GHz center frequency and 1 Hz frequency span, with 20001 sweep points taken over a sweep time of 200.7 s. For horn measurements, the VNA generated a 60 GHz carrier wave frequency but the sweep time was 62.1 s with 60001 samples in a sweep. The wider IF bandwidth of the VNA was used in the horn measurements in order to compensate the switching time of the two sources in the VNA and the narrower IF bandwidth used in the monopole measurements to lower the noise level. The 1 Hz frequency span, chosen due to the VNA setting limitations, is much smaller than the maximum Doppler frequency shift (which was estimated to be about 200 Hz, assuming the speed of body movements of 1 m/s), and therefore should not have a notable effect on the results. It worth mentioning that the sampling frequency of about 100 samples/s in the monopole measurements is less than that required by the sampling theorem, that is, 400 samples/s (two times the Doppler frequency shift). Therefore, the measured signal may be somewhat under-sampled. This, however, should not affect the statistics of the signal magnitude provided that a sufficiently large data set is available. The output power of the VNA was set to 10 dBm for both measurements. A through normalisation was performed before the measurements to remove the effects of cables and connectors, but the antennas were not included.

The test subject wearing the antennas was a male of a 178 cm height and 74 kg weight. The subject was wearing a conformal wetsuit made of approximately 1 mm thick nylon fabric. The antennas had to be supported by an expanded polystyrene foam block above the body because of the coaxial probe feed at the back of the antenna, and were held in place securely with belts and self-adhesive tape. The ground plane of the monopoles was parallel to the body with a distance of approximately 13–15 mm from the skin. For horn antennas, two cables were used to connect each port of OMT to the VNA. One corresponds to a polarisation perpendicular to the skin the other corresponds to the polarisation parallel to the skin. The distance between the body surface and the horn antenna was about 10–12 mm. Figure 5.3 shows the antenna placements on the subject for the head-arm link.

A number of on-body propagation channels were measured, including waist-chest, chest-head, head-upper arm, and upper arm-wrist. During each measurement a random sequence of movements was performed by the test subject, simulating various everyday activities, such as reading, writing, eating, operating electronic equipment (e.g. computers and mobile phones), walking, exercising, etc. The received signal magnitude when two cables were connected together with cable movements was measured. And the overall RMS of this value was used to normalise the measured signal magnitude for each measurement in order to remove the effects of cables and connectors.

A separate motion capture measurement using VICON© was carried out to capture body movements and measure the distances between different nodes on the surface of the body. More details of the measurement are described in [115]. The distance data from this measurement were used in the following section.

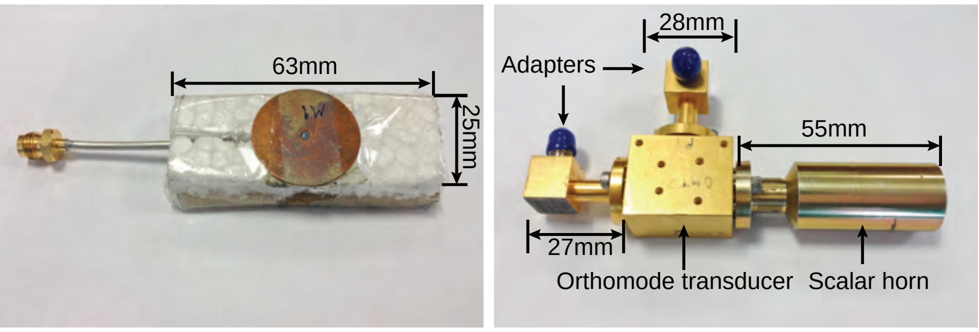

(a) (b)

Figure 5.2: Antennas used in the channel measurements: (a) monopole antenna, (b) scalar horn antenna with orthomode transducer.

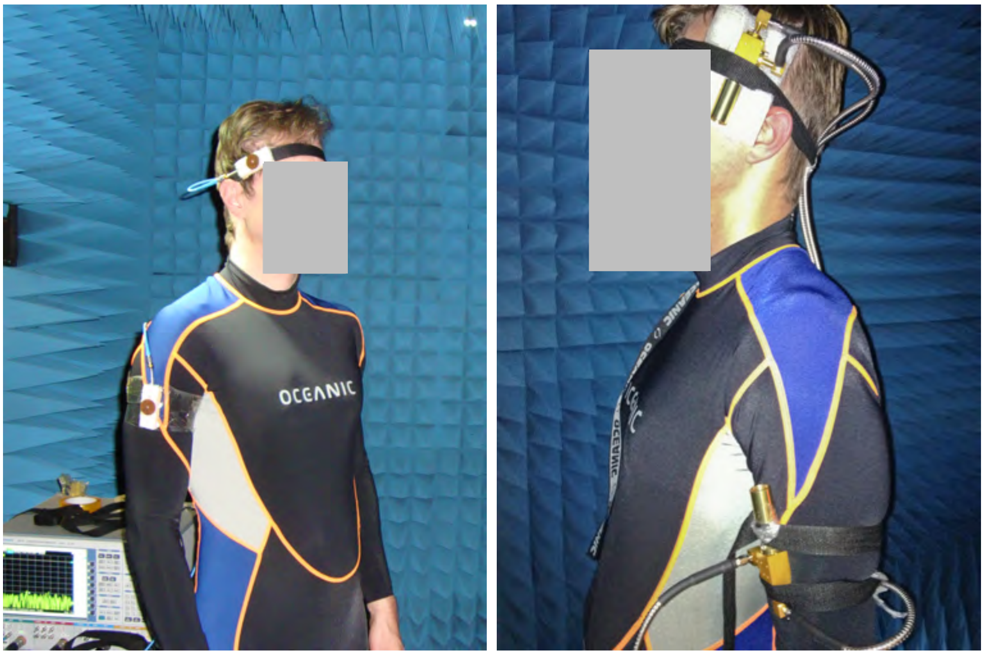

(a) (b)

Figure 5.3: Antenna placement on the subject for head-arm link: (a) monopole antenna, (b) horn antenna with orthomode transducer.

5.3 Results and Discussions

Figure 5.4 shows empirically derived cumulative distribution functions (CDFs) of the measured path gain data for the arm-wrist channel. The path gain is defined as the ratio of the power at the output of the receiving antenna to the power at the input of the transmitting antenna. These data were produced for all possible postures of the arm-wrist channel during the measurement. The CDFs for 4 polarization arrangements are shown, namely, VV (both antennas polarized vertically, i.e. perpendicularly to the body surface), VH (transmitting antenna is vertically polarized while the receiving antenna is horizontally polarized, i.e. tangentially to the body surface), HV (transmitting antenna is horizontally and receiver is vertically polarized), and HH (both antennas are horizontally polarized). The corresponding results for VV-oriented monopoles with circular ground planes are also presented in the figures for comparison. As shown in the figure, the monopole antennas provide a significant extra path gain compared to the horn antennas. The median path gain of monopole is more than 11 dB higher than that of horns as shown in Table 5.1. It is due to movements of the arm of the subject, which results in loss of line-of-sight communications between two horn antennas while because of omni-directionality, the communications between two monopoles were sustained. For polarisation comparisons, the HH polarisation is the dominant polarisation for the most of time.

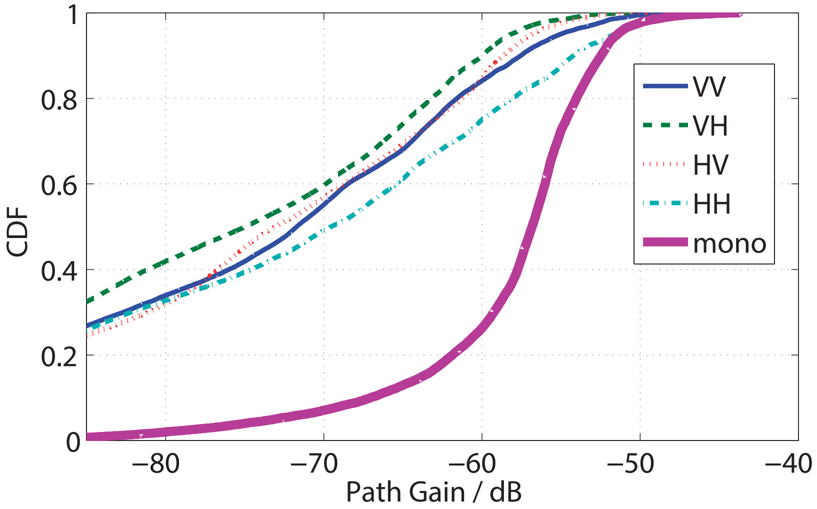

Figure 5.4: CDF for the arm-wrist channel.

The chest-waist channel, CDFs for which are shown in Figure 5.5, is a relatively stable channel due to limited relative movements between the two antennas. Directive antennas realise their advantage over monopole antennas in achieving higher path gain in this kind of channel. The median path gain of horns is about 18 dB higher than that of monopoles. Depolarization in this channel is small, and the VV polarization setup produces the strongest signal overall.

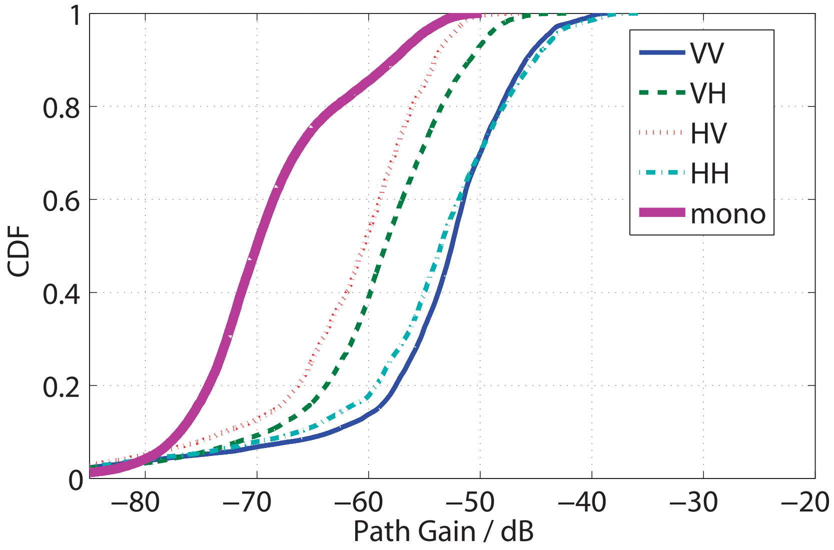

Figure 5.5: CDF for the chest-waist channel.

Figures 5.6 and 5.7 show the path gains for the chest-wrist and head-wrist channels. Two monopole antennas achieve the communications above the measurement noise floor in a wide range of positions and orientations relative to each other in this channel, but horns were rarely pointing directly at each other. As shown in Table 5.1, the median path gain of horn antennas is below the noise level. Therefore, omni-directional antennas are more suitable for the wrist-terminated channels.

Figure 5.8 shows the path gain for the head-arm channel. As shown in Figure 5.2, one horn antenna was placed on the right side of the head and the other horn antenna was placed on the front of right arm. Hence, VH and HV are co-polarised channels, which have 4–5 dB extra median path gain over the VV and HH channels. Monopoles gave a

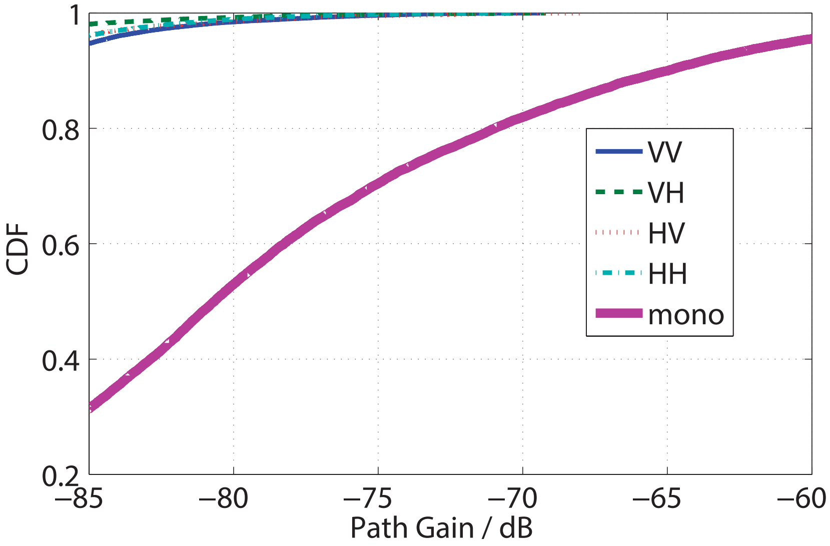

Figure 5.6: CDF for the chest-wrist channel.

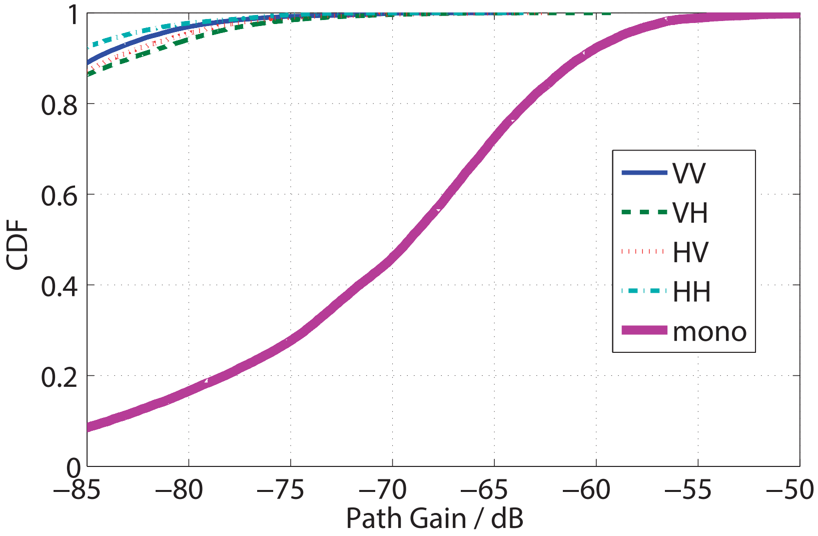

Figure 5.7: CDF for the head-wrist channel.

higher path gain for most of the time due to their wide coverage of the body area.

Figures 5.9 and 5.10 show the path gains for head-chest and head-waist channels. The main difference between two channels is the physical path length distance. Because of the placement of antennas, the VH and HV channels are the co-polarised ones. As indicated in Figure 5.9, directional antennas show a significant advantage over omni-directional ones,

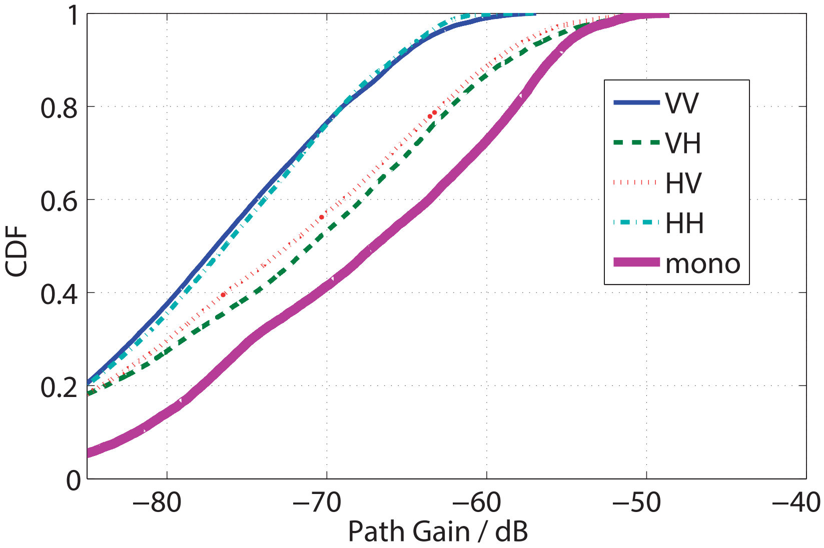

Figure 5.8: CDF for the head-arm channel.

both in short and long communication links. More than 20 dB extra median path gain achieved by using horn antennas. For the head-waist channel, the path gain difference between co-polarised channels (VH and HV) and cross-polarised channels (VV and HH) is small. This is due to severe depolarisation caused by the longer distance between antennas and movements of belly and diaphragm.

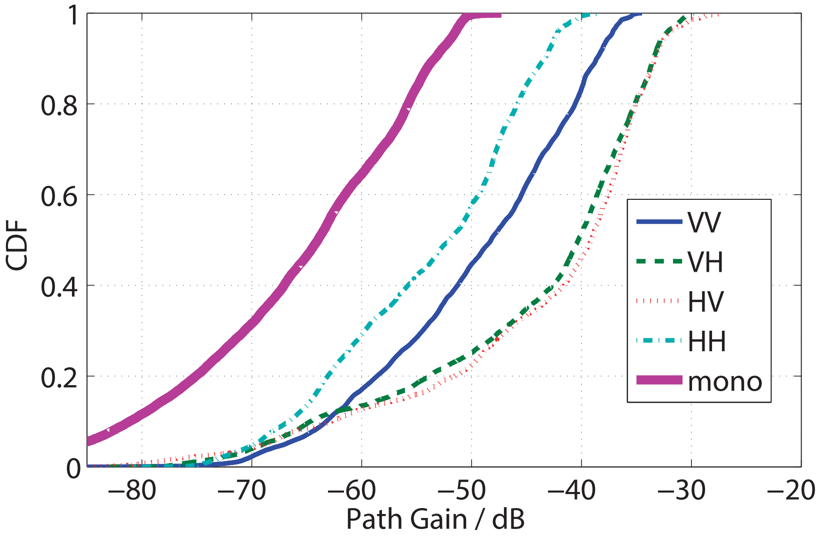

Figure 5.9: CDF for the head-chest channel.

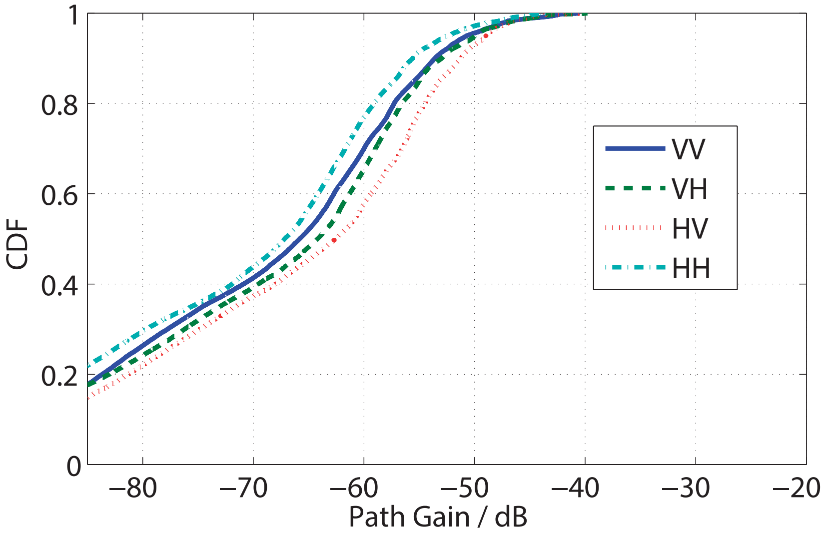

Figure 5.10: CDF for the head-waist channel.

Table 5.1: Median of path gain (dB) for on-body channels with horns and monopoles

	VV	VH	HV	HH	mono	distances[2](mm)
Arm-Wrist	−70.8	−73.5	−71.8	−68.2	−56.8	336.9
Chest-Waist	−52.5	−58.5	−60.9	−53.4	−70.0	246.1
Chest-Wrist	×[1]	×[1]	×[1]	×[1]	−80.6	377.9
Head-Waist	−67.0	−65.0	−63.5	−68.0	×[1]	654.8
Head-Arm	−77.6	−71.8	−73.4	−77.0	−67.0	412.9
Head-Chest	−48.5	−40.9	−39.7	−51.5	−63.9	393.2
Head-Wrist	×[1]	×[1]	×[1]	×[1]	−69.1	673.5

[1] signal below noise

[2] the median distances were calculated using distance data from optical motion capture and they are line-of-sight distances, sometimes even through the human body.

Figure 5.11 shows the percentages of the dominant polarisation for on-body channels using horn antennas. The dominant polarisation is the polarisation gives the best path gain in a particular channel for most of the time. There is no single dominant polarisation for all on-body channels. This is mainly because the depolarisation caused by body movements for different channels is different. However, polarisation diversity techniques may be used to improve the path gain for on-body channels.

Figure 5.11: Percentage of dominant polarisation for on-body channels with horn antennas.

Further statistical analysis has been performed for measured path gains using monopole antennas[1]. A fragment of the measured signal variation is shown in Figure 5.12. It shows that two different types of fading are present at the same time: small short-term variation is superimposed onto much larger and slower long-term variation. Hence, the time-varying complex channel transfer function can be represented in the following form:

$$\tilde{h}(t) = \tilde{s}(t) \cdot l(t) \tag{5.3.1}$$

where

$$l(t) = \sqrt{\langle | \tilde{h}(t) |^2 \rangle_{\Delta t}} \tag{5.3.2}$$

is the long-term fading component which slowly varies with time, provided $\langle \cdots \rangle_{\Delta t}$ represents local averaging over a short-time period Δt. And $\tilde{s}(t)$ is a fast varying complex factor whose magnitude, $s(t) =| \tilde{s}(t) |$, represents the short-term component. Then, given

---

[1] This data analysis was done by Dr. Yuriy Ivanovich Nechayev [184].

a transmitted complex signal complex $\tilde{x}(t)$, the received complex signal envelope is

$$\tilde{r}(t) = \tilde{s}(t) \cdot l(t) \cdot \tilde{x}(t) + \tilde{n}(t) \tag{5.3.3}$$

where $\tilde{n}(t)$ is the complex random thermal noise at the receiver, and $\mid \tilde{x}(t) \mid = 1$ in this measurement setup because the data was normalised before the measurement.

By multiplying Equation (5.3.3) by its complex conjugate and averaging over a time period Δt, which should be sufficiently short for the long-term component $l(t)$ to remain approximately constant, we arrive at,

$$l^2(t) = \langle r^2(t) \rangle_{\Delta t} - \langle n^2(t) \rangle_{\Delta t} \simeq \langle r^2(t) \rangle_{\Delta t} \tag{5.3.4}$$

When SNR has a high value, an approximation $r(t) \gg n(t)$ was made. One question that arises is what Δt should be used? The criteria are that there are sufficient short-term fading oscillations (approximately 4 to 6) inside that window and yet small enough compared to the time scale of the long-term variation [185]. The local RMS long-term component $l(t)$ was calculated using Equation (5.3.4) with the window size $\Delta t = 0.2$ s. It is worth mentioning this window size is probably not the optimal value. Then,

$$s(t) = \frac{\mid \tilde{r}(t) - \tilde{n}(t) \mid}{l(t)} \simeq \frac{r(t)}{l(t)} \tag{5.3.5}$$

Therefore, these two kinds of fading can be separated in the post-processing by means of averaging the received signal over a sufficiently short period time Δt, where the long-term component to remain approximately constant, to remove the short-term component based on Equation (5.3.4). The short-term component can be calculated by subtracting the long-term component from the measured signal envelope in logarithmic form based on

Equation (5.3.5). In this calculation, the threshold of the level not exceeded by noise 95% of the time was chosen for the SNR consideration. The data below this threshold were excluded from the analysis to eliminate the effect of noise on the channel characteristics.

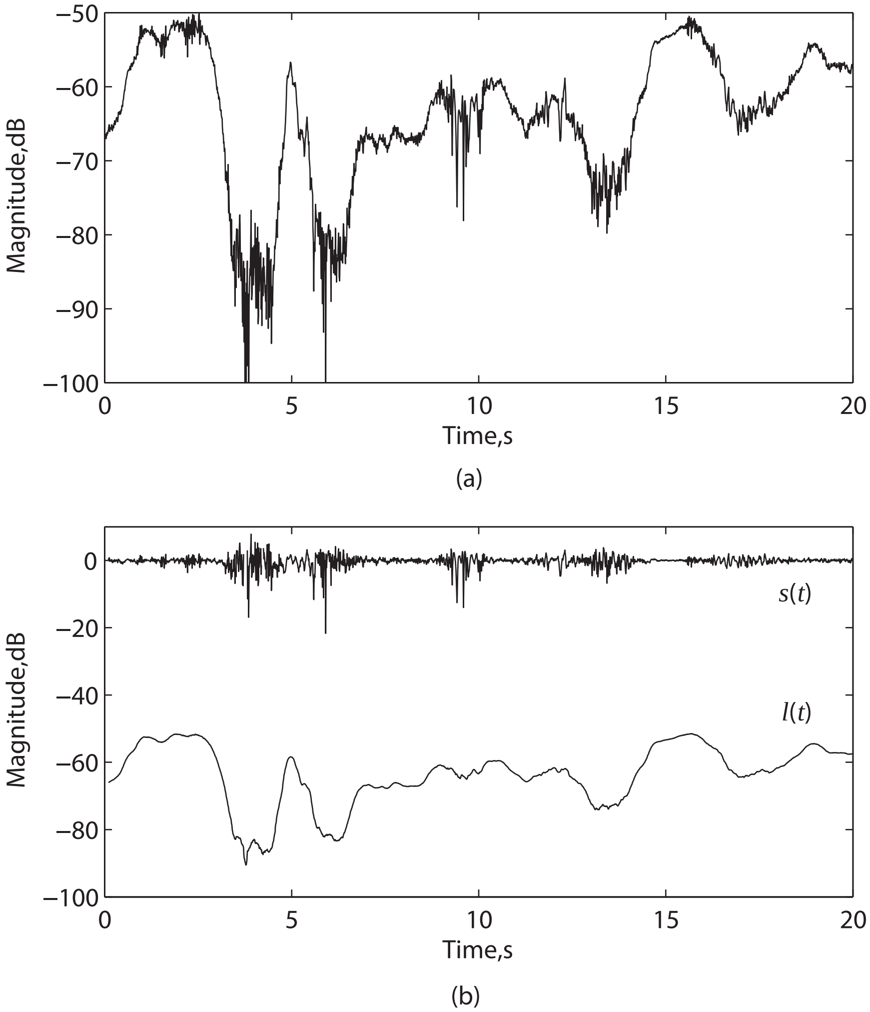

Figure 5.12: Time variation of measured signals: (a) Measured signal envelope (b) Long-term, $l(t)$ and short-term, $s(t)$, components.

The level-crossing rate (LCR) and average fade duration (AFD) of the long-term fading for four channels were also calculated and are shown in Figure 5.13 and 5.14. The long-term fading is mostly caused by shadowing, antenna pointing error, polarisation mismatch and distance changes. These variations are fairly slow with typical level crossing rates

< 1 s^{-1} and average fade durations > 0.1 s. However, two channels with the wrist node exhibit much larger LCRs and smaller AFDs in a 20 dB range around the median than the other two channels. This is because that the highly volatile nature of the movements when the antenna is on the wrist. The channels from the arm and the chest to the head change at a much slower rate but stay in the fade longer.

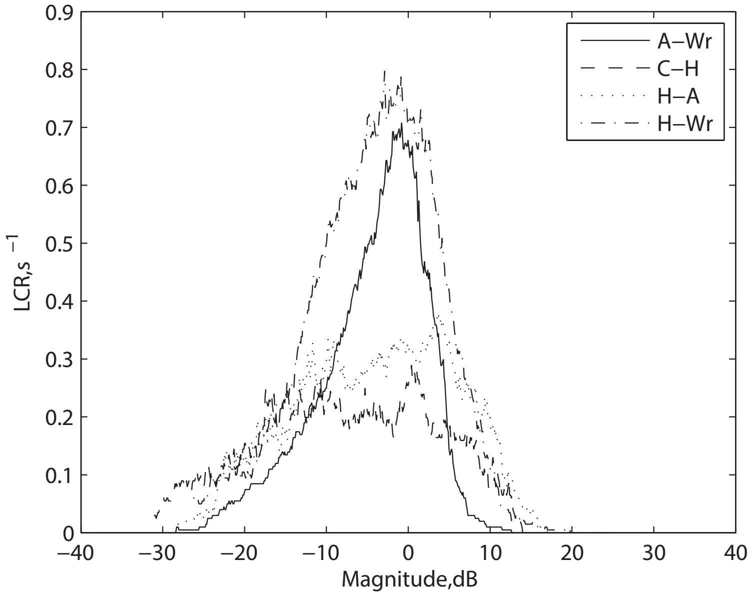

Figure 5.13: LCR of $l(t)$ normalised to its median, H(Head),A(Arm),C(Chest),Wr(Wrist)

Results also show that the attenuation in the channels is much stronger at 60 GHz than that at lower frequencies. Thus, the separations between communication nodes have to be short (approximately less than 30 mm) and the link should be line-of-sight for reliable on-body communications. Multipath fading at 60 GHz is much less prominent than at lower frequencies and only becomes significant when the signal level is low.

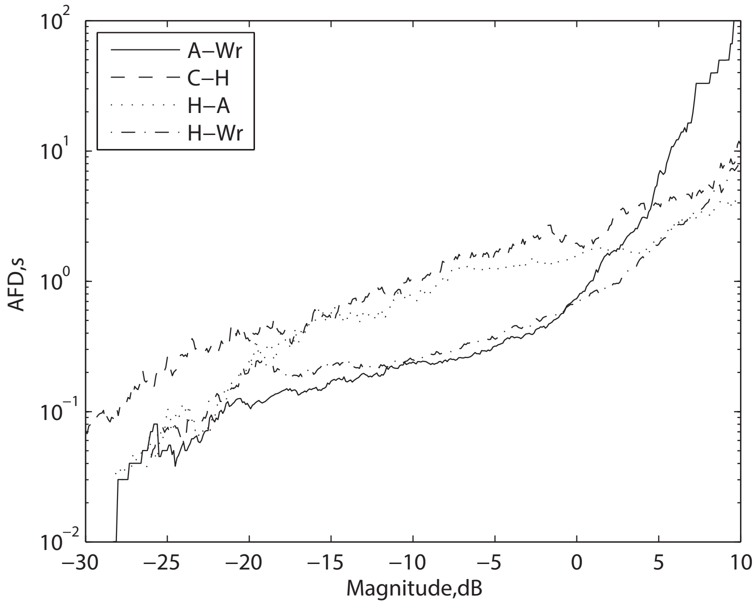

Figure 5.14: AFD of $l(t)$ normalised to its median, H(Head),A(Arm),C(Chest),Wr(Wrist)

5.4 Summary

In this chapter, 60 GHz on-body channels have been investigated using monopole antennas and horn antennas. Monopole antennas represent omni-directional antennas with relatively low antenna gain and horns represent directional antennas with high gain. Channels related to the positions of the head, arm, wrist, chest and waist were studied in terms of measuring and characterising the path gain of the channel. For horn measurements, orthomode transducers were used to investigate the polarisation dependence of path gain for on-body channels. Studies show that horn antennas demonstrate significant advantage in relatively stable channels such as the chest-waist channel by improving path gain compared to monopole antennas. Directional antennas also help to extend the communication distance due to its higher gain. However, in the more mobile channels, such as the wrist-terminated ones, monopole antennas achieve better performance because of their wider radiation coverage, while horn antennas have much lower probability of pointing at each other. In addition, body movements cause the depolarisation of the channels, which sometimes results in significant degradation of channel performance, hence no single polarisation outperforms others in all on-body channels. Dual-polarised or circularly polarised antennas may be helpful for improving the on-body channel performance. Finally, for different channels, different antenna characteristics are required. Requirements such as antenna gain, antenna beamwidth, polarisation must be taken into account.

CHAPTER 6

INVESTIGATION OF INTER-USER INTERFERENCE OF WIRELESS BODY AREA NETWORKS AT 60 GHZ

6.1 Introduction

THIS chapter investigates the inter-user interference between two persons with body movements in an indoor environment at 60 GHz and 2.45 GHz. Both omnidirectional antennas (monopole antenna) and directional antennas (horn antenna) were used in the measurements. The interfering signal strength variations and CIR were measured and characterized. Comparisons of interference signals and carrier-to-interference ratio between 60 GHz and 2.45 GHz are made.

6.2 Measurement Procedure

6.2.1 Interfering signal strength variation measurements

Interfering signal strength variation measurements were performed in a laboratory in the Electronic, Electrical and Computer Engineering building at the University of Birmingham. Antennas used in these measurements are monopole antennas at 2.45 GHz, monopole antennas at 60 GHz and 20 dBi gain standard horn antennas at 60 GHz. For each measurement, two identical antennas were placed on the bodies of two men of the height 1.65 m and 1.83 m, respectively. Antenna placements on the body were at the head, the abdomen and the wrist positions as shown in Figure 6.1. Hence, six interference channels were investigated, namely abdomen-abdomen, head-abdomen, head-head, head-wrist, wrist-abdomen, wrist-wrist. Only one channel was measured during each measurement. Figure 6.2 shows a 2.45 GHz monopole antenna placed on the wrist of human body. The ground plane of this antenna is 80×80 mm^2. The distance between the antenna and the body surface is 20 mm. Figure 6.3 shows the placements of 60 GHz monopole antenna on the human body. This antenna is made of a 60 GHz coaxial cable. The ground plane diameter is 25 mm and its height above the skin is approximately 13 mm. The loss in the short feed cable of the monopoles is less than 0.5 dB. Monopoles have a near omni-directional pattern in the azimuth plane tangential to the body surface.

In order to improve the dynamic range at 60 GHz, two amplifiers were used during the measurements, namely, a power amplifier (Spacek Labs Inc. SP604-13-12W) and a low noise amplifier (Spacek Labs Inc. SL6010-15-6). They achieve 30.8 dB gain in total at 60 GHz with this measurement setup. Placements of a 60 GHz standard gain horn antenna with an amplifier on the body are shown in Figure 6.4. The horn antenna used

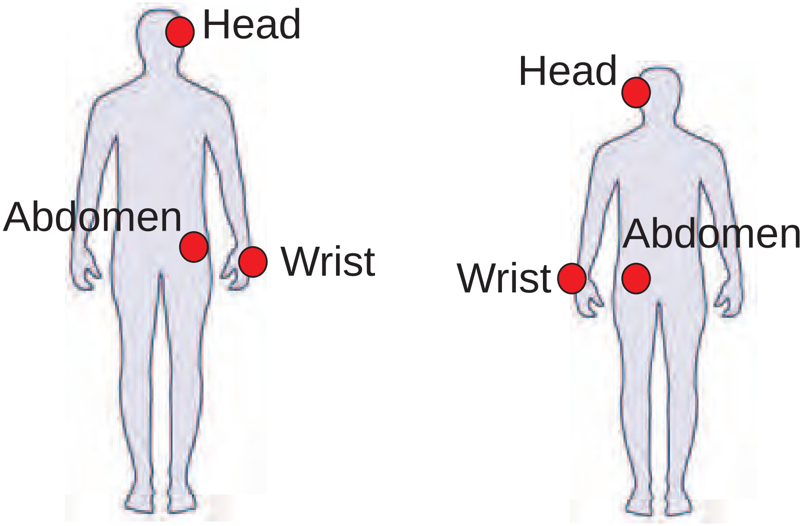

Figure 6.1: Antenna placements on the human body.

is Flann© standard gain horn Series 240 model 25240. The gain of antenna is 20 dBi. When the horn was placed on the wrist and abdomen, the aperture of the antenna was facing upwards. When the horn was placed on the head, the aperture of the antenna was facing downwards.

Figure 6.2: Monopole antenna on the wrist (2.45 GHz).

During the measurements, two subjects performed random movements and rotations with-


(a) (b) (c)

Figure 6.3: Placements of monopole antenna with amplifier on the body (60 GHz): (a) Head, (b) Wrist, (c) Abdomen.

in a 1 × 2.5 m^2 area in the lab environment as shown in Figure 6.5. The room contained equipment, tables, and chairs and computers, thus providing a rich multipath propagation environment. Random movements include walking, waving arms, rotating trunk, squatting, bending trunk, running, etc. It is worth mentioning that this scenario should be the worse case compared with daily scenarios because two persons are very close to each other. In a real situation, the interference should be much lower at 60 GHz because the distance between persons is much longer. The S_{21} during the various activities was measured with a Rohde & Schwarz© ZVA 67 VNA. The source and receiver direct access ports on the ZVA 67 were used, thus bypassing the directional couplers in order to maximize the dynamic range of the measurements. For this 60 GHz measurement setup, the analyzer was set to 60 GHz CW with 60001 sweep points taken over a sweep time of 62.1 s. The output power and measurement bandwidth were set to 0 dBm and 1 kHz respectively. Two 2 m long cables were used to connect antennas with the analyzer. The loss in the cables was measured as the cables were flexed randomly during a through calibration, before the measurements and afterwards. It was found that stress caused by rapid movements lead to deterioration of the cable performance, as the loss in the cable increased by 1.5 dB after measurements were done. The overall RMS signal strength in the cables was used to normalize the measured signal magnitude, and amplifier gain was removed in the data processing. With such a setup, the RMS noise level was at −110 dBm. For 2.45 GHz measurement, the VNA settings were the same with 60 GHz measurements. The output power is 0 dBm. The analyser sweep was set to 2.45 GHz centre frequency and 1 kHz frequency span with 60001 sweep points taken over a sweep time of 62.1 s. The RMS noise level at 2.45 GHz is −97 dBm. The loss in the cable due to movements is negligible at 2.45 GHz.

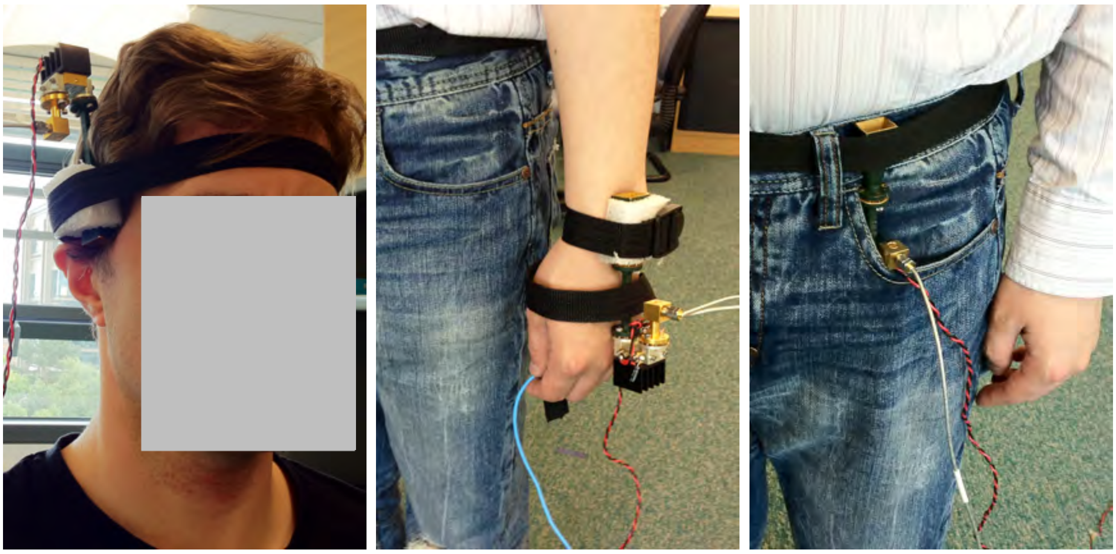

(a) (b) (c)

Figure 6.4: Placements of horn antenna with amplifier on the body (60 GHz): (a) Head, (b) Wrist, (c) Abdomen.

6.2.2 Carrier-to-interference ratio (CIR) measurements

The carrier-to-interference ratio measurements were conducted in the same environment with the same VNA setting except that the output power was set to 10 dBm. One

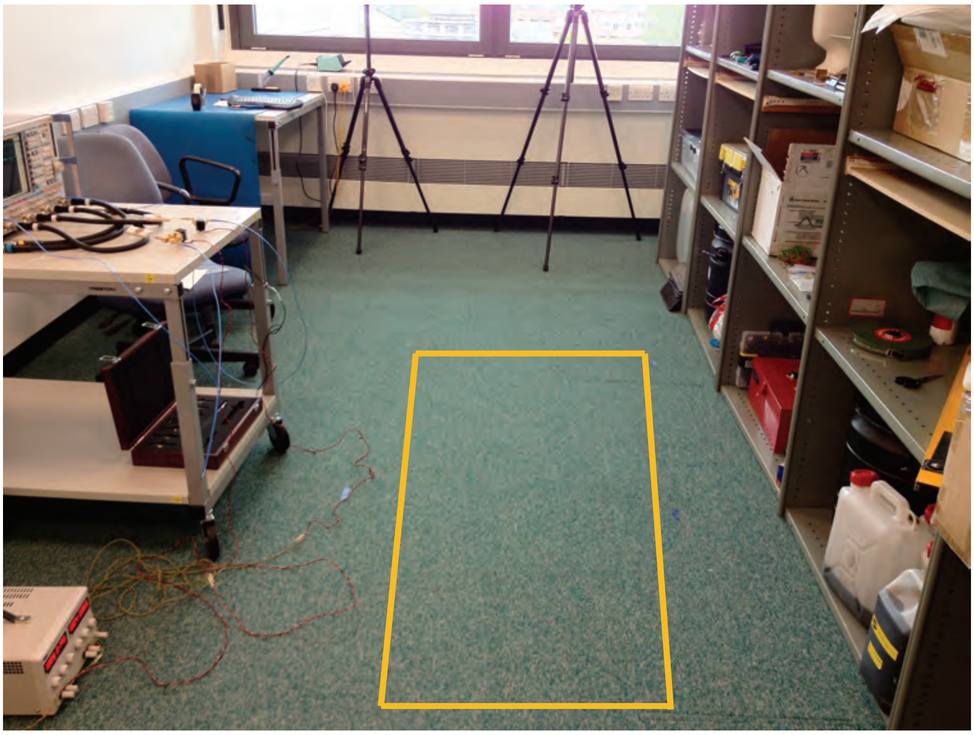

Figure 6.5: Lab environment.

monopole antenna and one horn antenna were placed on each subject for 60 GHz measurements. Only one antenna was in the transmitting mode, whilst the other three antennas were receiving. Hence, there were three channels measured simultaneously in this experiment. The channel on the same subject is defined as the wanted-signal channel. The other two between two subjects are defined as interference channels. Two body channels were measured: the head-abdomen channel and the head-chest channel. Figure 6.6 shows examples of antenna placements for both channels. We define the following format to illustrate the antenna placement on two subjects: $Antenna\ type, Position - Antenna\ type, Position$. Abbreviations are used to represent antenna positions: H for head, C for chest and A for abdomen. In this format, the first antenna was the transmitting antenna. The others were receiving antennas. The same type of antenna was placed on the same position for each subject. Therefore, the following measurements were measured:

$$HornH - MonopoleA$$
$$MonopoleA - HornH$$
$$HornH - MonopoleC$$
$$MonopoleC - HornH$$

For example, $HornH - MonopoleA$ represents that the case in which horn antenna and a monopole antenna were placed on the head and the abdomen respectively for each subject. The horn antenna on the head of Subject 1 was transmitting. The others were receiving. Because of reciprocity of channels, these channels measured are equivalent to the scenarios that three antennas are transmitting and one antenna is receiving which is the situation when interference occurs. Figure 6.7 shows the equivalent interference scenario for the measurement setup shown in Figure 6.6(b). The reason for doing the measurement this way was that there were not enough power amplifiers available.

In order to eliminate ambiguity, the following results and discussions will be presented in the context of the real interference scenario which means that the transmitting antenna in our measurements will be called the receiving antenna for the interference situation. Four 2 m coaxial cables were used to connect four antennas with the VNA. A power amplifier was always used with the transmitting antenna at 60 GHz. The gain of power amplifier is up to 23 dB at 60 GHz. A low noise amplifier was connected with the receiving horn antenna because high gain antenna suffers more significant shadowing effects at 60 GHz. The gain of low noise amplifier is 16 dB. This gain was subtracted from the measured data for that certain channel. Normalisation has been performed for all four ports. Movement of cable results in up to 1 dB fluctuation of the received signal. During the measurements, two subjects were performing random movements within the fixed area. Each sweep took 62.1 s to collect 60001 sampling points. Three channels were measured simultaneously when subjects were performing movements. For 2.45 GHz measurements, four monopole antennas were used, two on each subject. Other settings were the same as that at 60 GHz except that no amplifier was used at 2.45 GHz.

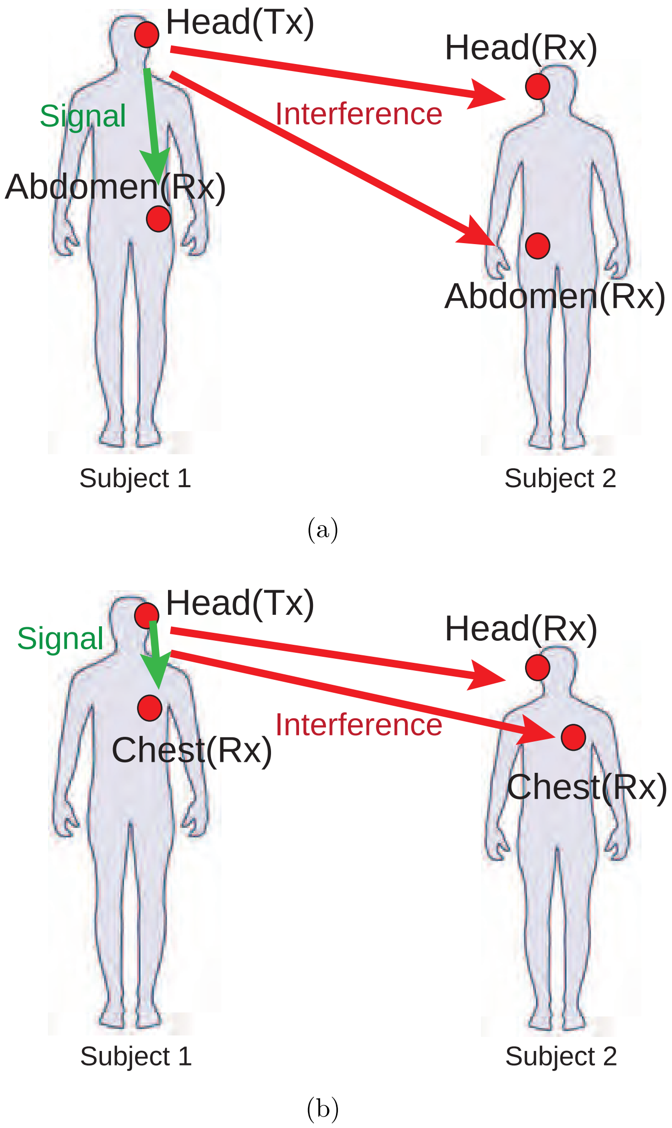

Figure 6.6: Examples of antenna placement for CIR measurements: (a) Head-abdomen channel, (b) Head-chest channel.

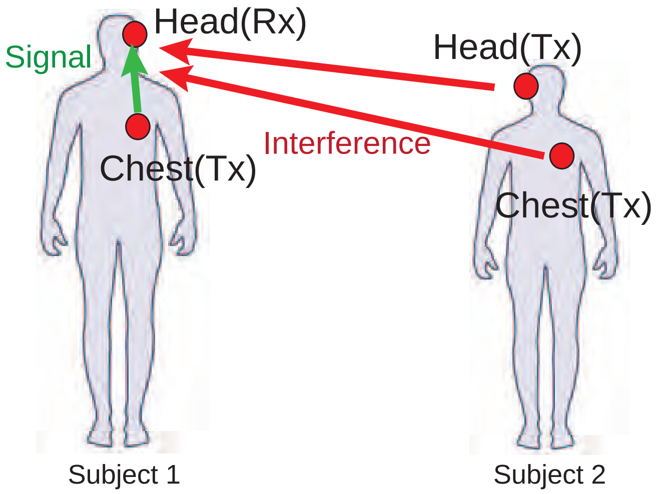

Figure 6.7: Interference equivalent scenario for head-chest channels.

6.3 Results

6.3.1 Interfering signal strength variation

In order to eliminate the effect of noise on the characteristics of the channel samples of interference lower than a certain threshold were excluded from the analysis. The threshold was chosen to be at the level not exceeded by noise 99% of the time. For 60 GHz, the S_{21} threshold was -103 dB. Any sample of interference below this threshold was replaced by the threshold. Because all data at 2.45 GHz are above the noise, this process was not applied at 2.45 GHz. Figure 6.8 shows the normalised magnitude of the measured S_{21} for the abdomen-abdomen interference channel. As shown in the figures, the interference level at 2.45 GHz is higher than that at 60 GHz. The interference level for monopoles at 60 GHz is higher than for horns at 60 GHz. Table 6.1 shows the statistics of the magnitude of the interfering signal. The median interference magnitude of 60 GHz monopoles for the abdomen-abdomen interference channel is 17.5 dB lower than that of 2.45 GHz monopoles. The median interfering magnitude of 60 GHz horns is about

26 dB lower than that of 60 GHz monopoles. These findings agree with our assumption that the adoption of 60 GHz radio and directional antennas can reduce the interference level significantly. In addition, the short-term fading at 60 GHz is much more faster than that at 2.45 GHz. The short-term fading is due to the channel dynamics produced by the multipath effect in transmission. As body movements were at almost the same speed while the wavelength at 60 GHz is much shorter, the multipath effect resulted in much larger variation of signal in the small time interval. Also, the standard deviation of interfering magnitude indicates that there are larger interfering magnitude variations at 60 GHz due to 60 GHz propagation characteristics and the narrower beamwidth of directional antennas.

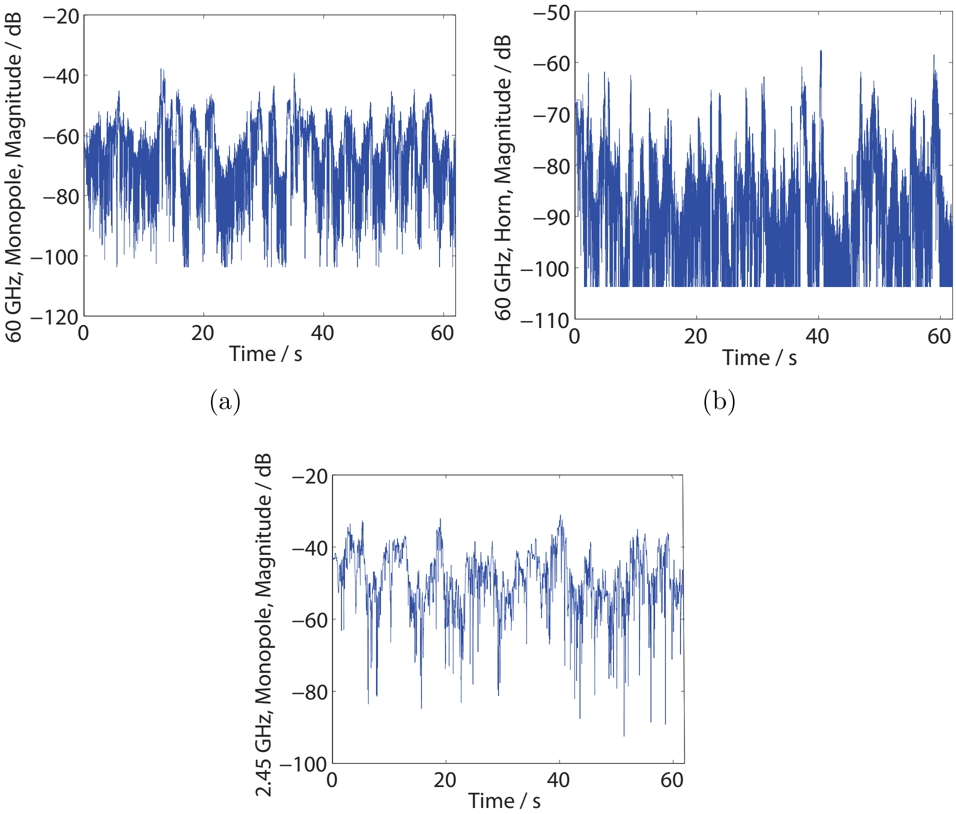

(a) (b)

(c)

Figure 6.8: Normalised magnitude of S_{21} for abdomen-abdomen interference channel: (a) 60 GHz monopole, (b) 60 GHz horn, (c) 2.45 GHz monopole.

Table 6.1: Data statistics for interfering magnitude

Interference channels	Frequency & Antennas	Median(dB)	Standard deviation(dB)
Abdomen-Abdomen	2.45 GHz mono	−48.3	7.7
	60 GHz mono	−65.7	10.2
	60 GHz horn	−89.4	9.9
Abdomen-Head	2.45 GHz mono	−50.1	7.3
	60 GHz mono	−69.6	9.1
	60 GHz horn	−89.4	9.4
Head-Head	2.45 GHz mono	−47.3	6.8
	60 GHz mono	−67.4	9.4
	60 GHz horn	−86.7	9.0
Wrist-Abdomen	2.45 GHz mono	−49.3	7.7
	60 GHz mono	−69.4	9.6
	60 GHz horn	−87.9	8.9
Wrist-Head	2.45 GHz mono	−48.6	7.4
	60 GHz mono	−67.3	8.9
	60 GHz horn	−87.9	7.6
Wrist-Wrist	2.45 GHz mono	−48.3	7.4
	60 GHz mono	−68.5	8.9
	60 GHz horn	−86.9	8.8

Figure 6.9 shows the cumulative distribution function for the interference magnitude of all measured channels. These show similar distributions. According to these measurements, there are two factors that contribute to the interfering magnitude mitigation, namely the frequency and the antenna type. The median values from Table 6.1 were used to calculate how many dB of interference reduction can be achieved corresponding to each factor. As shown in Table 6.2, the differences of the interference magnitude mitigation due to the frequency factor and the antenna factor are less than 2 dB for most interference channels, except for the abdomen-abdomen interference channel. For this channel, horn antennas

achieved 6.3 dB higher interference reduction compared to the reduction achieved by the adoption of 60 GHz radio. This is because of the antenna placement and orientation. The horn antennas placed on the abdomen were facing upwards, as shown in Figure 6.4(c). Also, the abdomen is a less mobile part of the human body. These imply that there is less chance in establishing a direct interference link between two horn antennas placed on two different persons.

Table 6.2: Frequency and antenna contribution to interference magnitude reduction for all measured interference channels

Interference channels	60 GHz vs. 2.45 GHz (dB)	Horns vs. monopoles (dB)
Abdomen-Abdomen	17.4	23.7
Abdomen-Head	19.5	19.7
Head-Head	20.1	19.2
Wrist-Abdomen	20.1	18.4
Wrist-Head	18.6	20.6
Wrist-Wrist	20.1	18.4

The level-crossing rate (LCR) was also calculated for the interference magnitude for all measured channels and is shown in Figure 6.10. The LCR is much higher at 60 GHz compared to 2.45 GHz, because the wavelength is much smaller and they have different multipath effect. By comparing the LCR for 60 GHz monopoles and the LCR for 60 GHz horns, it shows that the radiation pattern of antenna has the significant impact on the LCR. The interference channel with the wrist node exhibits much larger LCRs. This is thought to be a consequence of the highly volatile nature of the movements when the antenna is placed on the wrist. The interference channels with the abdomen and head change at a much slower rate.

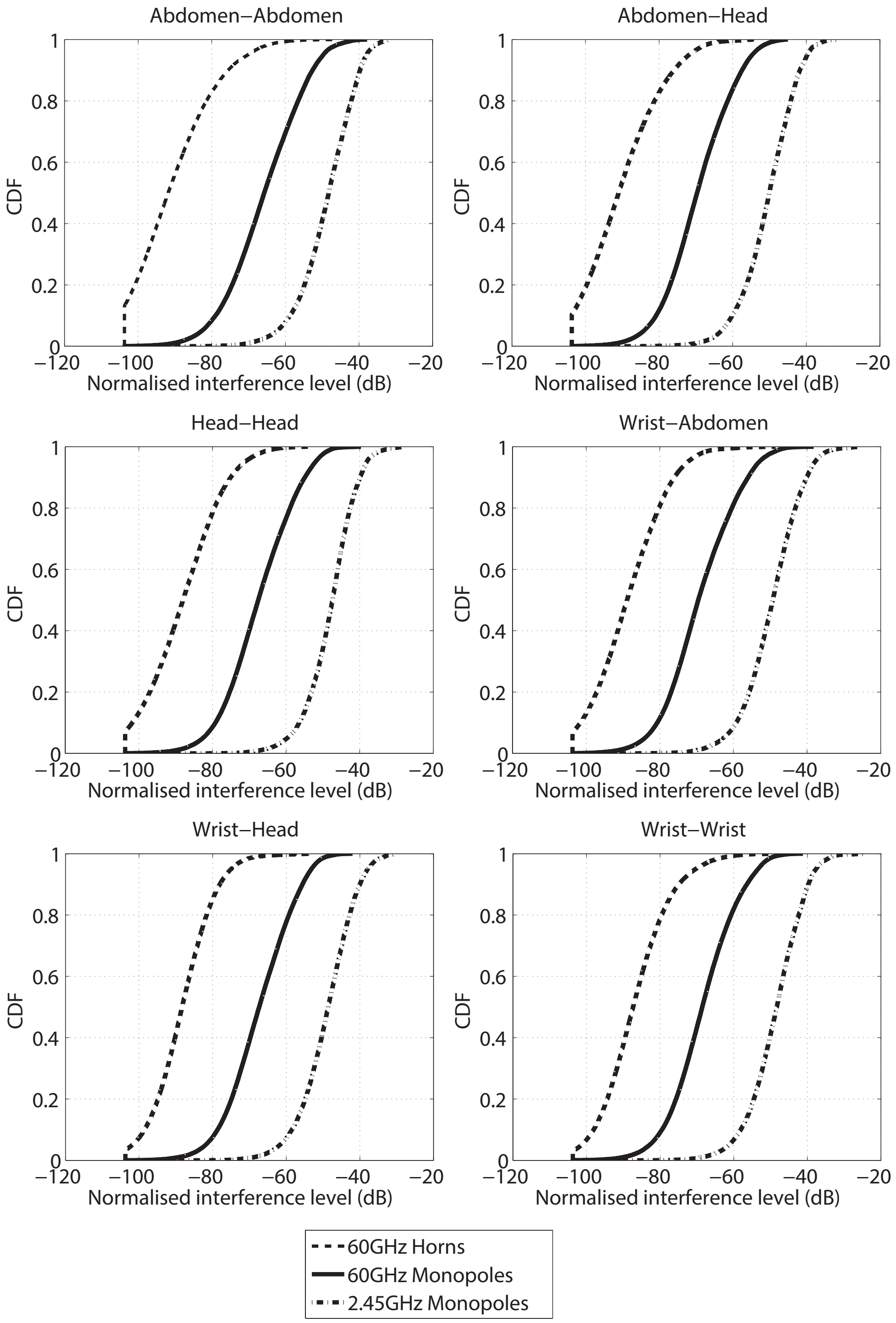

Figure 6.9: CDF for interference magnitude.

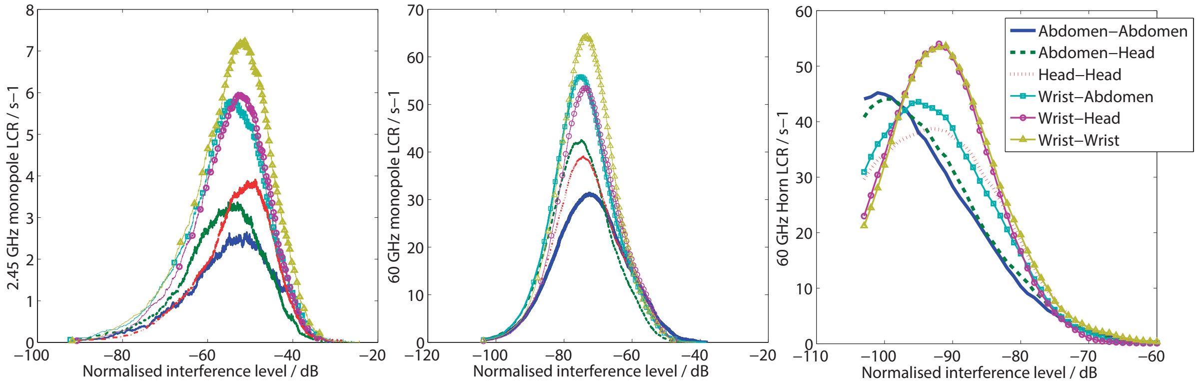

Figure 6.10: LCR for interference magnitude: (a) 2.45 GHz monopoles, (b) 60 GHz monopoles, (c) 60 GHz horns.

6.3.2 Carrier-to-interference ratio (CIR)

Figure 6.11 shows the measured magnitude of $HornH - MonopoleC$ at 60 GHz. In this measurement, one horn antenna and one monopole antenna were placed on the head and the chest for each subject. The (red) solid curve shows the wanted signal from the chest to the head on Subject 1. The (blue) curve with rectangle marker shows the interference from the horn antenna on the chest of Subject 2. The (green) curve with circle marker shows the interference from the monopole antenna on the head of Subject 2. As shown in the figure, the wanted signal is more than 20 dB higher than the interference. For CIR calculation, if either the wanted signal or the interference is below the noise, the data is discarded. Figure 6.12 shows the CIRs against time and the CDF of CIRs for the 60 GHz $HornH - MonopoleC$ measurement. The data statistics of CIRs for other channels are listed in Table 6.3.

Based on the data in Table 6.3, the following comparisons are made: $HornH-MonopoleC$ and $MonopoleC - HornH$ measure the same channel: the head-chest channel. As shown in Figure 6.13, the only difference between two measurements is which antenna was re-

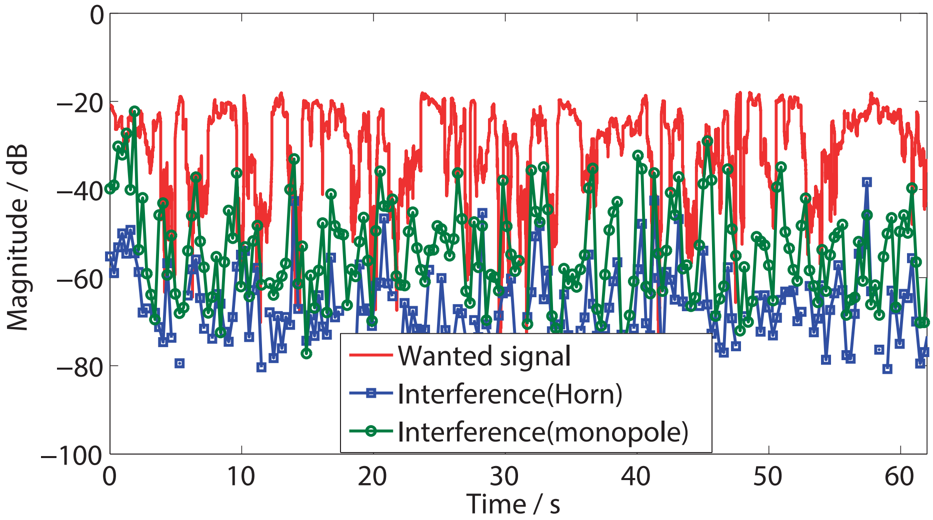

Figure 6.11: Measured magnitude of 60 GHz $HornH - MonopoleC$.

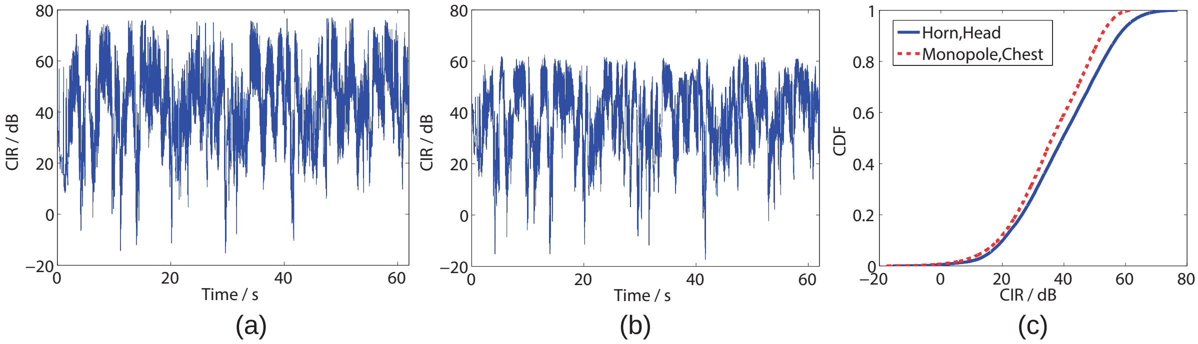

Figure 6.12: 60 GHz CIR of $HornH - MonopoleC$: (a) CIR for interference from horn on the head of Subject 2, (b) CIR for interference from monopole on the chest of Subject 2, (c) CDF of CIRs.

ceiving. For $HornH - MonopoleC$, the receiving antenna was the horn antenna on the head of Subject 1. For $MonopoleC - HornH$, the receiving antenna was the monopole antenna on the chest of Subject 1. $HornH - MonopoleC(HornH)$ gives the highest CIR in this comparison, because both the receiving antenna and interferer are horn antennas. As discussed in Section 6.3.1, the directional antenna mitigates the interfering magnitude significantly. On the contrary, the $MonopoleC - HornH(MonopoleC)$ gives the lowest CIR, because the the receiving antenna and interferer are monopole antennas. The 3.61 dB CIR difference between $HornH - MonopoleC(MonopoleC)$ and $MonopoleC - HornH(HornH)$ must be caused by the unrepeatable random movements which subjects were performing in the measurements. The same finding can be reached in the comparison of $HornH - MonopoleA$ and $MonopoleA - HornH$.

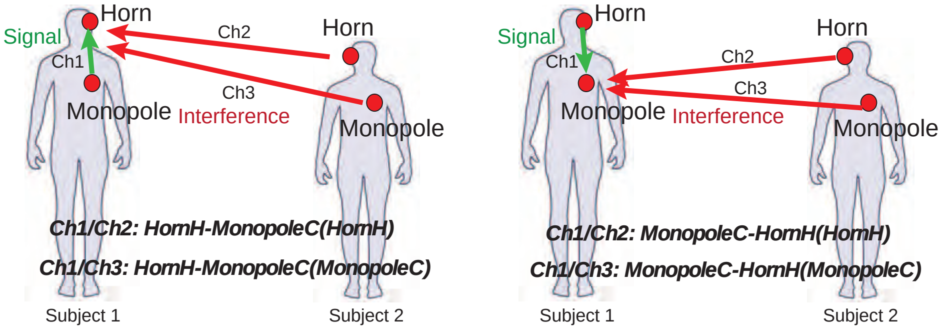

(a) (b)

Figure 6.13: 60 GHz CIR measurement setup for the head-chest channel: (a) $HornH - MonopoleC$, (b) $MonopoleC - HornH$.

Another comparison is made between $HornH - MonopoleC$ and $HornH - MonopoleA$ as shown in Figure 6.14. The difference between the two is the communication distance on Subject 1, which results in more than 20 dB lower CIR for the head-abdomen channel. This is because 60 GHz signal attenuates very quickly when it is propagating along the body, and the short communication distance can improve the wanted signal. Therefore, for single link communications, the shorter communication distance is desired for 60 GHz on-body communications.

Similar CIR measurements at 2.45 GHz were conducted in the same environment and with the same subjects. However, the antennas used at 2.45 GHz were all monopole antennas. The measured CIRs are listed in Table 6.4. The first column indicates which channel we measured and where was the interferer. For example, Abdomen-Head(Head) means that the abdomen-head channel was measured with the monopole antenna on the abdomen

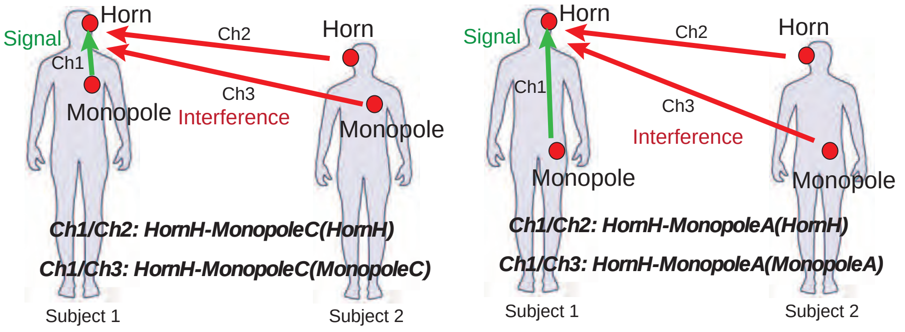

(a) (b)

Figure 6.14: 60 GHz CIR measurement setup for the head-chest and chest-abdomen channels: (a) $HornH - MonopoleC$, (b) $HornH - MonopoleA$.

Table 6.3: Data statistics of CIRs for measured on-body channels at 60 GHz

Carrier-to-interference ratio[1]	Median(dB)	Standard deviation(dB)
$HornH - MonopoleC(HornH)$	39.5	14.4
$HornH - MonopoleC(MonopoleC)$	36.1	13.0
$MonopoleC - HornH(HornH)$	32.5	13.9
$MonopoleC - HornH(MonopoleC)$	28.2	14.3
$HornH - MonopoleA(HornH)$	18.4	14.7
$HornH - MonopoleA(MonopoleA)$	16.2	13.1
$MonopoleA - HornH(HornH)$	15.6	14.2
$MonopoleA - HornH(MonopoleA)$	10.1	13.4

[1] The interferer's antenna type and position are shown in the parentheses.

of Subject 1 receiving. The interferer was from the monopole antenna on the head of Subject 2 as shown in the parentheses.

Figure 6.15 shows the comparison of the CIRs for the abdomen-head channel at 60 GHz and 2.45 GHz. The receiving antenna was the monopole antenna on the abdomen of Subject 1. From the data statistics tables, up to 15 dB (median value) CIR improvement can be observed at 60 GHz if the receiving antenna is a monopole. If the receiving antenna is a horn, up to 18 dB (median value) CIR improvement can be achieved. Figure 6.16

Table 6.4: Data statistics of CIRs for measured on-body channels at 2.45 GHz

Carrier-to-interference ratio	Median(dB)	Standard deviation(dB)
Abdomen-Head(Head)	2.0	10.5
Abdomen-Head(Abdomen)	−0.2	10.4
Chest-Head(Head)	8.6	9.0
Chest-Head(Chest)	8.7	9.7

shows the comparison of the CIRs for the chest-head channel at 60 GHz and 2.45 GHz. The receiving antenna was the monopole antenna on the chest of Subject 1. Much larger CIR improvements can be achieved. Up to 24 dB (median value) and 30 dB (median value) CIR improvement can be observed for the monopole and horn antennas, respectively.

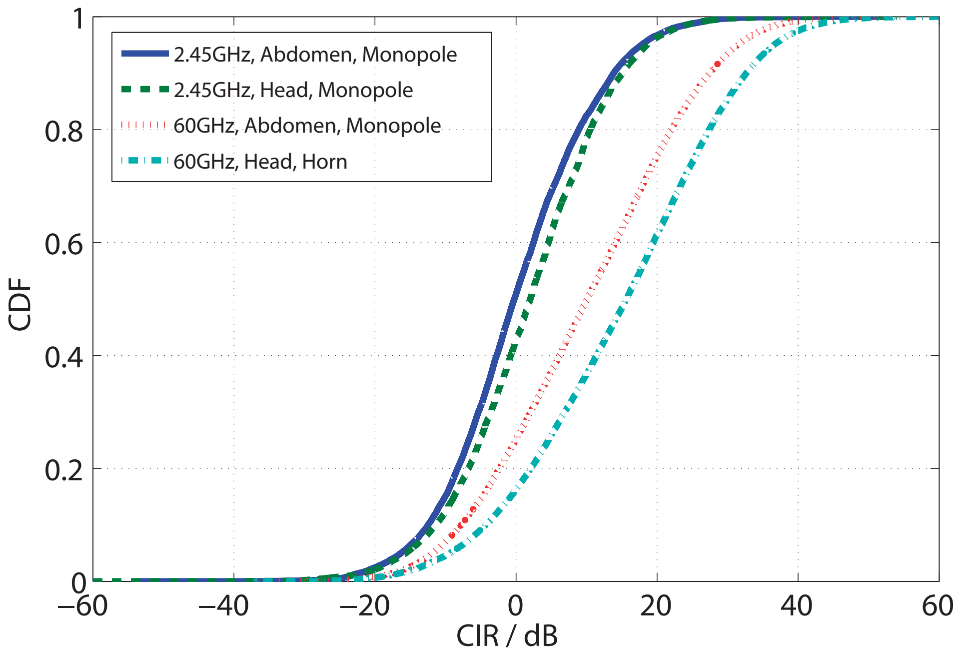

Figure 6.15: CIR comparison for abdomen-head channel at 60 GHz and 2.45 GHz.

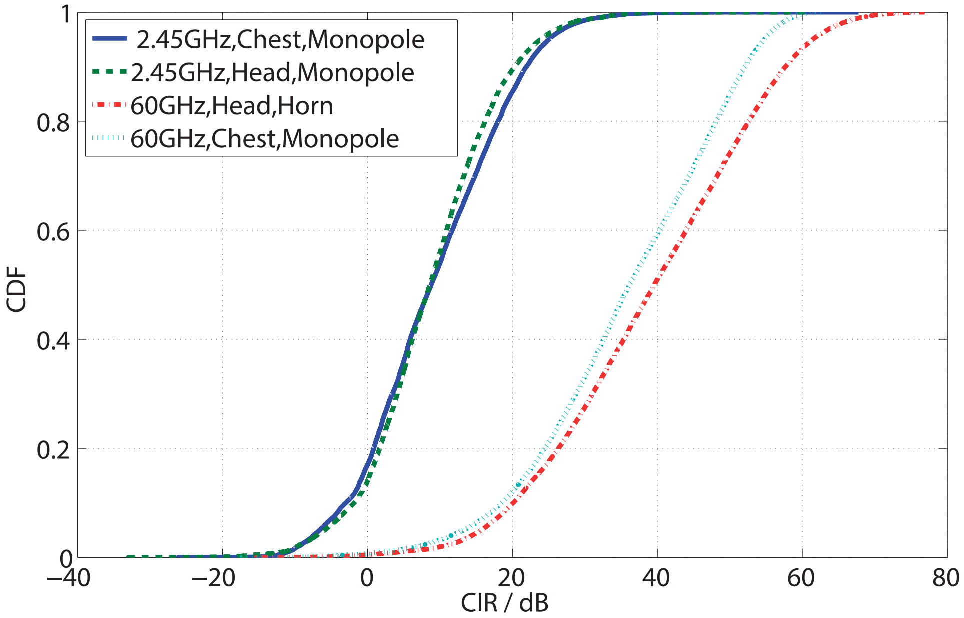

Figure 6.16: CIR comparison for chest-head channel at 60 GHz and 2.45 GHz.

6.4 Summary

In this chapter, the co-channel interference for wireless body area networks at 60 GHz and 2.45 GHz were investigated. Two sets of measurements were conducted: the interference magnitude and the carrier-to-interference ratio. Both measurements were conducted in a lab environment with two subject. Continuous body movements were considered in these measurements. Based on the results presented in the previous sections, adoption of 60 GHz radio and directional antennas can reduce the observed levels of interference significantly. The highly volatile nature of the movements when the antenna is on the wrist results in higher chance of the interference. The CIR can be significantly improved for the short-distance communications, especially at 60 GHz, because the adoption of the directional antenna not only improves the wanted signal, but also reduces the interference level. To further reduce the interference, reconfigurable antennas can be used, which will be described in Chapter 9. They can generate nulls in the direction of the interferer, but in order to realise this function, the direction of arrival of the interference and wanted signal is required. Receivers with interference rejection function would be very complex, and it will add up to the cost and size of the receivers.

CHAPTER 7

INVESTIGATION OF COVERTNESS OF WIRELESS BODY AREA NETWORKS AT 60 GHZ

7.1 Introduction

In addition to healthcare, defence is another significant potential application for wireless body area networks. Defence programs, such as the Future Integrated Soldier Technology in the UK and Land Warrior and Future Force Warrior in the USA, aim to create fully integrated combat systems by incorporating varieties of wearable devices and sensors on dismounted soldiers. These systems can achieve information superiority for soldiers by providing advanced visual, voice and data communications. For example, high definition video from other squad members' sighting system can be displayed on the soldier's helmet mounted visors in real-time through body-to-body communications, and also the physiological inertial sensors on the soldiers can continuously monitor parameters of a soldier such as their heart rate, body temperature and body motions and relay these data to the nearest control and command centre.

However, the integration of wireless body-worn devices into the soldier combat system will encounter lots of challenges. For military applications the devices are expected to be operated in much more diverse and harsh conditions than those in civilian ones, and also need to achieve very high levels of performance in quality, accuracy and reliability. Wireless security is critical to achieve this high level of performance. For example, tactical information must be distributed effectively among dismounted soldiers in the battle field while maintaining a low probability of interception and detection. In order to achieve this, the communications on a soldier, from soldier to soldier or from soldier to a command centre must be covert. Covertness here is defined as a radio system that has a low probability of detection and thus signal transmissions remain concealed from potential enemies.

Normally, military research is classified, but some publications about 60 GHz BANs for military applications can be found in the open literature: soldier-to-soldier communications and the channel propagation characteristics on the soldier at 60 GHz were studied in [186, 187], respectively, but these publications are all based on simulation or the measurements with static postures.

This chapter focuses on the investigation of covertness for wireless body area networks at the physical layer, especially to demonstrate the improvement of covertness of communications by adopting 60 GHz radio compared to lower frequencies. A model is proposed to predict the maximum detection distance at a certain probability of detection and the measurements were conducted with monopole and horn antennas placed on the human body. Body movements have also taken into account in this model.

7.2 Overview of Detection Fundamentals

Radar detection theory has been widely studied [188–190] and its subject is to determine whether a given measured signal is the result of an echo from a target, or caused by noise or interference. In theory, this decision is a problem in statistical hypothesis testing and this theory can be applied to the study described in this chapter.

For any detection measurement which is to test the presence of a target, one of two following hypotheses can be true:

1. H_0: The measurement is only the result of noise or interference arising due to the presence of clutter, hence, a target is not present
2. H_1: The measurement is result of both echoes from a target and noise, hence, a target is present

The detection process is to test and select which hypothesis is best at accounting for the measurement. Since signals are described statistically, statistical decision theory is applied in this decision process. Firstly, two probability density functions (pdfs) are established to describe the measurement to be tested under each hypothesis. After two pdfs are successfully modeled, three probabilities of interest are defined:

- Probability of Detection, P_D, when a target is declared (H_1 is chosen), and a target is in fact present
- Probability of False Alarm, P_{FA}, when a target is declared (H_1 is chosen) but a target is in fact not present

- Probability of Miss, P_M, when a target is not declared (H_0 is chosen) but a target is in fact present

Because $P_M = 1 - P_D$, P_D and P_{FA} are sufficient to specify all probabilities of interest. The relationship between P_D and P_{FA} for Gaussian pdfs can be derived as follows [191],

$$P_D = \frac{1}{2}\operatorname{erfc}\left\{\operatorname{erfc}^{-1}(2P_{FA}) - \sqrt{\chi/2}\right\} \tag{7.2.1}$$

where $\operatorname{erfc}(\cdot)$ is the complementary error function and χ is SNR in linear ratio unit. A receiver operating characteristic (ROC) curve can be constructed based on a similar equation to Equation (7.2.1). Figure 7.1 shows a typical ROC curve. As shown in the figure, P_D increases as the SNR increases, but P_{FA} increases as well. Hence a tradeoff between P_D and P_{FA} has to be made by increasing the SNR for a detector design. The values of P_D and P_{FA} depend on various conditions, such as target type, detection range, interference environment, etc. The detector designer also has to take antenna design, waveform design, transmitter power and signal processing techniques into account. Normally, P_{FA} is lower than 10^{-3} and very often is in the range of 10^{-6} to 10^{-8}.

7.3 Probability of Detection Estimation Model

In military telecommunications, there exists a term named Electronic Support Measures in electronic warfare. It implies to detect, intercept, identify, locate, record, and analyse sources of radiated electromagnetic energy for the purposes of immediate threat recognition or long-term operational planning [193]. A soldier wearing wireless devices must avoid being detected and intercepted. Based on this concept, a model is build to estimate the probability of detection. The scenario we consider is as follows: a soldier is wearing

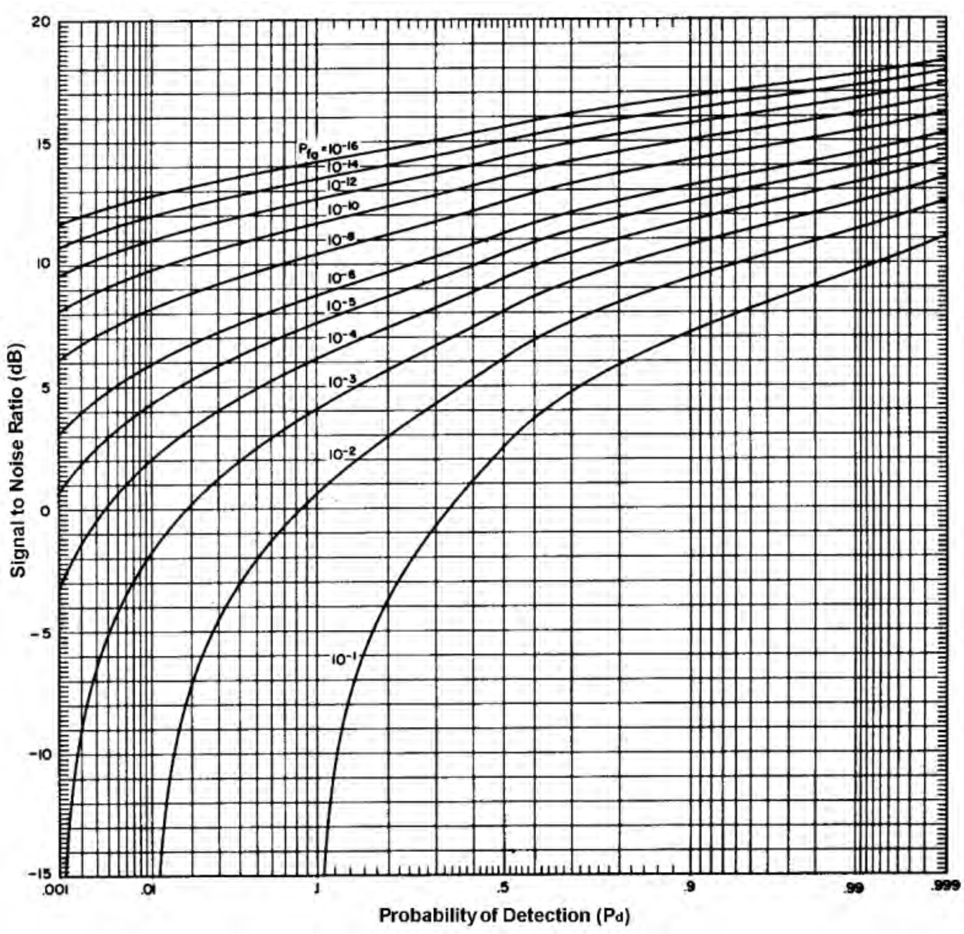

Figure 7.1: Detection probability as a function of signal to noise ratio with false alarm probability as a parameter. Copyright of Artech House, reproduced from [192].

a body area network in a battlefield environment. The environment in the immediate vicinity surrounding the soldier gives rise to multipath scattering, which is then detected by a potentially hostile remote observer equipped with a directional antenna and sensitive receiver at a long distance away. The remote observer is passively listening to electromagnetic radiations of military interest. This scenario is approximated by the laboratory experiment described shortly. A channel decomposition method was adopted to establish the detection model [194]. The novelty of this method amounts to separating a body channel within its surrounding environment and a free-space, or two-ray ground reflection propagation channel as sketched in Figure 7.2.

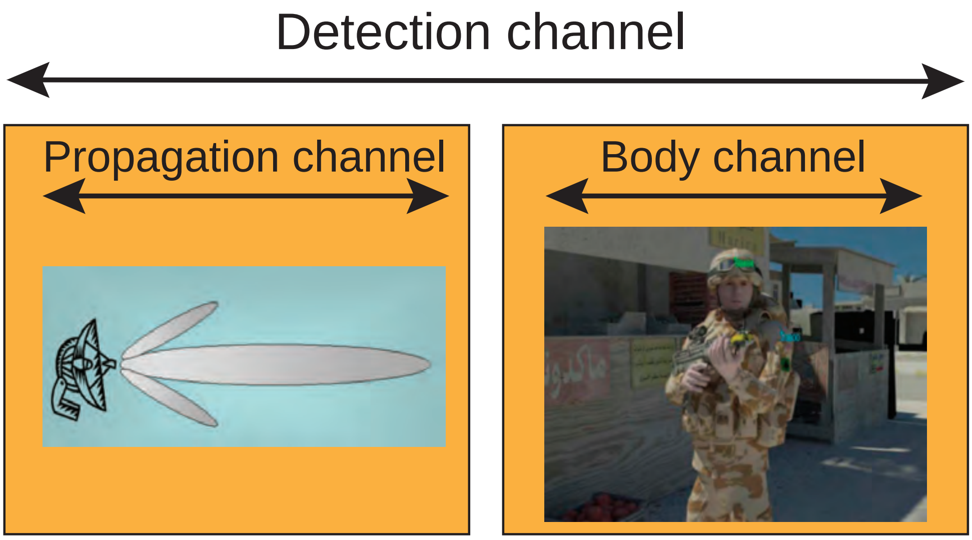

Figure 7.2: Channel decomposition for detection channel.

In this model, the received power at the remote detector is given by:

$$W_R = W_T \cdot G_{OB} \cdot G_D \cdot F(d) \cdot X_s \tag{7.3.1}$$

$$F(d) = \begin{cases} \left(\dfrac{\lambda}{4\pi d}\right)^2 \cdot e^{-2\alpha d} & d < d_C \quad (7.3.2a) \\ \left(\dfrac{h_T \cdot h_D}{d^2}\right)^2 \cdot e^{-2\alpha d} & d > d_C \quad (7.3.2b) \end{cases}$$

$$d_C = \frac{4 h_T h_D}{\lambda} \tag{7.3.3}$$

where W_R and W_T are the received power at the detector and transmitted power from the soldier , respectively. F is the free-space or two-ray ground model path gain (atmospheric attenuation $\alpha = 1.842 \times 10^{-3}$ Np/m is included at 60 GHz), depending on whether the distance between the target and detector, d, is smaller or larger than the cross-over distance d_C and h_T and h_D are antenna heights of the target and detector, respectively. λ is wavelength. X_s is the random excess path gain caused by the combined body shadowing and local scattering. G_{OB} and G_D are the on-body and detector antenna gains, respectively. In this model, we define a single random variable,

$$X = G_{OB} \cdot X_s \tag{7.3.4}$$

because the receiving antenna is embedded in the body channel and dembedding of the on-body antenna from the body channel is a big challenge. X is related to the body channel as shown in Figure 7.2, which include self-shadowing from the soldier's body and local scattering in the vicinity of the soldier. It will be characterised in the measurements described in the following section.

Therefore, given a detection system received power threshold W_{Th}, the probability of observability ($P_{(detect|pointing)}$) is given by:

$$\begin{aligned} P_{(detect|pointing)}(W_R > W_{Th}) &= P_{(detect|pointing)}\Big(X > \frac{W_{Th}}{W_T \cdot G_D \cdot F(d)}\Big) \\ &= 1 - CDF\Big(\frac{W_{Th}}{W_T \cdot G_D \cdot F(d)}\Big) \end{aligned} \tag{7.3.5}$$

In this model, it is assumed that the target and the detector are in line of sight. However, in a real situation, the angle of a target relative to detector is unknown, so the main beam of radiation pattern of the high gain detector antenna should be scanned, either mechanically or electrically, to capture the target. Hence, there will be another probability describing whether the detection antenna main beam is pointed towards the BAN scattering area. As shown in Equation (7.3.6), the probability of detection then is the product of this (pointing) probability ($P_{pointing}$) and the observability probability ($P_{(detect|pointing)}$) defined by Equation (7.3.5). The higher the gain of the receiving antenna, the higher the observability probability, but the lower the pointing probability which is dependent on the receiving antenna beamwidth as well as the detection range. Note that $P_{(detect|pointing)}$ is a conditional probability which is the probability of the soldier being detected only when the soldier has been pointed by the detection antenna.

$$P_D = P_{(detect|pointing)} \cdot P_{pointing} \tag{7.3.6}$$

7.4 Body Channel Measurements

This measurement is to characterise the parameter, X defined in the model. In order to create a similar scenario to a soldier in the battle field, the measurements were conducted on the roof of Gisbert Kapp Building at the University of Birmingham. As shown in Figure 7.3, the roof is a relatively open space, but it has walls and obstacles which provide multipath scattering. The detection antenna (horn antenna with vertical polarisation) was placed on a tripod with height of 1.56 m. A subject with height of 1.70 m wearing an antenna on the body was performing random movements at 4 m away from the detection antenna. Both antennas were connected to direct access ports of the VNA through cables. The antenna on the body was transmitting while the detection antenna on the tripod was receiving. The received signal was monitored during the measurements. Movements were done carefully with the subject walking in a small area about 1×1 m^2. The antenna was placed on three parts of the body, namely head, waist, and wrist. The measurements for every position repeated two times. All cables were taped to the floor except the one connected to the antenna on the subject in order to minimise the signal variation caused by cable movements. It is worth mentioning that this experiment was a simplified situation compared to the real scenario in the battlefield, where the local scattering from the environment could be more complex. Also, a single beam antenna was used as detection, but in a real situation, a multi-beam array could be used. In addition, the detection antenna height is 1.56 m, but in real situation it would be probably higher, so that it may give rise to some errors in characterising X. Finally, a dual polarised detection antenna can be used in a real situation.

(a) (b)

Figure 7.3: Measurements setup on the roof.

These measurements were conducted at both 60 GHz and 2.45 GHz. For 60 GHz, a Flann© 20 dBi standard gain horn (Series 240 model 25240) was placed on the tripod as the detection antenna, and a monopole antenna and the same horn antenna was placed on the body of the subject in separate instances. In order to improve the dynamic range at 60 GHz, two amplifiers were used during the measurements, namely, a power amplifier (Spacek Labs Inc. SP604-13-12W) and a low noise amplifier (Spacek Labs Inc. SL6010-15-6). In order to calibrate out the amplifiers, a free-space calibration was performed. Two horn antennas were placed on the tripods at 4 m apart. They were both vertically polarised and carefully aligned, with the amplifiers switched on. The VNA was set to 60 GHz CW with 60001 sweep points taken over a sweep time of 62.1 s. The output power and measurement bandwidth were set to 0 dBm and 1 kHz respectively. For 2.45 GHz, the detection antenna was a Q-par© horn antenna (Model Number WBH1-18S) with 7 dBi gain at 2.45 GHz. It was placed on the tripod with vertical polarisation. The antenna placed on the subject was a quarter-wavelength monopole antenna at 2.45 GHz. No amplifier was used at 2.45 GHz, so a through calibration with cables was performed before the measurements. The VNA settings were the same as those at 60 GHz except for the measurement frequency. Figures 7.4, 7.5 and 7.6 show the placements of 2.45 GHz monopole, 60 GHz monopole, and 60 GHz horn on the body, respectively. As shown in the figures, all antennas were placed on the right side of the body. For the horn antenna, it was pointing downwards when it was placed on the head and pointing upwards when it was placed on the waist and wrist.


(a) (b) (c)

Figure 7.4: Placements of monopole antenna on the body (2.45 GHz): (a) Head, (b) Waist, (c) Wrist.


(a) (b) (c)

Figure 7.5: Placements of monopole antenna with the amplifier on the body (60 GHz): (a) Head, (b) Waist, (c) Wrist.

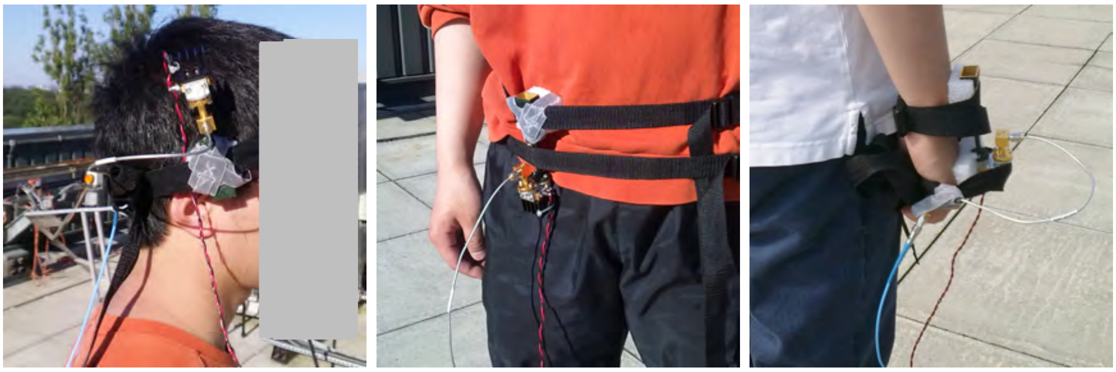

(a) (b) (c)

Figure 7.6: Placements of horn antenna with the amplifier on the body (60 GHz): (a) Head, (b) Waist, (c) Wrist.

7.5 Results and Discussions

The measured data were re-normalised to remove the detector antenna gains, free space path loss at a 4 m distance and amplifier gains at 60 GHz in order to characterise X. The RMS noise floor is -56.5 dB after re-normalisation. The CDFs of the measured received signal magnitude X are shown in Figure 7.7. As shown in the figures, the maximum values of X are larger than 0 dB which is caused by the on-body antenna gain on the soldier. In the wrist channel, due to movement of the wrist, there may be some chances that the on-body horn antenna and detector antenna have a line-of-sight link, which gives an X higher than 10 dB. In the remaining channels, horn antennas on the soldier were placed pointing downwards and they did not involve large movements, giving a lower observed value of X.

The detection receiver specifications are needed to determine the detection system received power threshold W_{Th}. Equation (7.5.1) [195, p. 85] was used to calculate the noise level

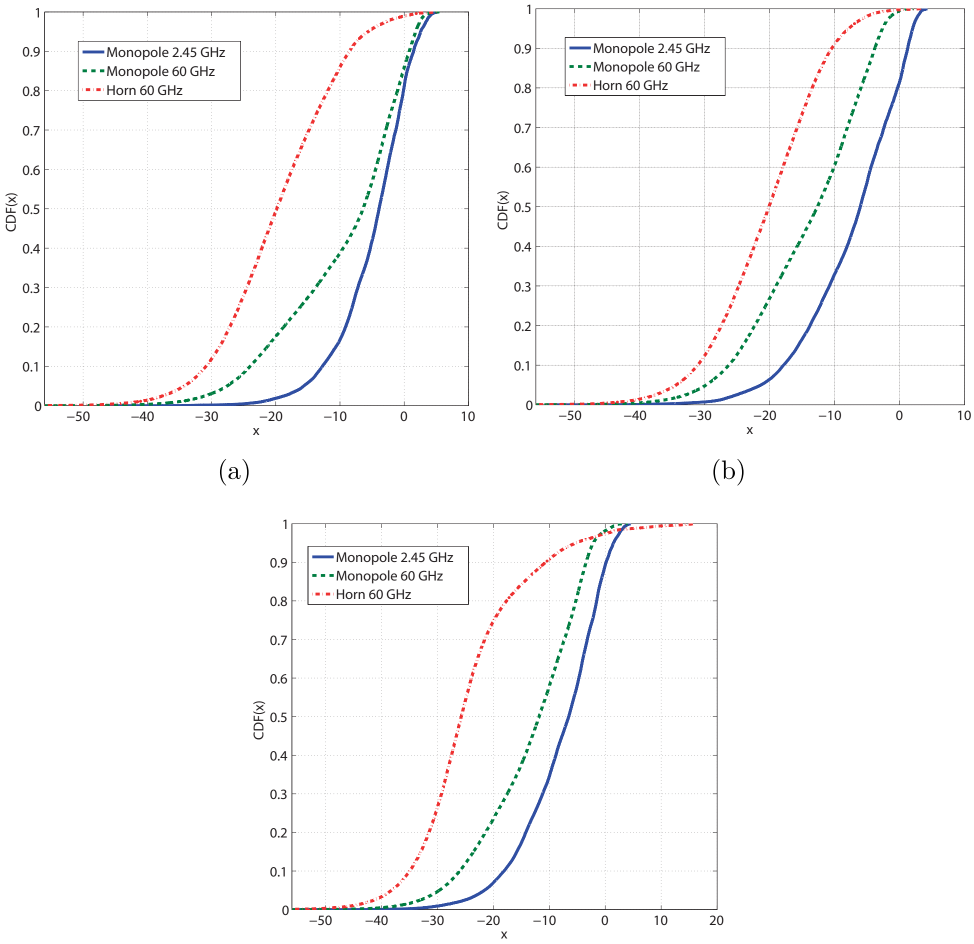

(a)

(b)

(c)

Figure 7.7: CDF of X: (a) Head channel, (b) Waist channel, (c) Wrist channel.

of the receiver.

$$L_N = -174\text{dBm} + NF + 10\log_{10}(S_F)\text{dB} + 10\log_{10}\left(\frac{B_{IF}}{\text{Hz}}\right)\text{dB} \tag{7.5.1}$$

where L_N is the noise level, -174 dBm corresponds to the thermal noise, NF is the noise figure of the receiver. B_{IF} is IF bandwidth. Because the IF filter does not have a rectangular transmission characteristic, the noise bandwidth of the IF filter is always somewhat greater than the 3 dB bandwidth which is used to characterise the filter setting. The shape factor, S_F is the ratio of these two bandwidths. A 60 GHz VμbIQ RX module and a Texas Instruments CC2420 were used for detector receiver specifications in this estimation. Based on the specifications of the 60 GHz VμbIQ RX module, the noise figure and IF bandwidth are 6 dB and 200 MHz, respectively. We assume $S_F = 1$, hence, receiver sensitivity of VμbIQ RX module is -85 dBm. According to the specifications of CC2420, its receiver sensitivity is -92 dBm. Also, the following assumptions are made: the transmitting power from the antenna on the body was 0 dBm and the detection antenna gain was 20 dBi.

Based on Figure 7.1, SNR=3 dB, $P_D = 6\%$, $P_{FA} = 10^{-3}$ were selected for analysis as an extreme detection case, hence W_{Th} for the 60 GHz VμbIQ RX module and the 2.45 GHz CC2420 are -82 dBm and -89 dBm, respectively.

Equation (7.3.5) can be rearranged to the following equation:

$$F(d) = \frac{W_{Th}}{W_T \cdot G_D \cdot X|_{CDF(X)=1-P_{(detect|pointing)}(W_R>W_{Th})}} \tag{7.5.2}$$

$$P_{(detect|pointing)} = \frac{P_D}{P_{pointing}} \tag{7.5.3}$$

We assume $P_{pointing} = 50\%$, the antenna height of detector $h_D = 5$ m and the antenna height of target $h_T = 1.5$ m. $X|_{CDF(X)=1-P_{(detect|pointing)}(W_R>W_{Th})}$ is the value of X corresponding to a certain probability from the CDF of X. By combining Equations (7.3.2), (7.5.2) and (7.5.3) and data from Figure 7.7, we can calculate the detection distance corresponding to a certain detection probability. Table 7.1 shows calculated data for detection at 2.45 GHz and 60 GHz based on the assumptions made. Note that at 2.45 GHz, two-ray ground reflection model was used to calculate detection distance because the cross-over distance at this frequency is 245 m.

Table 7.1: Maximum detection distance estimates:
SNR $= 3dB, P_{FA} = 10^{-3}, P_D = 6\%, P_{pointing} = 50\%, P_{(detect|pointing)} = 12\%$

Frequency&Antenna	Position	X (dB)	F (dB)	d (m)
2.45 GHz Monopole	Waist	0.93	-109.93	1534
	Head	1.02	-110.02	1540
	Wrist	-0.23	-108.77	1435
60 GHz Monopole	Waist	-4.22	-97.78	29
	Head	0.39	-102.39	48
	Wrist	-3.80	-98.20	31
60 GHz Horn	Waist	-11.16	-90.84	14
	Head	-9.32	-92.68	17
	Wrist	-12.22	-89.78	12

As shown in the table, the maximum detection distances for three positions at 2.45 GHz are 1534 m, 1540 m and 1435 m, respectively. Whereas, at 60 GHz, the maximum detection distances are all shorter than 50 m, no matter whether using a monopole or horn antenna on the soldier. At these distances, the presence of the soldier can be detected by human eye sight alone.

The maximum detection distances with some other P_D for the scenario with the antenna on the waist of the body were also calculated. Except P_D and its corresponding SNR, other parameters were kept the same with the previous calculation. Table 7.2 lists the calculated maximum detection distances for the waist channel with different P_D. Results show the distances decrease when P_D increases. Note that based on this model and assumptions, the maximum detection distances when $P_D \geq 50\%$ cannot be calculated because $P_{(detect|pointing)}$ will be greater than 100%.

Another scenario using a 43 dBi parabolic dish (30 cm diameter) detection antenna at 60 GHz was calculated. Other parameters remained unchanged. The maximum detection

Table 7.2: Maximum detection distance (m) estimates for the waist channel: different P_D

P_D,SNR,P_{FA}	2.45GHz Mono	60GHz Mono	60GHz Horn
$P_D = 10\%$,SNR=4.0dB,$P_{FA} = 10^{-3}$	1347	21	9
$P_D = 20\%$,SNR=5.8dB,$P_{FA} = 10^{-3}$	960	11	4
$P_D = 30\%$,SNR=6.6dB,$P_{FA} = 10^{-3}$	742	5	3
$P_D = 40\%$,SNR=7.5dB,$P_{FA} = 10^{-3}$	507	2	1

distances with a body mounted monopole antenna on the three positions at 60 GHz increased to 267 m, 373 m and 275 m, respectively. These distances are still significantly lower than those at 2.45 GHz. In addition, increasing the antenna gain will decrease the beamwidth of the radiation pattern. Based on Equation (7.5.4) [196], the beamwidth of the radiation pattern of the antenna can be estimated.

$$D \simeq \frac{4\pi(180/\pi)^2}{\Theta^2} \tag{7.5.4}$$

where D is directivity of the antenna, Θ is half-power beamwidth in one plane. We assume the half-power beamwidths in both planes are the same. Hence, the half-power beamwidth for 20 dBi gain antenna is approximately 20° and the half-power beamwidth for 43 dBi gain antenna is approximately 1.2°. Narrowing the beamwidth results in the reduction of $P_{pointing}$. Therefore, $P_{pointing}$ for 43 dBi detection antenna is only 3% (we assume $P_{pointing}$ for 20 dBi detection antenna is 50%), and the probability of detection (P_D) decreased significantly.

If the transmitting power from the soldier increases to 10 dBm while the detector antenna gain remains 20 dBi for both frequencies, the maximum detection distance with a 6% detection probability for 2.45 GHz waist position extends to 2728 m, whereas for 60 GHz it becomes 84 m.

7.6 Summary

In this chapter, a new measure of covertness, the probability of detection was introduced. Using a channel decomposition method, a method of estimating the maximum detection distance at a certain probability for detecting a WBAN wearing soldier in a battlefield was proposed. Measurements at 2.45 GHz and 60 GHz was conducted to characterise the body channels in a local area. The maximum detection distances were calculated and compared for different conditions. Studies show at 0 dBm BAN transmitting power the soldier is not detectable at ranges greater than 50 m, while under the same conditions, the detection range at 2.45 GHz can be up to 1540 m. A 10 dBm BAN transmit power and a highly directional detection antenna were employed and the distances are extended beyond 100 m at 60 GHz, but the detection distance extends beyond 2500 m at 2.45 GHz. This demonstrates that the use of a 60 GHz BAN achieves much better covertness than 2.45 GHz. Also, the use of directional antennas on the soldier improves covertness and the antenna placements on the body has effect on the detectability.

Chapter 8

Fixed-Beam Antennas for 60 GHz Body Area Networks

8.1 Introduction

Although monopole antennas are the best in terms of radiation coverage for on-body channels at 2.45 GHz [47], a major problem is the low gain of such antennas. A shortcoming of using millimeter wave bands is the high propagation loss in free space and especially in shadowed regions. This makes establishing reliable communication links on a human body a challenge, as the links have to be short and unobstructed. High gain antennas are required to focus the signal in a particular propagation direction. As discussed in the previous chapters, the high gain antennas such as the traditional horn antenna, can not only improve link performance, but also reduce the interference and achieve better covertness and the carrier-to-interference ratio. However, the most significant disadvantage of the horn antenna is its bulky size, which makes it very hard to integrate into small form factor body sensors. Hence, low profile high antennas are required for body-worn applications. This chapter proposes two antennas for on-body communication channels at 60 GHz: a printed Yagi-Uda antenna and a substrate integrated waveguide antenna. The first two antennas achieve more than 10 dBi gain, end-fire radiation pattern and wide impedance bandwidth, but with orthogonal polarisations. The third antenna is proposed for an RF front end of relay nodes in body area networking because of its bi-directional radiation characteristics. In order to investigate the antenna performance close to the human body, extensive studies on the impact of a phantom on antenna performance have been conducted. Parameters such as antenna/phantom separation, the type of phantom and the size of phantom have been taken into account. On-body measurements using fixed-beam antennas to investigate the chest-belt link and head-shoulder link are also presented.

All of the simulations presented in this chapter were performed using the transient solver in CST Microwave Studio©.

8.2 On-body Antenna Requirements

Wearable antennas should be low profile, lightweight, and ideally conformal to the body surface. However, due to 60 GHz propagation characteristics, there are some additional requirements: First, because of high path loss at 60 GHz, high antenna gain is needed to offset channel loss. According to path loss calculations, at least 10 dBi gain is required at both the transmitter and the receiver for a line of sight path length of typical human body dimensions. Second, for this kind of scenario, the maximum of the radiation pattern should be tangential to the body surface to maximize the signal transferred between bodyworn devices. Previous studies showed that a monopole antenna gives very good results for on-body applications at lower frequencies [197], but it is difficult to provide the high gain required in the 60 GHz band. Metamaterial structures can be introduced to improve gain [198]. However, in this work, we focus on relatively narrow beam antennas which achieve an end-fire radiation pattern tangential to the body surface. Such high gain antennas can lead to better security, as they minimize the amount of energy radiated away from the body, thus giving good BAN to BAN and BAN to fixed base station isolation. For the aforementioned reasons, Yagi-Uda antennas have been chosen as strong candidates because of their good compromise in terms of size and gain performance compared to other end-fire antennas, such as tapered slot antennas.

8.3 Printed Yagi-Uda Antenna

Variants of the printed Yagi-Uda antenna have been introduced in [199]. Based on these a single printed Yagi-Uda antenna has been designed with a driven dipole, 18 directors and one reflector on both sides of a 0.127 mm thick RT/Duroid 5880 substrate ($\varepsilon_r = 2.2$, measured at 10 GHz [200]). Normally, the gain of a Yagi-Uda antenna is about 10 dBi. To further increase the gain, four identical single printed Yagi-Uda antennas are arranged together in a linear array configuration as shown in Figure 8.1 based on the trade-off between the gain and the design complexity. For each single printed Yagi-Uda antenna, one half of each driven dipole is placed on one side and the other half on the opposite side of the dielectric substrate. Symmetrical parallel lines are used as a feeding structure which printed on both sides of substrate. Due to the 180° phase difference between the upper line and the lower line, the sidelobe level is significantly reduced compared to coplanar strip feeding [201]. The substrate used is very thin so the dipole arms are only slightly out of phase, resulting in an insignificant adverse effect on the radiation pattern. By changing the propagation constant linearly along the length of the antenna, the sidelobe level can be reduced and the gain of the antenna can be improved. It is proved that the linear variation of the propagation constant can be obtained by slowly tapering the

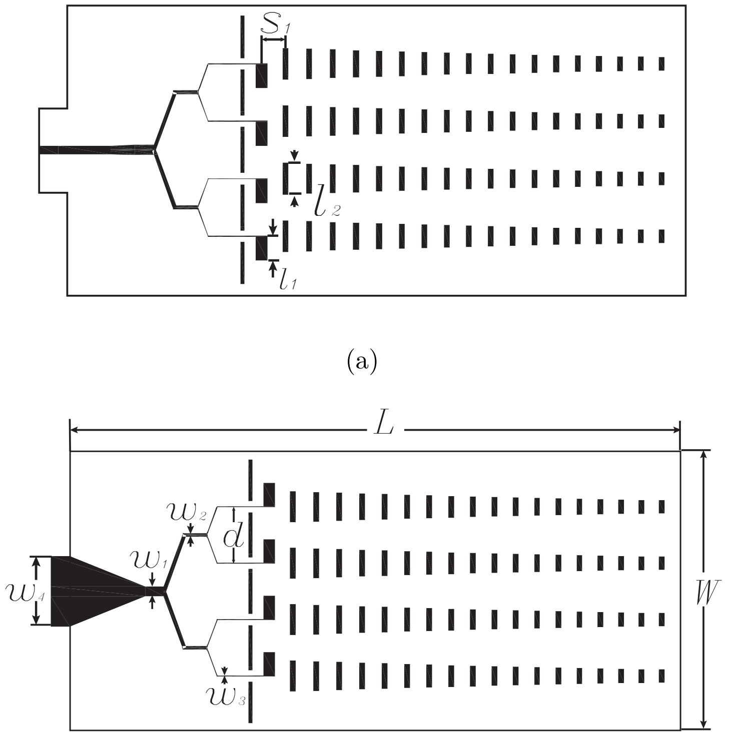

(a)

(b)

Figure 8.1: Layout of the printed Yagi-Uda array:(a) Top view; (b) Bottom view

element lengths and element spacings along the length of the antenna [202]. Based on this study, a number of combinations of tapered factors for both director lengths and spacings were used in the simulations, trying to find better antenna gain and sidelobe level. Finally, the length taper factor of 0.95 and the spacing taper factor of 0.99 were selected. The spacings and lengths of directors are decreased gradually by these factors from 1.25 mm, 1.65 mm, respectively. It is worth mentioning that because this is a trial and error process, it is probably not the optimal configuration. The dimensions of the antenna are given in Table 8.1.

Table 8.1: Dimensions for the antenna shown in Figure 8.1

Parameters	W	L	s_1	l_1	l_2	w_1	w_2	w_3	w_4	d
Dimensions (mm)	15	32.6	1.25	1.298	1.65	0.5068	0.204	0.048	3.7592	3

A four-way power divider is designed to equally distribute power to each single antenna. Simple Y-junctions are used to split power from a one-way to a two-way path. This power divider is also patterned on the both sides of substrate. At the end of the power divider, a parallel line to microstrip line transition is introduced by means of a tapered microstrip line ground plane.

The centre-to-centre spacing, d, is defined between two adjacent two single Yagi-Uda antennas. This is a crucial parameter in the array design. If the spacing is too small, the mutual coupling among antenna elements would increase, which results in degradation of antenna performance. If the spacing is too large, the side lobe level will increase. A number of spacings have been simulated in CST Microwave Studio©, trying to trade off between the array gain and the side-lobe level. The target gain of this process is 15 dBi, and the target sidelobe level is more than 10 dB below the maximum gain. It was found that by arranging the single antennas too close to each other ($d \leqslant 2.5$ mm), the overall array gain decreases because mutual coupling among single antennas becomes too strong. If $d \geqslant 3.5$ mm, side-lobe levels become too high. Consequently, the value $d = 3$ mm was chosen.

For measurement purposes, a ridged intermediate step waveguide to microstrip transition is adopted because of broad bandwidth, better match and wider range of available impedances [203]. The outer dimensions of the transition is $30 \times 15 \times 28$ mm^3. It cannot be made smaller because it needs to be big enough to support the waveguide flange.

As shown in Figure 8.2, two steps are used. Their dimensions are $1 \times 0.4 \times 1.7296$ mm^3, and $1 \times 0.4 \times 1.2496$ mm^3, respectively. The aperture size of waveguide is standard WR15.The final configuration of the conventional Yagi-Uda array is shown in the Figure 8.3.

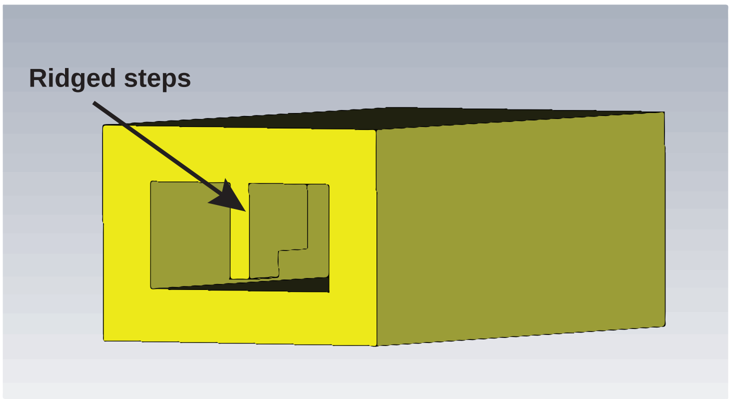

Figure 8.2: Microstrip-to-waveguide transition.

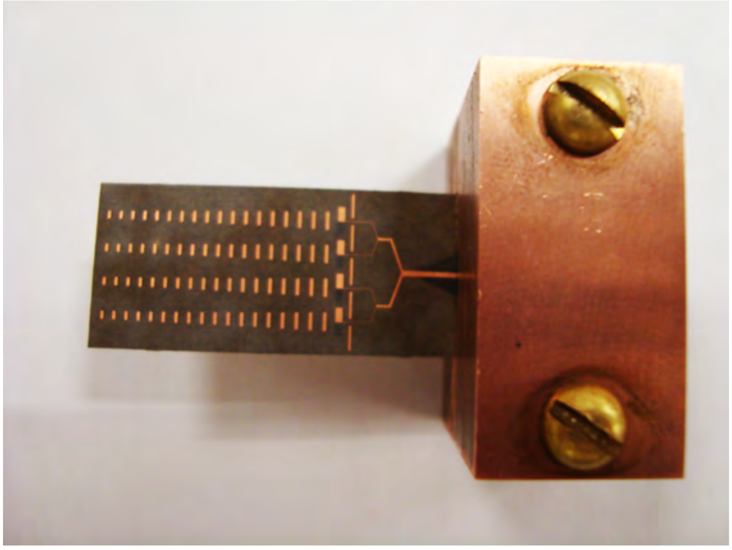

Figure 8.3: Final configuration of the printed Yagi-Uda array.

Figure 8.4 shows the simulated and measured return loss. 5 GHz of −10 dB bandwidth is achieved from 55 GHz to 60 GHz. Although there is a frequency shift, resonances with good impedance matching can be seen.

Figure 8.5 shows the simulated and measured radiation pattern of the printed Yagi-Uda array. The (red) solid line shows simulated pattern. The (blue) dashed line shows the measured co-polarised pattern. The (black) dotted line shows the cross-polarised pattern. The gain measurement was conducted using gain-transfer method by comparing to a standard gain horn antenna. The measured gain is 16.1 dBi. The 3 dB beamwidths in the E and H planes are 19.1° and 29.5°, respectively. The H plane sidelobe level is approximately -18 dB and the E plane sidelobe level is about -16 dB. The cross-polarisation levels are relatively high in both the planes due primarily to the radiation from the open aperture of the waveguide transition block.

8.4 Substrate Integrated Waveguide Yagi-Uda Antenna

Recently, substrate integrated waveguide (SIW) technology has been demonstrated as a promising candidate for millimetre-wave integrated circuits and systems for the next decade. Based on planar dielectric substrates with top and bottom metal layers perforated with metallic vias, SIW structures offer a compact, low loss, flexible, and cost-effective solution for integrating active circuits, passive components and radiating elements on a single substrate [204]. However, there are some extra losses due to the leakage through gaps between vias and dielectric losses in the waveguide. Some design rules for SIW are

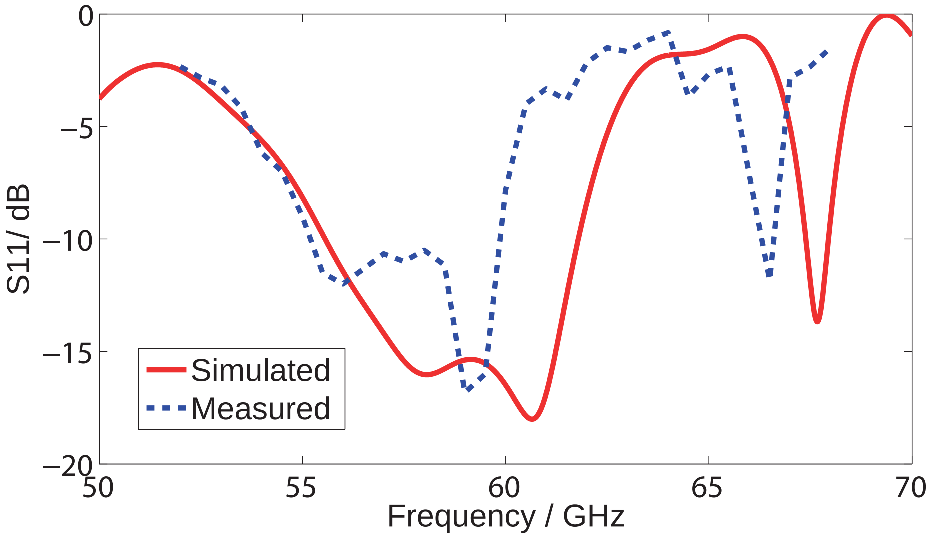

Figure 8.4: Reflection coefficient (S_{11}) of the printed Yagi-Uda array with waveguide feeding.

summarised in Appendix B.

The geometry of the SIW Yagi antenna is shown in Figure 8.6. On the left side of the antenna is a planar waveguide structure, where two periodic rows of metallic vias are employed to form the sidewalls of the waveguide. The substrate used here is RT/Duroid 5880 substrate ($\varepsilon_r = 2.2$, measured at 10 GHz [200]), with thickness of 0.787 mm. The width of the SIW, w is 2.6 mm. The diameter and the center-to-center spacing of the waveguide vias, q, are 0.4 mm and 0.65 mm, respectively. The dimensions of the antenna are given in Table 8.2.

Table 8.2: Dimensions for the antenna shown in Figure 8.6

Parameters	L	q	s	l_1	w_1	w_2
Dimensions (mm)	7.15	0.65	1.24	1	2.6	0.15

Another row of vias with a diameter of 0.3 mm is also inserted into the substrate, to act as the directors of the Yagi-Uda antenna. The vias are loaded at the top and the

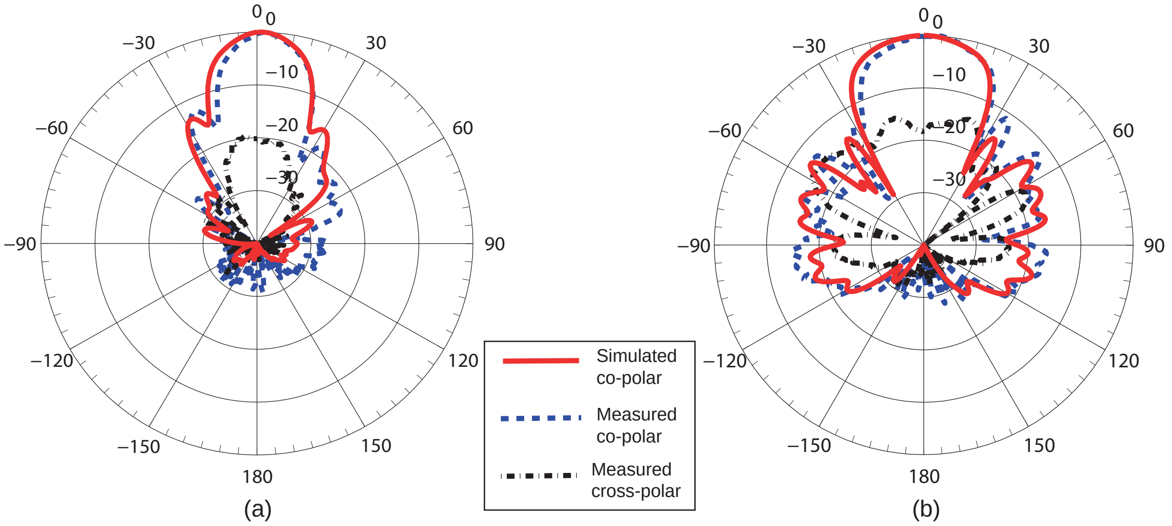

Figure 8.5: Radiation pattern of the printed Yagi array at 60 GHz: (a) E plane; (b) H plane (radial scale in dB).

bottom with printed strips to make sure the equivalent length of the directors is half a wavelength. The width of strips is 0.15 mm. The same process has been done for the tapering of director length and spacing as discussed in Section 8.3. The spacing between the adjacent strips is gradually decreased from 1.24 mm to 1.05 mm by a tapered factor of 0.98. The length of the strips is reduced according to a geometric series in order to achieve higher gain and lower sidelobe level. As high currents flow in the vias of the parasitic elements, the radiated polarisation is normal to the substrate, unlike the printed Yagi-Uda array described earlier, which is polarised in the plane parallel to the substrate.

A multi-step transition between the SIW and the WR15 standard air-filled waveguide is used to perform measurements. It uses a three-step quarter-wavelength impedance transformer.

The measurement results are presented below. The reflection coefficient of the SIW Yagi antenna is shown in Figure 8.7. Results show a good agreement between the simulation and the measurement.

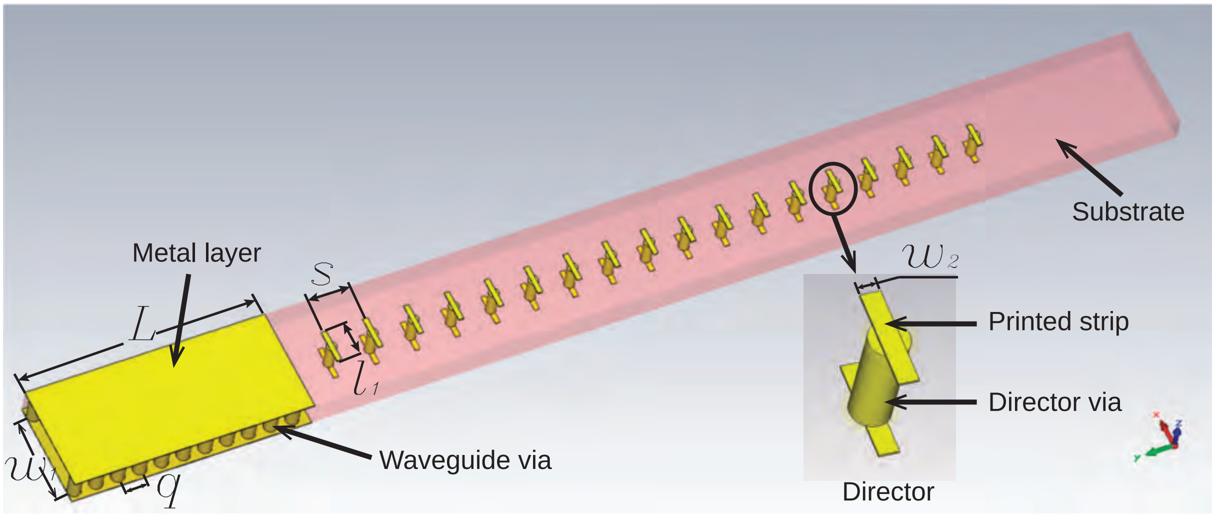

Figure 8.6: Schematic of SIW Yagi-Uda antenna.

Both the simulated and measured radiation patterns in E and H planes at 60 GHz are shown in Figure 8.8. The antenna gain measurement has been conducted using the gain transfer method. The measured maximum gain is 12.5 dBi. The larger backlobe in the simulation results is because of smaller transition used in simulation modeling than one used in the measurements due to fabrication requirements. The sidelobe levels are −9.7 dB and −11.2 dB in the E and H planes, respectively, which are higher than the sidelobes of the printed Yagi-Uda array. The 3-dB beamwidths in the E and H planes are 28° and 30°, respectively.

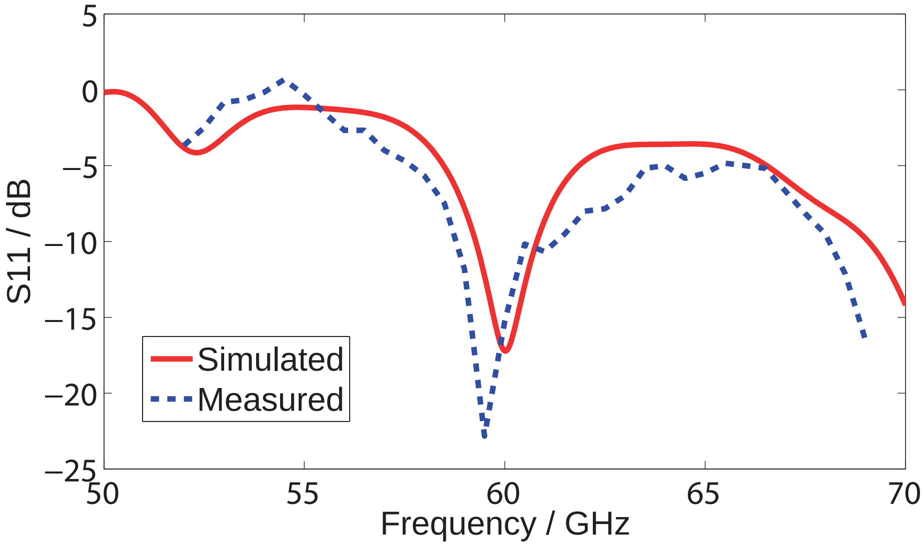

Figure 8.7: Reflection coefficient (S_{11}) of the substrate integrated waveguide Yagi-Uda antenna.

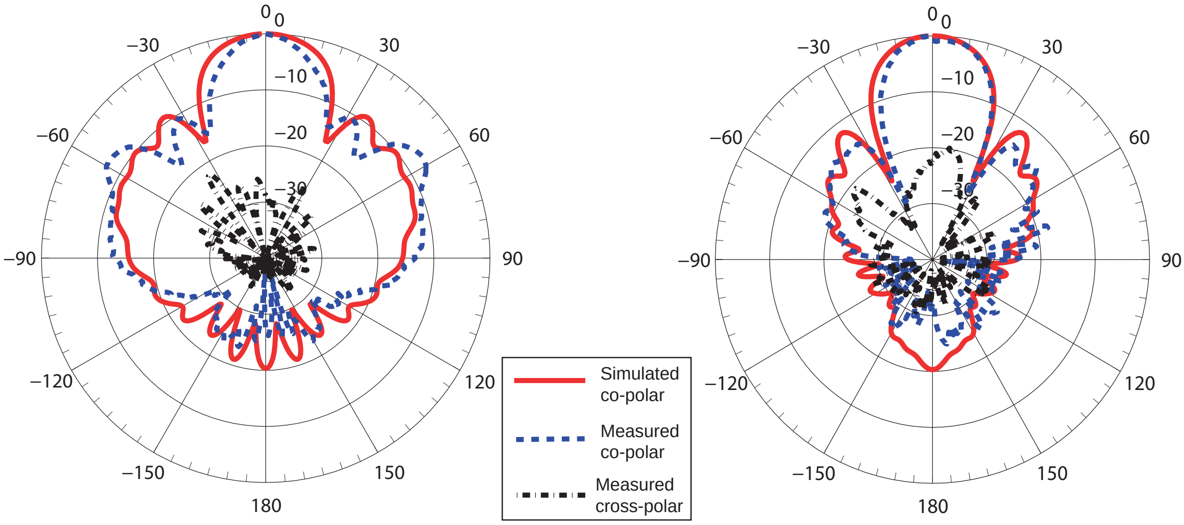

(a) (b)

Figure 8.8: Radiation pattern of the SIW Yagi-Uda antenna at 60 GHz: (a) E plane; (b) H plane (radial scale in dB).

8.5 Investigation of the In-situ Antenna Performance on a Phantom

8.5.1 Studies of antenna performance with different types of phantoms

It is known that antennas placed in close proximity to a lossy medium will experience antenna detuning, radiation pattern distortion, a change in input impedance and strong power absorption [205]. Hence, wearable antennas should be designed to operate robustly in close proximity to the human body, meaning that the influence of the body on antenna performance should be minimised. The interaction of antennas and the human body has been widely studied in mobile phone antenna design at lower frequencies [206, 207]. However, at millimetre wave frequencies, the electromagnetic coupling between antennas and the human body and the influence of the proximity of the human body on antenna performance are still not well understood. Some preliminary work has been carried out in this topic [208, 209]. Effects of the phantom on radiation pattern, reflection coefficient, and the specific absorption rate and incident power density have been investigated in such work, but much remains to be done such as effects of the material and size of phantom on the antenna performance.

In this study, we characterize the printed Yagi-Uda array and the substrate integrated waveguide Yagi-Uda antenna in close proximity to three different types of phantom, both through simulation and measurements. The phantoms used are a numerical skin phantom ($50 \times 20 \times 5$ mm^3, complex permittivity $= 7.98 - j10.9$ at 60 GHz), fresh meat ($70 \times 100 \times 5$ mm^3, pork steak-predominately muscle), and a physical skin-equivalent phantom ($100 \times 100 \times 20$ mm^3, complex permittivity $= 8.05 - j10.49$ at 60 GHz)[1] [210]. The distance between the antenna and the phantom is set to 5 mm, i.e. one free-space wavelength at 60 GHz. Figure 8.9 shows the Yagi-Uda antennas with different types of phantom. Figure 8.10 shows the co-polarised radiation pattern of the printed Yagi-Uda array in close proximity to the phantom. The solid curve shows the measured radiation pattern in free space. The dashed curve shows the simulated radiation pattern of the antenna in close proximity to the numerical skin phantom. The dotted curve and the dash-dotted curves show the measured radiation pattern of the antenna in close proximity to the fresh meat and the physical skin phantom, respectively. The measured maximum gains with the phantom in the H and E planes are around 18 dBi and 15 dBi, respectively. This difference arises because the main lobe of radiation pattern is lifted upwards off the phantom. In the E plane, all normalised radiation patterns show good agreement. But in the H plane, the radiation patterns are much more affected due to the presence of the phantom. The main beam of radiation pattern is lifted upwards away from the phantom by approximately 12°. However, all results are very similar, even though different types of phantom were used,

---

[1] The measurements with the physical skin-equivalent phantom were done by Dr. Nacer Chahat at IERT, University of Rennes 1, Rennes, France.

except that the beamwidth of the simulated pattern with the numerical phantom is 7° to 10° wider than the measured values in the H plane and the lift angle is 2° to 3° smaller because of the size of the phantom. This will be discussed in detail in Section 8.5.2.

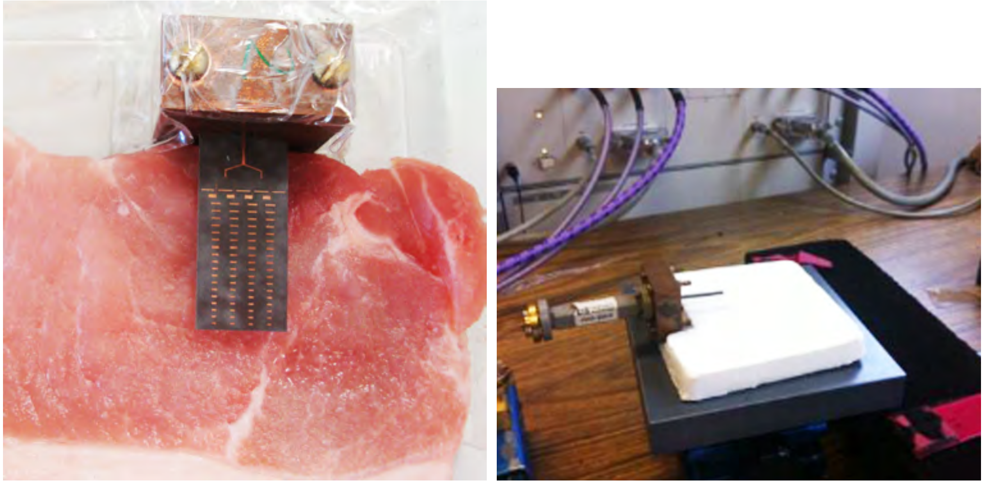
(a) (b)

Figure 8.9: Yagi-Uda antenna with phantom: (a) printed Yagi-Uda antenna with fresh meat; (b) SIW Yagi-Uda antenna with physical phantom.

Figure 8.11 shows co-polarised radiation pattern of the substrate integrated waveguide Yagi-Uda antenna in close proximity to these phantoms. The solid curve shows the measured radiation pattern in free space. The dashed curve shows the simulated radiation pattern of the antenna in close proximity to the numerical skin phantom. The dotted curve and dash-dotted curves show the measured radiation pattern of the antenna in close proximity to the fresh meat and physical skin phantoms, respectively. The measured gains in situ on the phantom in the E and H planes are around 11 dBi and 10 dBi, respectively. In the H plane, all normalised radiation patterns show good agreement to each other. However, in the E plane, the radiation patterns are significantly affected due to the presence of the phantom. The main beam of the radiation pattern is shifted away from the phantom by about 8°. From −90° to −40°, a much higher side lobe appears due to the presence of the phantom and from 0° to 90°, the normalised gain is much lower

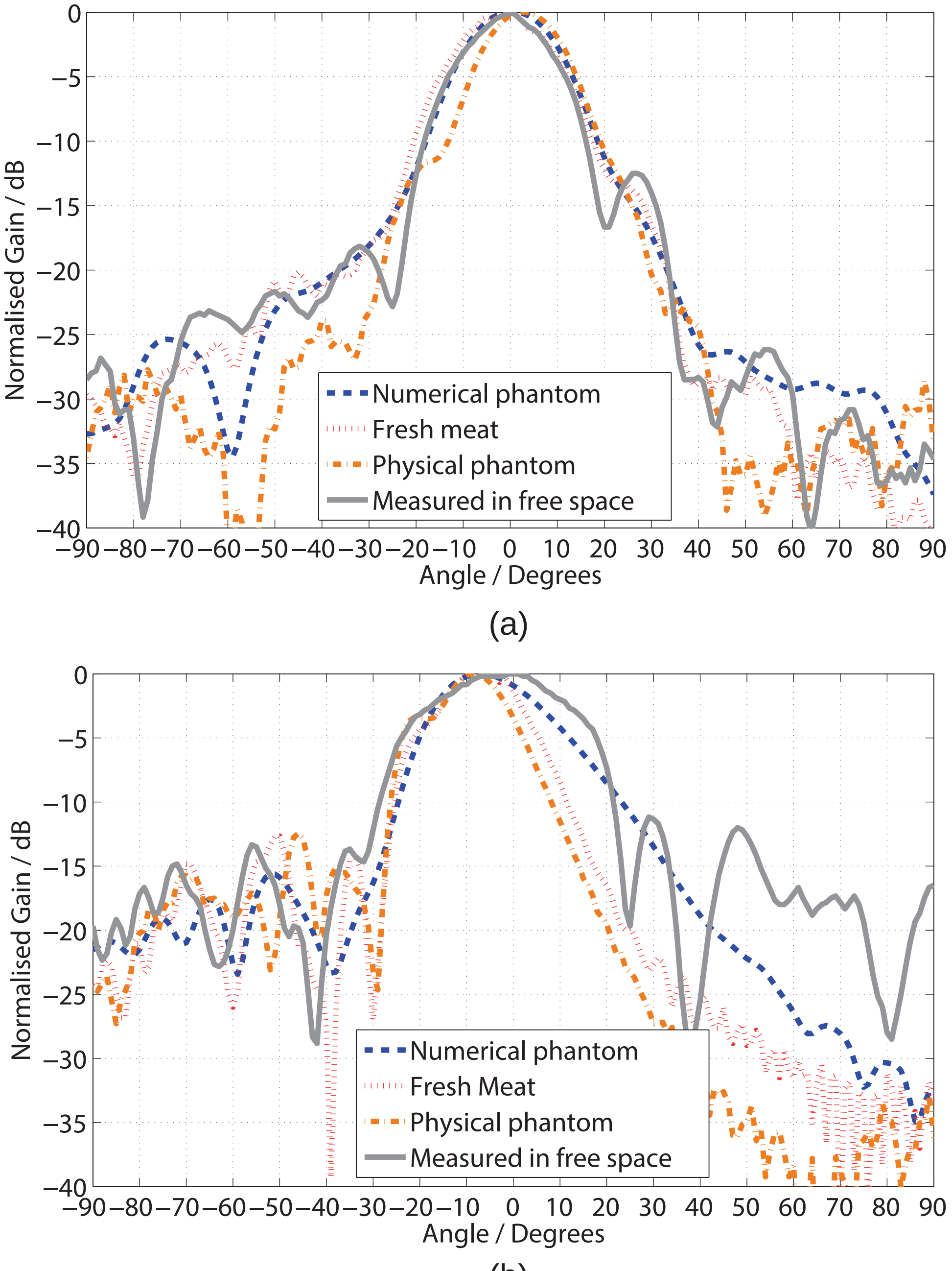

(a)

(b)

Figure 8.10: Radiation patterns of printed Yagi-Uda array in close proximity to phantom: (a) E plane; (b) H plane.

than that in free space. Moreover, the simulated result for the numerical phantom shows some discrepancies compared with other two results such as the wider 3-dB beamwidth and the lower sidelobe level.

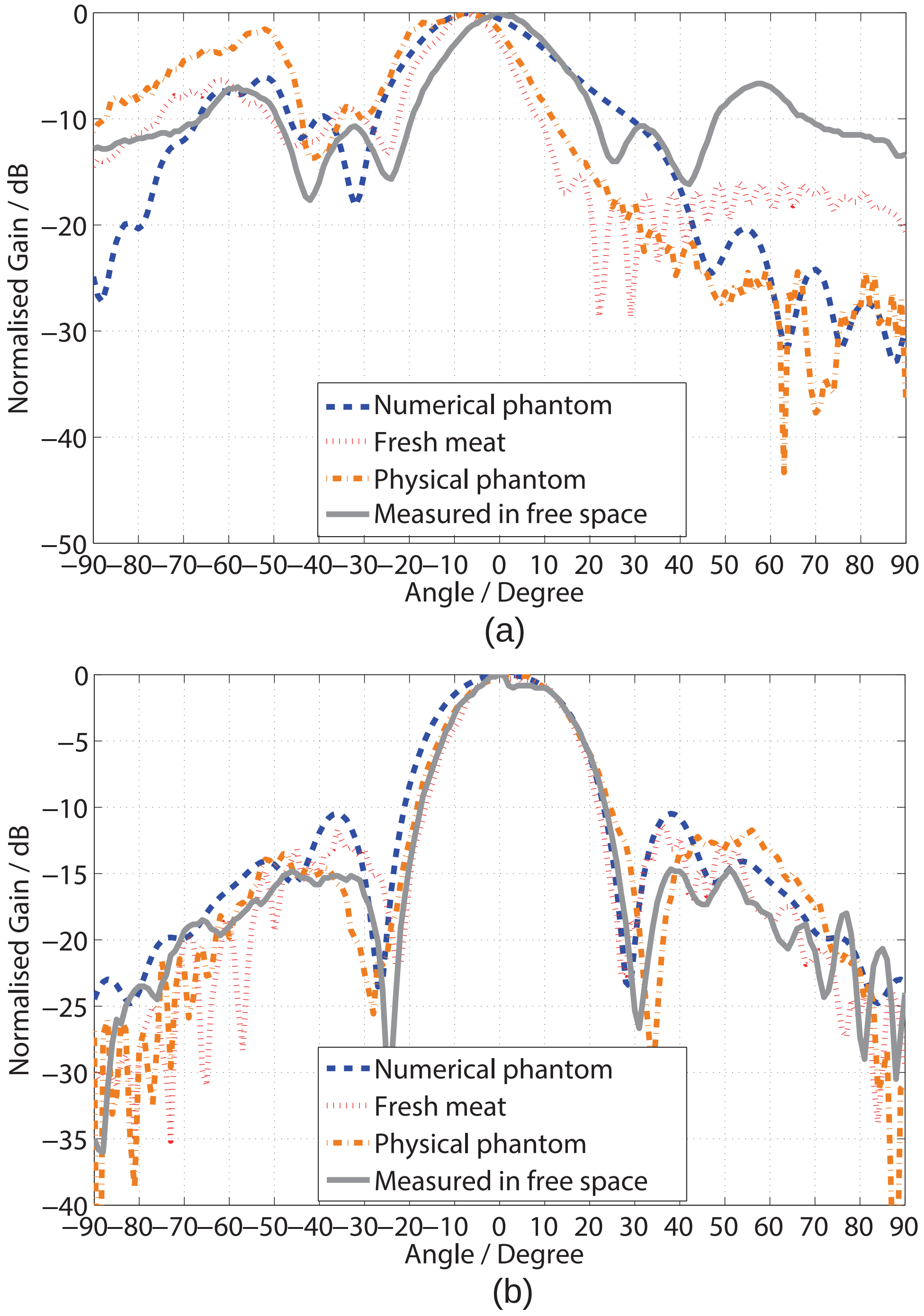

Figure 8.11: Radiation patterns of SIW Yagi-Uda antenna in close proximity to phantom: (a) E plane; (b) H plane.

The influence of the phantom on the antenna impedance match has also been investigated. As shown in Figure 8.12, the phantom causes both a mismatch as well as a detuning

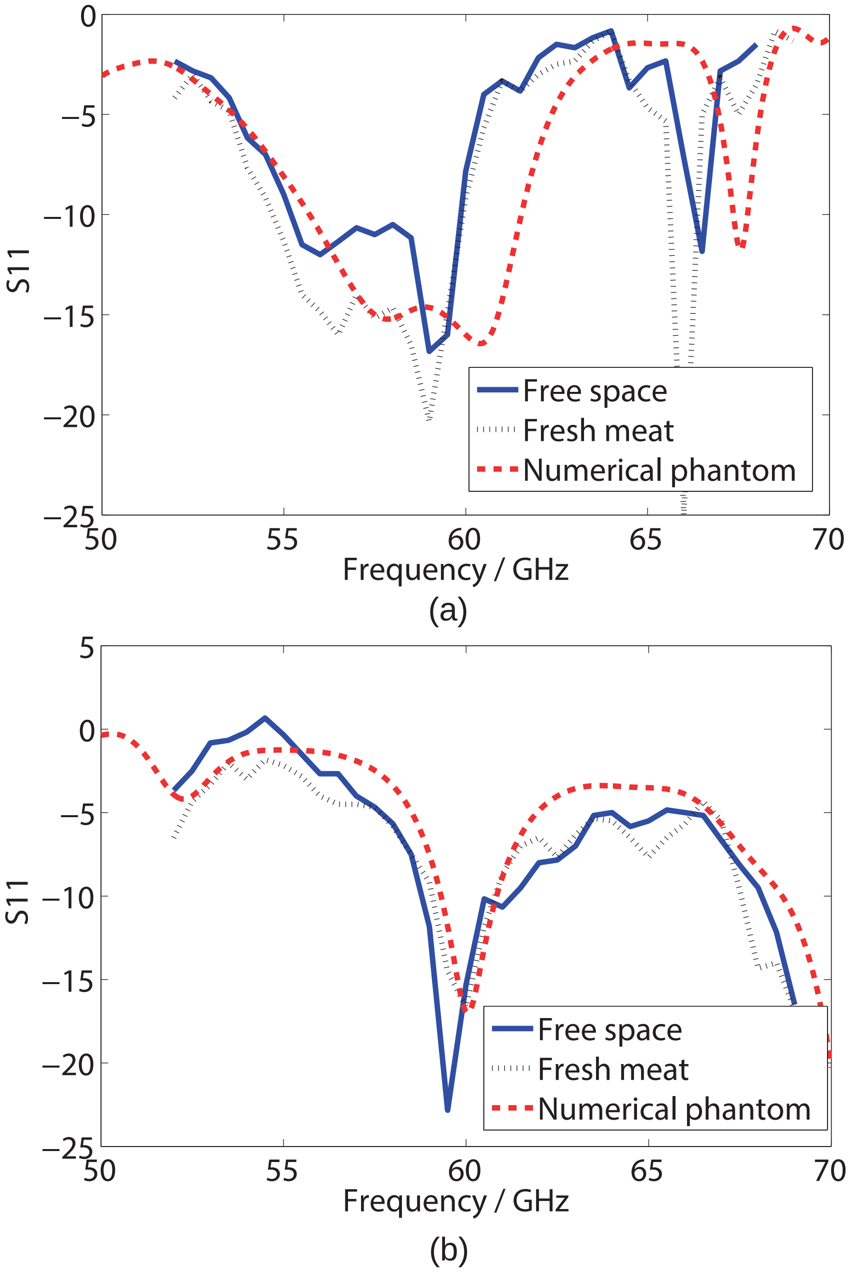

Figure 8.12: Reflection coefficient (S_{11}) of antennas with phantom: (a) printed Yagi-Uda array; (b) SIW Yagi-Uda antenna.

effect. However, these effects are not as significant as the effects on the radiation pattern.

8.5.2 Studies of antenna performance with different size of phantoms

In the preceding study results show that the numerical phantom gives rise to prediction discrepancies compared with the other types of phantom. We hypothesise that it arises because of the phantom size. In order to investigate this issue in more details, the printed Yagi-Uda array and SIW Yagi-Uda antenna predictions were recalculated with two different sizes of numerical skin phantoms in the simulation. The sizes of two phantoms are $50 \times 20 \times 5$ mm^3 which was used in the previous study, and $90 \times 80 \times 5$ mm^3.

Table 8.3: Studies of SIW Yagi-Uda antenna with different sizes of phantoms

	Small ($50 \times 20 \times 5$ mm^3)	Large ($90 \times 80 \times 5$ mm^3)
Shift angle in E plane (degrees)	5	8
3 dB beamwidth in E plane (degrees)	26.7	23.0
3 dB beamwidth in H plane (degrees)	29.2	28.8
Realised gain in E plane (dBi)	13	12.7
Realised gain in H plane (dBi)	12.6	11

Table 8.4: Studies of printed Yagi-Uda array with different sizes of phantoms

	Small ($50 \times 20 \times 5$ mm^3)	Large ($90 \times 80 \times 5$ mm^3)
Shift angle in E plane (degrees)	8	12
3 dB beamwidth in E plane (degrees)	19.5	19.1
3 dB beamwidth in H plane (degrees)	24.4	16.3
Realised gain in E plane (dBi)	16.1	14.3
Realised gain in H plane (dBi)	17.2	18.9

As shown in the Tables 8.3 and 8.4, there is a 3.7° difference in the 3 dB beamwidth in the E plane of SIW Yagi-Uda antenna and a 8.1° in the 3 dB beamwidth in the H plane of the printed Yagi-Uda array between the two phantoms, which strongly supports the assumption that the size of the phantom results in the previously observed discrepancies.

Besides, the lifted angle and realised gain are also affected by the size of the phantom. This study indicates that the positioning of the antenna has a significantly influence on the predicted antenna performance. For example, the same antenna placed on the wrist and on the chest will give different radiation patterns because the size and curvature of those parts of the body give different effects on antenna performance.

8.5.3 Numerical studies of antenna performance with different antenna/phantom spacings

The spacing between antenna and body is likely to fluctuate when the body is moving. Therefore, it is important to investigate the antenna performance with different antenna/phantom separations. In this study, we simulate a single element printed Yagi-Uda antenna with a $54 \times 36 \times 5$ mm^3 numerical skin phantom at different separations from 1 mm to 6 mm. Figure 8.13 shows the simulation setup. The layout and dimensions of the single element printed Yagi-Uda antenna are described in Section 8.3 The size of the antenna is $28 \times 6 \times 0.127$ mm^3.

Figure 8.14 shows the simulated reflection coefficient (S_{11}) for the single element printed Yagi-Uda antenna in free space and on the skin phantom for three different antenna/phantom separations, namely 1 mm, 3 mm and 5 mm. A slight detuning effect due to the presence of the phantom is observed. The smaller separation results in the stronger detuning effect. The minima of S_{11} are -38.7 dB, -28.4 dB, -31.3 dB and -34.1 dB corresponding to free-space, 1 mm, 3 mm and 5 mm separations, respectively. The respective minima frequency shifts compared to free-space are 0.46 GHz, 0.28 GHz and 0.48 GHz.

Figure 8.15 shows the simulated radiation pattern of single element printed Yagi-Uda antenna on the phantom at 60 GHz for free space and three different antenna/phantom

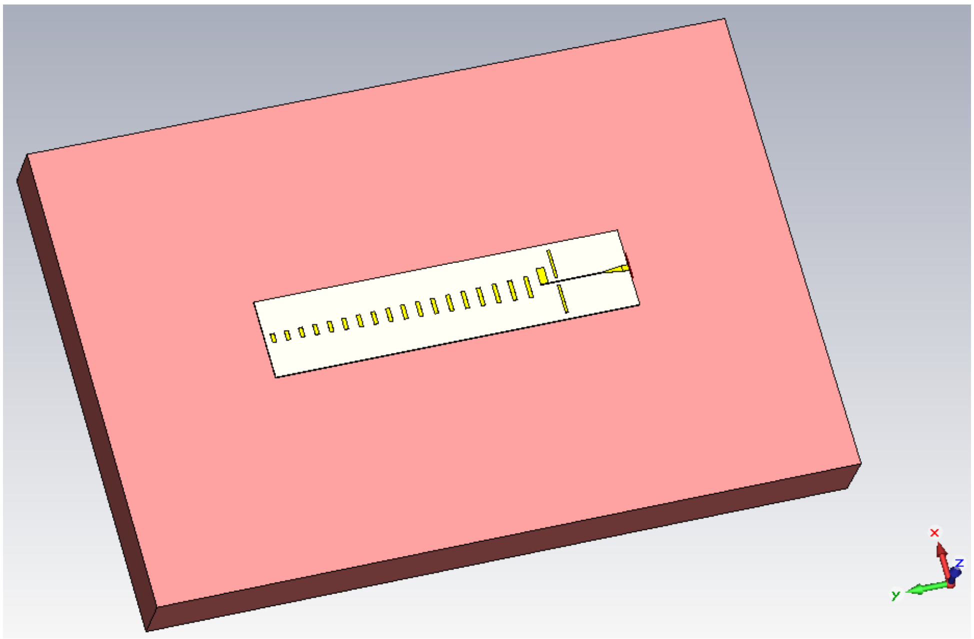

Figure 8.13: Single element printed Yagi-Uda antenna on the skin phantom.

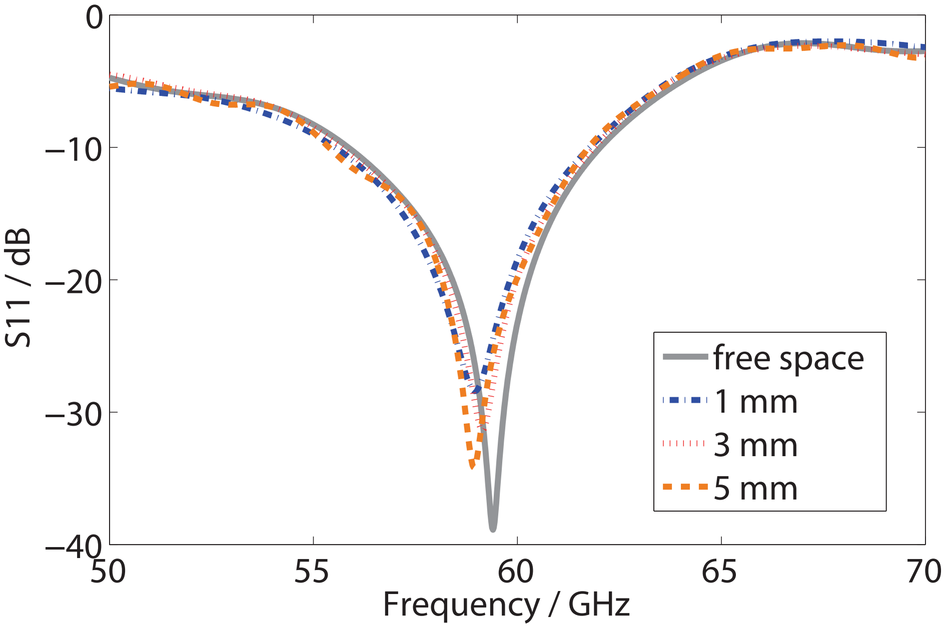

Figure 8.14: Simulated reflection coefficient (S_{11}) for the single element printed Yagi-Uda antenna in free space and on the skin phantom with different antenna/phantom separations.

separations. It is observed that the peak of the radiation pattern is strongly shifted due to the presence of the phantom. The smaller separation results in larger shift angle as shown in Figure 8.15(a). The radiation pattern in the H plane from 0° to 90° is affected significantly by the phantom. The realised gain in the E plane decreases with separation because of the lift angle.

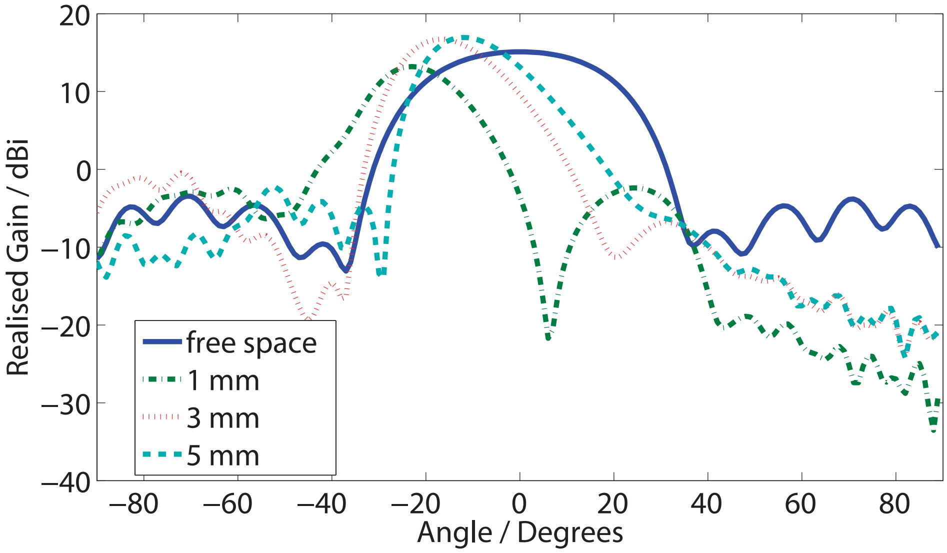

(a)

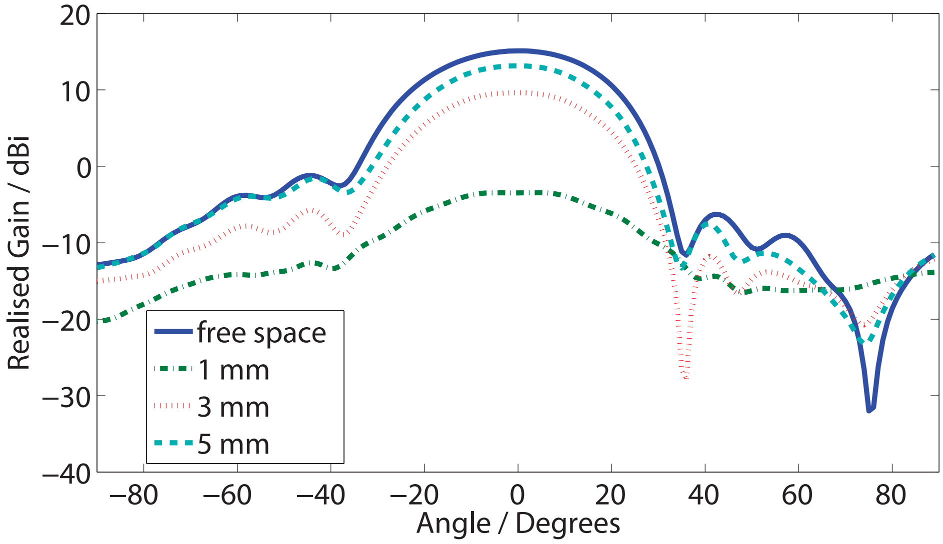

(b)

Figure 8.15: Simulated radiation pattern of single element printed Yagi-Uda antenna on the phantom at 60 GHz for free space and three different antenna/phantom separations. (a) H-plane (yz); (b) E-plane (xy).

Further parameter studies are shown in Table 8.5: the realised gain and efficiency increase with separation. The lifted angle increases when separation decreases. It is worth mentioning that the antenna performance is severely affected when antenna/phantom separation is at 1 mm, but is much more robust to ranging antenna/phantom spacing beyond 2 mm.

Table 8.5: Studies of antenna performance with different antenna/phantom separations

Separation (mm)	1	2	3	4	5	6
Realised Gain (dBi)	13.04	16.52	16.61	16.92	16.82	16.66
Efficiency (%)	63.07	82.39	88.06	90.73	91.87	92.41
3 dB beamwidth in H plane (degrees)	17.4	17.9	18.5	18.5	18.4	18.1
shift angle (degrees)	23	20	17	14	12	10

8.6 On-body Channel Measurements Using Fixed-beam Antennas

In the measurements, four types of 60 GHz fixed-beam antennas, namely a wideband quarter-wavelength monopole, a 20 dBi standard gain horn, a printed Yagi-Uda array and an SIW Yagi-Uda, as described in Sections 8.3 and 8.4, were used to investigate two typical on-body links, the belt-chest and the head-shoulder links. The belt-chest link is one of the most stable links for on-body channels, in contrast to the head-shoulder link which is much more variable due to the existence of the highly mobile shoulder and neck joints. The aim of the measurement was to investigate the antenna performance for 60 GHz on-body channels and to establish on-body antenna design requirements.

The measurements were conducted in an anechoic chamber using a Rohde & Schwarz ZVA67 VNA. The analyser was set to 60 GHz CW. The number of sweep points was 1001 and the sweep time was approximately 10 s. The output power and the measurement bandwidth were set to 10 dBm and 100 Hz, respectively. Two 2 m long coaxial cables were used to connect the analyser direct access ports to the antennas. The loss in the cables was measured as the cables were flexed randomly while connected together. It was found that the stress caused by rapid movements lead to deterioration of the cable performance, which introduces a ±1 dB magnitude measurement error. A through normalisation was performed before the measurements to remove the effect of the cables. With this setup, the RMS noise level in the VNA was found to remain at approximately the level of -89.6 dB.

The subject in the measurements was a 26-year old man of 175 cm height and 70 kg weight. Five transmit-receive combinations of the antennas were used in this measurement, namely, monopole-monopole, printed Yagi-horn, printed Yagi-monopole, SIW Yagi-horn and SIW Yagi-monopole. The antennas with the support of Styrofoam block were fixed on the body securely using belts and adhesive tape. Specifically, for the monopole antenna, due to the size of cable connection beneath the ground plane, the distance between the antenna and the surface of human body was 13 mm. However, because of the large transitions used in the printed Yagi-Uda and SIW Yagi-Uda antennas, the size of the foam block was larger to make these antennas robust and the attachment of them to the body tight. The distance between these latter two antennas and the human body was increased to 18 mm. It is worth mentioning that in real applications, wearable antennas are very desirable to be inconspicuous and mounting close to the body. However, in the channel measurements, it is difficult to keep this distance small due to the cable connection. Meanwhile, the antenna and its connection with the cable should be robust because the vigorous movements could be introduced in the measurement. The coaxial connector is usually the first choice, but in some circumstances, it is not robust enough. Especially, designing and manufacturing a low profile SIW to coaxial transition at 60 GHz is difficult. Therefore, we used waveguide transitions instead in our measurements which result in the larger antenna-body distance.

8.6.1 Belt-chest link

In this measurement, both the transmitter and receiver antennas were placed on the left hand side of the chest and belt, respectively. The distance between them was approximately 25 mm, which satisfies the far-field radiation condition for all the employed antennas. Three kinds of movement were introduced in the measurement, namely, deep breathing, turning truck left, and turning trunk right. During each sweep, the subject was performing a periodic movement, for example, a left turn of the trunk followed by a turn back to forward. The speed of the movement was kept slow and as smooth as possible in order to ensure the analyser captured the signal variation accurately. Figure 8.16 shows the setup for the belt-chest link using the printed Yagi and horn antenna combination.

Figure 8.16: Belt-chest link using a printed Yagi-Uda and horn antennas.

According to data shown in the Table 8.6, high gain antennas improve the link perfor-

Table 8.6: Belt-chest link using fixed-beam antennas (in dB scale)

	Breathing			Periodic movement left			Periodic movement right		
	max	min	median	max	min	median	max	min	median
M-M[1]	−61.3	−75.8	−66.7	−58.9	−68.3	−62.9	−61.3	−73.7	−67.6
P-H(Co)[2]	−33.6	−39.6	−36.0	−32.2	−38.1	−34.3	−33.8	−44.0	−37.2
P-H(Coss)[3]	−39.3	−46.4	−42.6	−37.2	−47.8	−42.8	−41.1	−54.6	−46.1
P-M	−56.2	−60.2	−57.5	−57.7	−64.2	−60.1	−57.5	−64.8	−59.7
S-H(Co)[2]	−31.3	−46.5	−37.9	−31.8	−36.3	−34.6	−32.6	−42.9	−34.6
S-H(Cross)[3]	−45.6	−60.1	−49.5	−42.5	−50.2	−46.5	−46.4	−59.4	−51.7
S-M	−56.3	−68.0	−59.2	−52.7	−58.6	−54.6	−54.0	−61.9	−56.2

[1] M stands for monopole antenna, P stands for printed Yagi-Uda antenna, H stands for horn antenna, S stands for SIW Yagi-Uda antenna.
[2] Co means two antennas were aligned with co-polarisation.
[3] Cross means two antennas were aligned with cross-polarisation.

mance significantly by reducing median path gain. For example, the result of using the printed Yagi-horn combination is to achieve up to 30 dB lower path gain than when employing the monopole-monopole combination. It confirms that a high gain antenna is really desirable for 60 GHz on-body channels. Besides, the SIW Yagi-monopole and the printed Yagi-monopole combinations always gave the smallest difference between max and min compared with the results of printed Yagi-horn and SIW Yagi-horn combinations. This is because of the omnidirectional pattern of the monopole antenna, which reduces the occurrence of a boreside misalignment pointing error. It also indicates that due to the narrower beamwidth, using high gain antennas at both ends of the link can lead to higher susceptibility to misalignment-induced "fading", especially when the body is moving.

Although the belt-chest link was thought to be the most stable link for on-body channels, small movements such as breathing can also cause deterioration in the link performance, especially for the SIW Yagi-Uda antenna. It is worth mentioning that breathing causes the belly and chest movements perpendicular to the body surface due to the motion of the diaphragm, which can in turn shadow the main signal path. Previous studies show that when placing the SIW Yagi-Uda antenna close to an experimental phantom, the antenna gain reduces significantly because the antenna is polarised normal to the body surface. Finally, when both antennas were placed on the left side of body, turning the trunk to the right results in much more path loss variability compared to when turning it to the left.

8.6.2 Head-shoulder link

Compared with the belt-chest link, the head-shoulder link is much more variable. The same combinations of antenna pairs were used in this set of measurements. In each measurement, one antenna was placed on the left side of head, just above the ear, as shown in Figure 8.17. The other antenna was placed on the front side of the left shoulder. Two movements were used in the measurements, periodically turning the head to the left and turning it to the right. Because this variation in geometry/antenna relative orientation introduces a severe polarisation mismatch along the link, at start point it was ensured that the two antennas polarisations were aligned.

The path gain results in Table 8.7 show that all antenna combinations suffer very large path gain variability due to the loss of line-of-sight path caused by turning the head, which indicates that fixed-beam antennas (including low directivity monopole antennas) cannot be relied upon to provide such a stable on-body link, due to the highly variable body geometry.

Figure 8.17: Head-shoulder link using fixed-beam antennas.

Table 8.7: Head-shoulder link using fixed-beam antennas (in dB scale)

	Periodic movement left			Periodic movement right		
	max	min	median	max	min	median
M-M[1]	−55.2	−82.0	−65.4	−56.7	×[2]	−60.3
P-H[1]	−54.5	×[2]	−66.1	−53.1	×[2]	−74.8
P-M[1]	−46.3	−82.6	−60.9	−57.4	×[2]	−64.7
S-H[1]	−48.2	−82.0	−54.9	−52.4	×[2]	−67.3
S-M[1]	−43.2	×[2]	−61.8	−56.0	×[2]	−64.3

[1] M stands for monopole antenna, P stands for printed Yagi-Uda antenna, H stands for horn antenna, S stands for SIW Yagi-Uda antenna.

[2] signal below noise

8.7 Two Back-to-back Antennas

As discussed in the previous chapter, due to the characteristics of 60 GHz radio propagation, high path loss and shadowing effects are significant challenges for 60 GHz body area networks. In order to establish reliable communication links on a human body, one possible solution is to use multi-hop networking with short-distance links. Hence, repeater nodes are needed in the multi-hop network. This section describes two back-to-back antennas which can be used in the RF front end of repeater nodes.

Figure 8.18 shows layout of two back-to-back antennas. It is formed of two identical single element printed Yagi-Uda antennas. The substrate used is Rogers RT5880 with dielectric constant 2.2. Two antennas are placed back to back. The back-to-back spacing is 0.9 mm. The overall size of the two back-to-back antennas is $48 \times 6 \times 0.127$ mm^3. Two ports are introduced to excite each antenna. Therefore, they can provide two diametrically opposite radiation beams.

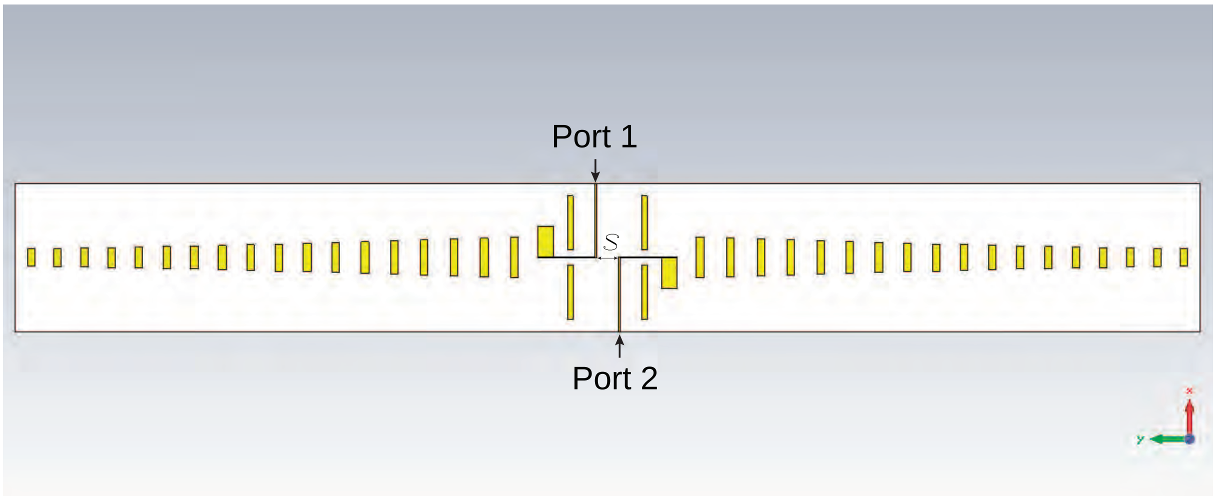

Figure 8.18: Two back-to-back antennas.

Figure 8.19 shows simulated scattering parameters of two back-to-back antennas. The isolation between two ports (S_{21}) is below -35 dB at 60 GHz.The antenna is resonant around 60 GHz as shown in S_{11}. S_{22} and S_{12} are the same as S_{11} and S_{21} by symmetry.

Figure 8.20 shows the simulated radiation patterns of two back-to-back antennas. Two directional beams towards the opposite directions are achieved by switching the feeding ports (the direction of the main beam by fed Port 1 is $+90°$ and the direction of the main

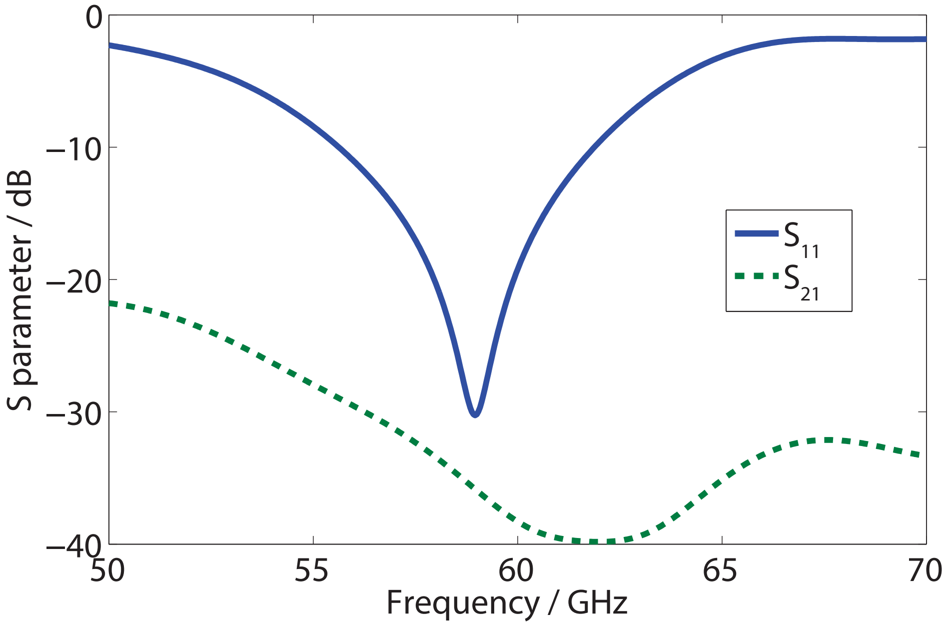

Figure 8.19: Simulated S parameters of two back-to-back antennas.

beam by fed Port 2 is $-90°$). The radiation patterns in the both E and H planes are quite symmetrical. Each beam has up to 15.3 dBi realised gain. The efficiency of antenna in free space is 97.6%.

8.8 Summary

This chapter describes two antennas: a printed Yagi-Uda antenna, a substrate integrated waveguide antenna, which are proposed for use in on-body communication channels at 60 GHz. The results show that they can achieve greater than 10 dBi gain, end-fire radiation pattern and a wide impedance bandwidth. Antenna performance has been characterised with different types of phantoms to investigate their suitability for on-body applications. The presence of the phantom results in a slight terminal impedance mismatch degradation and frequency shift. Much more significant effects are observed on the radiation pattern, especially in the plane normal to the phantom. The simulated and

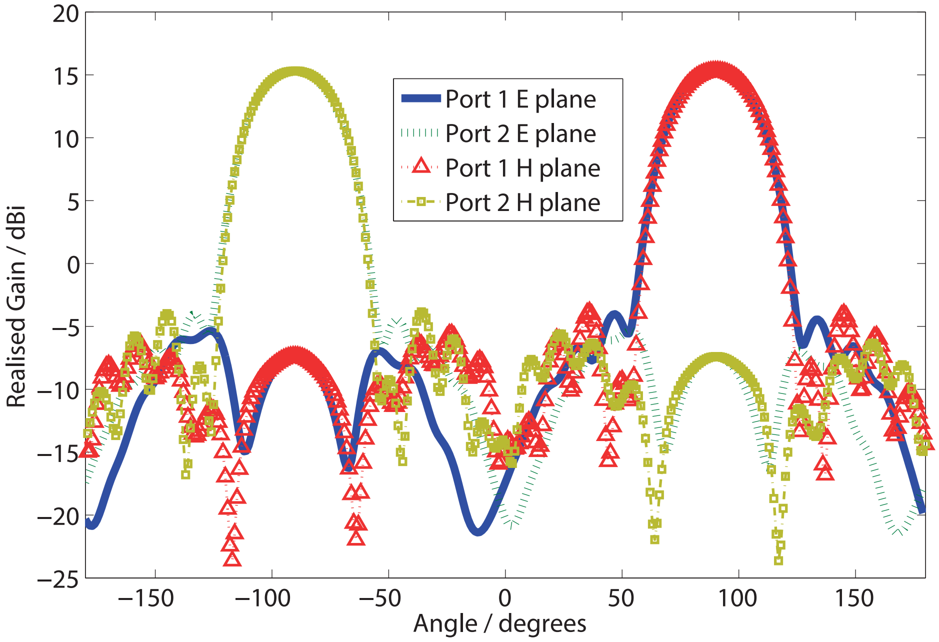

Figure 8.20: Radiation patterns of two back-to-back antennas in free space.

measured radiation patterns with a phantom show that the main lobe of the pattern is shifted away from the phantom surface by 8° to 12°. The difference of dielectric constant for different types of phantoms does not give rise to significant discrepancies between the results. The antenna/phantom separation has a severe impact on the antenna performance such as gain, efficiency, 3-dB beamwidth and the shift angle for the main lobe. The smallest, sub $\lambda/5$ separations result in worsening performance for the antenna. The larger phantom size causes more significant influence on the antenna performance than a smaller phantom, which suggests that different parts of the body can have a different impact on the antenna performance.

The most significant advantage for these antennas are their low profile form factor and easy integration in the body sensors compared to the traditional high-gain antennas such as the horn antenna. For the printed Yagis, they can be easily integrated in the PCB based RF circuitry and the SIW Yagis can be integrated in the SIW based system. It is worth mentioning that the antenna integration to the real system probably requires redesign the antenna to meet the new requirements, such as EMC and the different thickness of the substrate, but this work gives a general guideline for this kind of antenna design.

In order to investigate in situ on-body antenna performance and to establish more specific antenna requirements, on-body channel measurements are conducted for the belt-chest and head-shoulder links using fixed-beam antennas. Results show high gain antennas can improve the link performance significantly but are susceptible to pointing errors and shadowing.

Chapter 9

Reconfigurable Antennas for 60 GHz WBANs

9.1 Introduction

The primary thrust in using 60 GHz channels in applications of body area networks is to maximise the available bandwidth whilst reducing possible interference or eavesdropping. Previous chapters have demonstrated that directional antennas achieve the improved carrier-to-interference ratio, but are much more susceptible to the shadowing effect due to the narrow beam of the antenna and quasi-optical characteristics of 60 GHz propagation. However, advanced antenna technology and antenna signal processing will play a vital role in solving these problems. A reconfigurable antenna is useful in minimizing unwanted illumination of the wider body area whilst overcoming the fading or shadowing resulting in the loss of line-of-sight paths, by switching its radiation pattern beam direction. This strategy also leads to higher security, as the energy can be confined to the immediate vicinity of the body, thus giving good BAN-to-BAN and BAN-to-off-body receiver isolation. If and when required, such BAN antennas can switch to an outward facing beam. This has long been an aspiration for microwave BANs, however the low directivity of small antennas at lower frequencies prevents it from being practically realized. Nevertheless this idea can be realized at 60 GHz because of small size of antennas and wide available bandwidth.

In order to implement the pattern reconfigurability, one straightforward method is to use multiple antenna elements with switches. There has been extensive research in radio frequency microelectromechanical systems (MEMS) working at millimeter-wave frequencies, but there are still no commercial switches working at 60 GHz available in the market. Another widely studied approach for millimeter-wave beam-steering antennas is using a lens beamformer. However, this kind of antenna is not practical for on-body applications because of the high profile of the antenna. The third type is using a electrical beamformer, which generally divides into two categories. One is a circuit beamformer using transmission lines, connecting power splitters and couplers, to form the multibeam feeding networks. This method is feeding multiple antenna elements in parallel, e.g. a Butler matrix. The other method is frequency scanning, which achieves beam scanning by the variation of the carrier wave frequency. These two methods will be discussed in the following sections.

In this chapter, a stripline 4 × 4 Butler Matrix working at 60 GHz will be introduced, which is proposed for beam-switched antennas for on-body applications. A four-element dipole array with a Butler matrix was simulated to demonstrate its beam switching functionality. Circularly polarised and linearly polarised substrate integrated waveguide slot antennas will be presented. These antennas can scan their beam direction by changing their operating frequency. The on-body channel measurements using the linearly polarised SIW slot antenna were conducted for the wrist-chest channel. In the measurements, the subject was performing arm-swing movement to test beam-reconfigurability for the link performance improvement.

9.2 Butler Matrix

The Butler matrix is a type of beam-forming network, which was introduced by Jesse Butler and Ralph Lowe in 1961 [211]. By providing phase shifts among the output ports of the Butler matrix, the antenna beam is steered in specific directions in one plane. Figure 9.1 shows the configuration of a four-element antenna array with a 4×4 Butler matrix feeding network. The Butler matrix is formed of the 90° coupler, crossover, 45° phase shifter, and phase-adjusting transmission lines. By feeding the different input ports, the Butler matrix can provide four output signals with equal power levels and the progressive phases of $+45°$, $-45°$, $+135°$ and $-135°$, respectively. The direction of the main radiation beam of the antenna array can be switched by feeding the designated input port as shown in Figure 9.1. One drawback of the Butler matrix is if a larger number of beam directions is required, much more complex circuits have to be designed, and more feed network losses are expected.

As shown in Figure 9.2, a stripline 4×4 Butler matrix working at 60 GHz has been designed. A similar 60 GHz Butler matrix has been presented in [212], which was implemented in microstrip technology. In this work, the Butler matix was designed using a stripline technology, thus the pattern printed on both sides of the substrate is the same. For easily integrating the antennas on the same substrate, an RT/duroid 5880 substrate with 0.127 mm thickness was employed to implement the Butler matrix. As the line width of the 50 Ω striplines is too wide to effectively design the components for the Butler matrix, 100 Ω striplines were used. The overall size of the Butler matrix is 10.5×10.87 mm. The 90° coupler is designed using two pairs of 50 Ω and 100 Ω quarter-

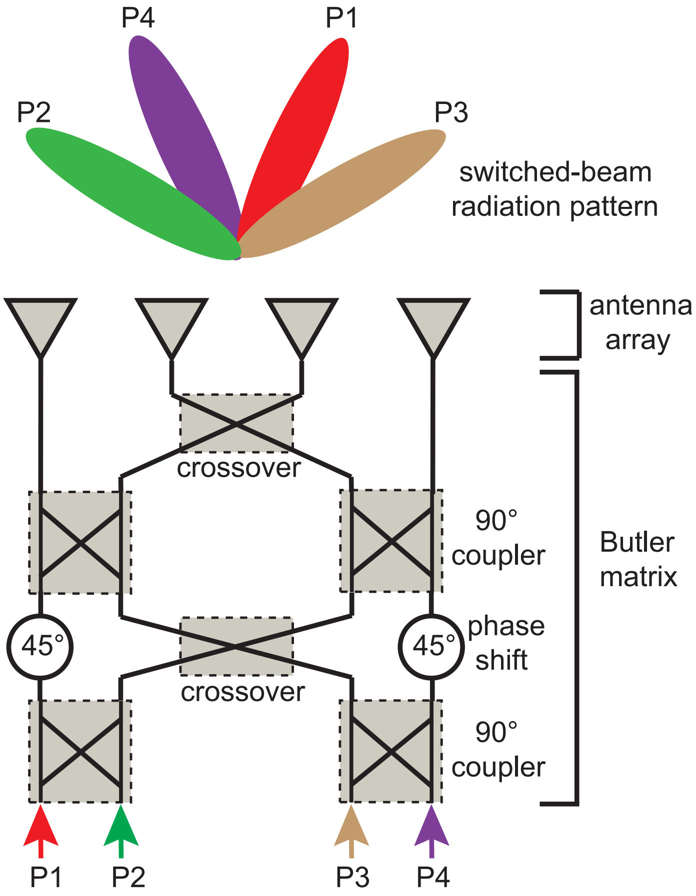

Figure 9.1: Configuration of the switched-beam antenna array with a 4 × 4 Butler matrix network.

wavelength striplines. The crossover is implemented by cascading two 90° couplers via two 100 Ω quarter-wavelength striplines. Moreover, meandered striplines are employed to adjust the output phases of the Butler matrix. The Butler matrix was simulated in CST Microwave Studio©, and Figure 9.3 shows the simulated magnitude and phase of the output signals from the 4×4 stripline Butler matrix. The magnitudes of the simulated output signals at 60 GHz are −6.88 dB, −6.84 dB, −7.07 dB and −6.61 dB, respectively, while the phase differences between two adjacent output ports are 129.2° , 136.8°, and 140° , respectively. The theoretical magnitude value is −6 dB, so about 1 dB loss is observed. The theoretical phase difference between adjacent output ports is 135°. Hence there is about 5° discrepancy between the theoretical value and the simulated value.

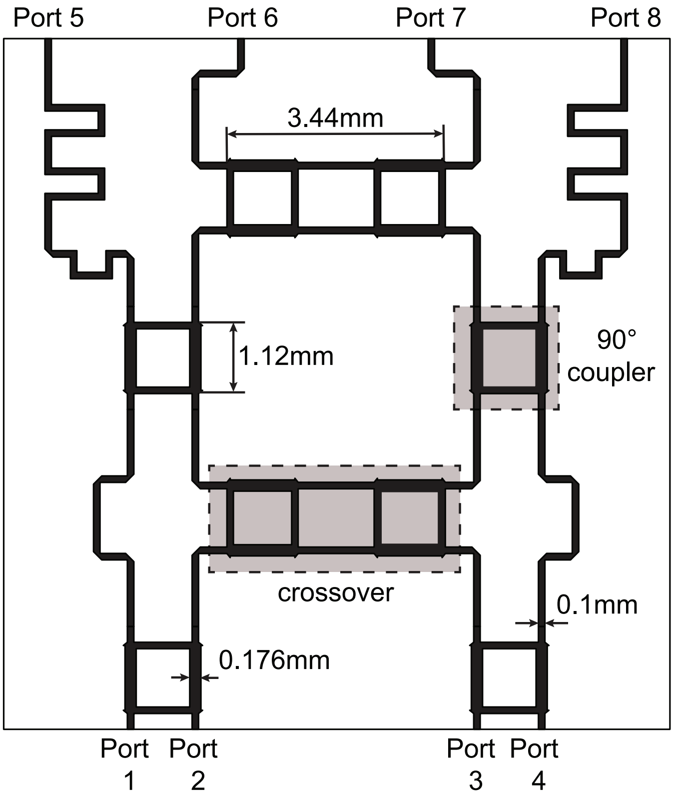

Figure 9.2: Layout of the stripline 4 × 4 Butler matrix network.

In order to demonstrate the beam-steerable functionality of the Butler matrix, a 4-element dipole array was simulated with the Butler matrix. Figure 9.4 shows the layout of the dipole array with the Butler matrix. The spacing between the adjacent dipole element is 3 mm. Figure 9.5 shows the simulated radiation pattern of the dipole array. The direction of each main beam with excitation at Port 1 to Port 4 is $-10°$, $33°$, $-33°$, and $10°$, respectively.

A Butler matrix based antenna can be placed conformally on the body and achieve beam switching in endfire, which is very suitable for on-body communications.

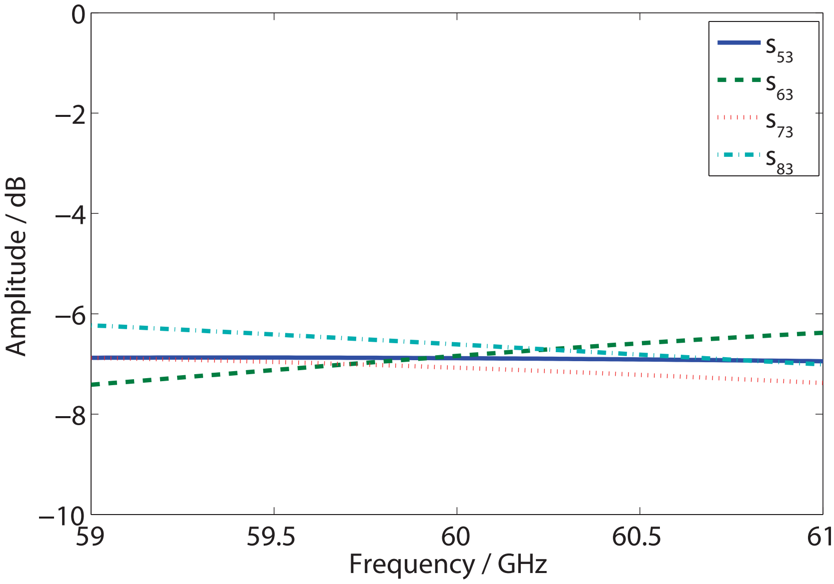

(a)

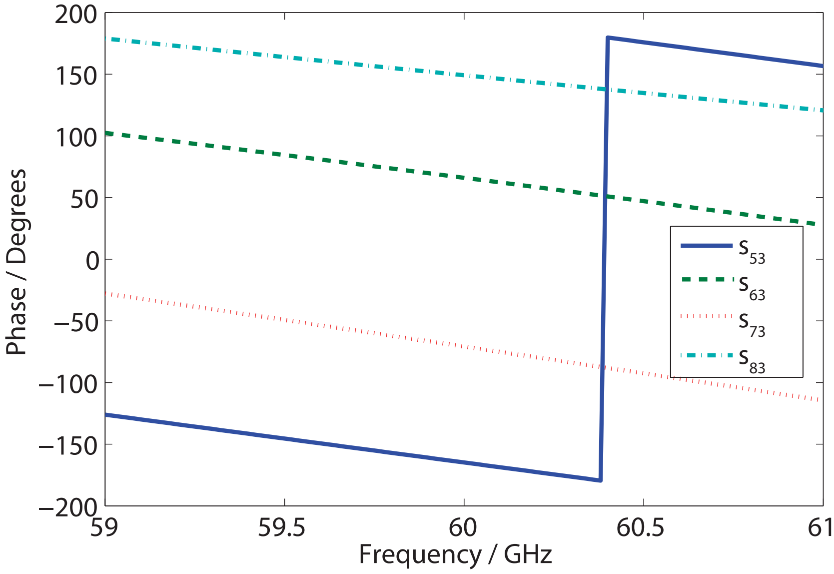

(b)

Figure 9.3: Simulated transmission coefficients of the Butler matrix network with port 3 as the input port: (a) amplitude, (b) phase.

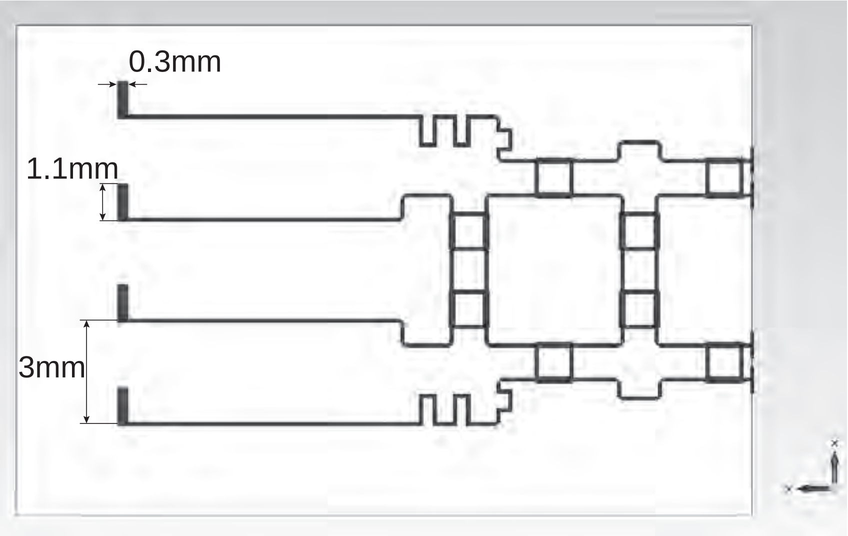

Figure 9.4: Layout of the dipole array with Butler matrix network.

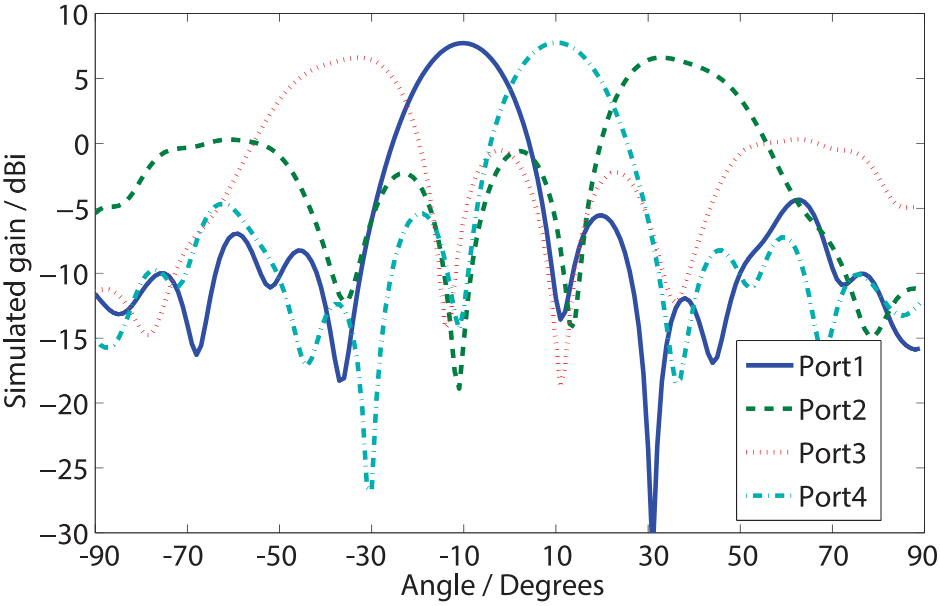

Figure 9.5: Simulated radiation pattern for the dipole array with Butler matrix network.

9.3 Frequency scanning antenna

The frequency scanning technique is an efficient and economical way to implement beam-scanning capabilities by using tuning the frequency. In the design of frequency scanning antennas, several important parameters should be considered: the range of scanning angle, the required frequency bandwidth, and the losses in the antenna. A frequency scanning antenna is usually a travelling-wave antenna, which is a case of serial feeding of multiple radiating elements. The principle of the frequency scanning antenna is based on the frequency dependent phase shift between the antenna elements created by a propagation delay in a transmission line. By varying the frequency, the angle θ between the axis of the main beam and the normal to the antenna array changes. As depicted in Figure 9.6, if the transmitted frequency increases then the beam travels up the face of the antenna while if the transmitted frequency decreases then the beam travels down the face of the antenna.

Travelling-wave antenna can be divided into two general categories: slow-wave antennas and fast-wave antennas. The wave on the latter type of antenna has a phase velocity greater than the speed of light and it is also called leaky-wave antenna which radiates continuously along its length and achieves highly-directive beams at an arbitrary specified angle with a low sidelobe level. The antennas presented in this section fall into this category.

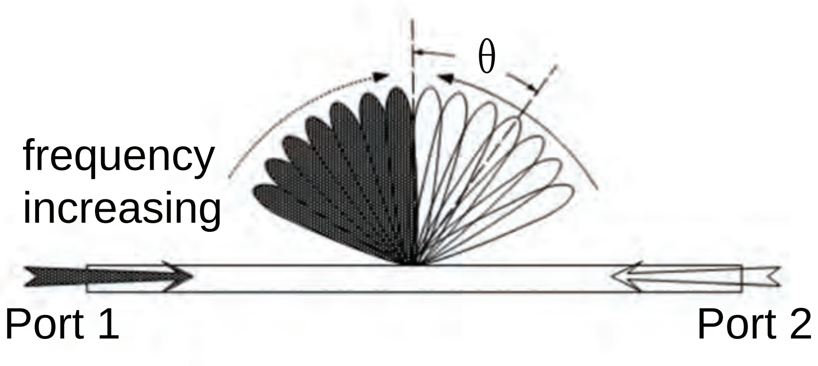

Figure 9.6: Basic principle of the frequency scanning antenna.

There are a number of implementations for frequency scanning antennas, such as the cascade-coupled radiating microstrip resonators [213] and waveguide slot antennas. However, microstrip antennas are quite lossy at 60 GHz and waveguide slot antennas are heavy and bulky, making them unsuitable for on-body applications. Therefore, two planar, light-weight SIW slot antennas are proposed. One is circularly polarised and the other is linearly polarised.

9.3.1 Circularly polarised frequency scanning antenna

A left-handed circularly-polarised SIW frequency scanning antenna is presented which consists of two leaky-wave arrays and phase shifters as shown in Figure 9.7. Each leaky-wave antenna has sixteen radiating slots arranged on the broad wall of the radiating SIW at ±45° to the waveguide axis. The substrate used here is Rogers 5880 with a thickness of 0.508 mm. At each end of the leaky-wave arrays, there is an equal-length unequal-width phase shifter, which introduces a 90° phase difference feeding each row of mutually orthogonal slots. Table 9.1 lists the simulated results of the phase shifter. A uniform slot spacing of 3 mm is used in order to achieve large bandwidth. If the slot spacing is not an integral multiple of half a guide wavelength and a matched load is used at the end, a leaky-wave array is obtained [214]. In ideal situations, when each port is excited, the incident wave is split into two equal portions with 90° phase difference. Combined with ±45° slots which provide two orthogonal field components, a circularly polarised radiated wave is achieved. Figure 9.8 shows part of the circularly polarised SIW slot antenna. The dimensions are listed in Table 9.2. The overall size of this antenna is $110 \times 6.2 \times 0.508$ mm^3.

By changing the propagation direction of the leaky wave, the scanning beams with left-handed circularly polarised mode can be generated in the opposite direction with tilting

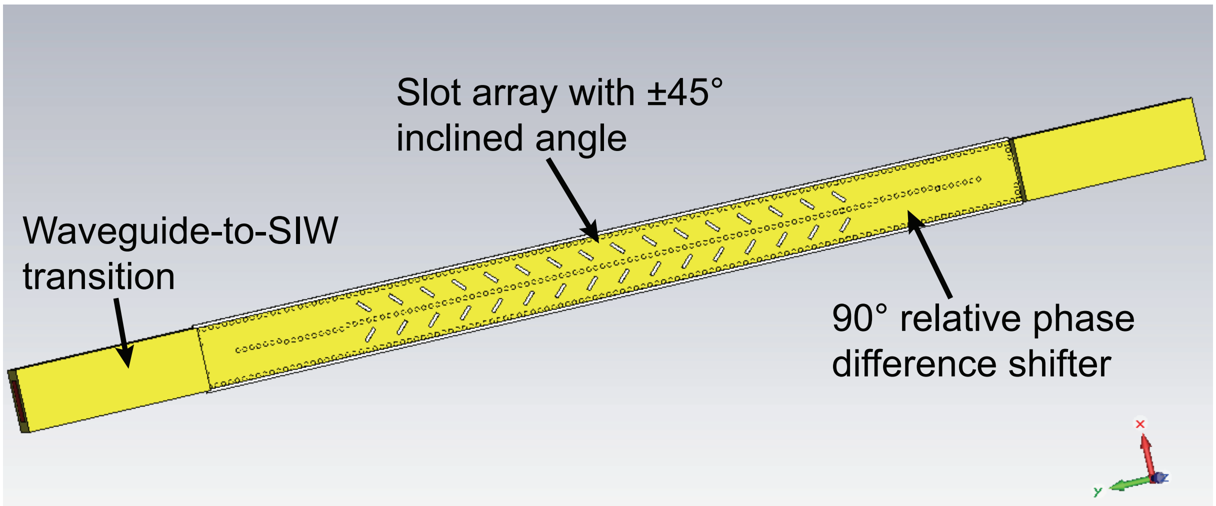

Figure 9.7: Circularly polarised SIW slot antenna.

Table 9.1: Simulated results of the phase shifter

Frequency (GHz)	58	59	60	61	62	63	64	65	66
Amplitude difference (dB)	0.46	0.94	0.96	0.57	0.05	0.5	0.7	0.54	0.15
Phase difference (degrees)	91	90.3	91	91	88.8	84.5	78.8	73.3	69.6

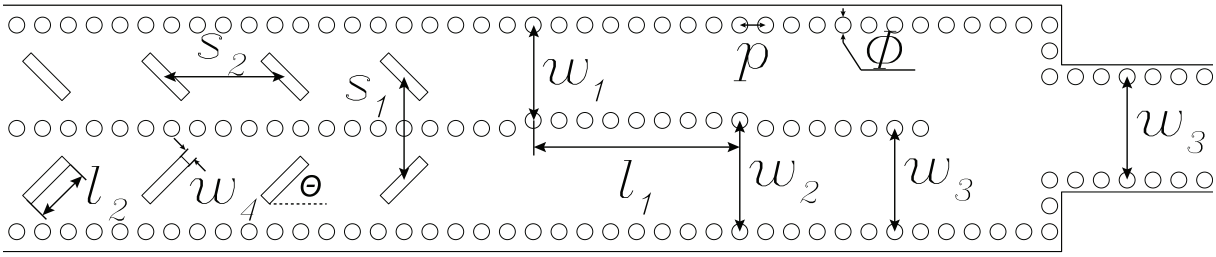

Figure 9.8: Part of circularly polarised SIW slot antenna layout with dimensions.

Table 9.2: Dimensions for the antenna shown in Figure 9.8

Parameters	w_1	w_2	w_3	w_4	l_1	l_2	s_1	s_2	p	Φ	θ
Dimensions (mm)	2.4	2.8	2.6	0.3	5.2	1.4	2.6	3	0.65	0.4	45°

angle other than broadside. Two SIW-to-waveguide transitions are used at each end of the antenna to feed the antenna. Figure 9.9 shows the simulated S parameters of the SIW frequency scanning antenna, where it can be observed that a 9 GHz operating scanning bandwidth corresponds to satisfactory antenna operation.

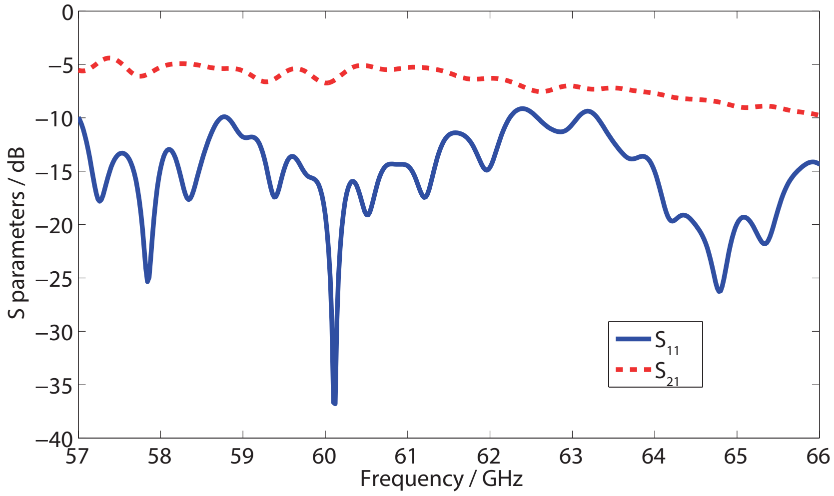

Figure 9.9: Scattering parameters of SIW slot antenna with transitions.

Figure 9.10 shows the simulated absolute radiation pattern[1] of the circularly polarised SIW slot antenna as a function of operating frequency when port 1 is excited. Due to the symmetry of the antenna structure, the pattern resulting from the excitation of port 2 is a mirror image of that of Figure 9.10 along the positive theta axis. The beam directions are scanned from −45° to −19° corresponding to 58 GHz to 66 GHz operating frequencies, respectively. The main lobe at each frequency has in excess of 10 dBi gain and an approximate 8° 3-dB beamwidth in the plane normal to the antenna surface and along the antenna length. Table 9.3 lists axial ratio of the simulated radiation pattern of the circularly polarised SIW slot antenna.

As shown in previous chapters, the depolarisation effect on the on-body channels is significant due to body movements. The use of circular polarisation would be helpful for mitigating this effect. But in this antenna design, the axial ratio is quite high at some frequencies and the sidelobe level is also higher than expected.

---

[1] Absolute value of the electric field derived from the two tangential and radial components: $E_{Abs} = \sqrt{\mid E_1 \mid^2 + \mid E_2 \mid^2 + \mid E_R \mid^2}$.

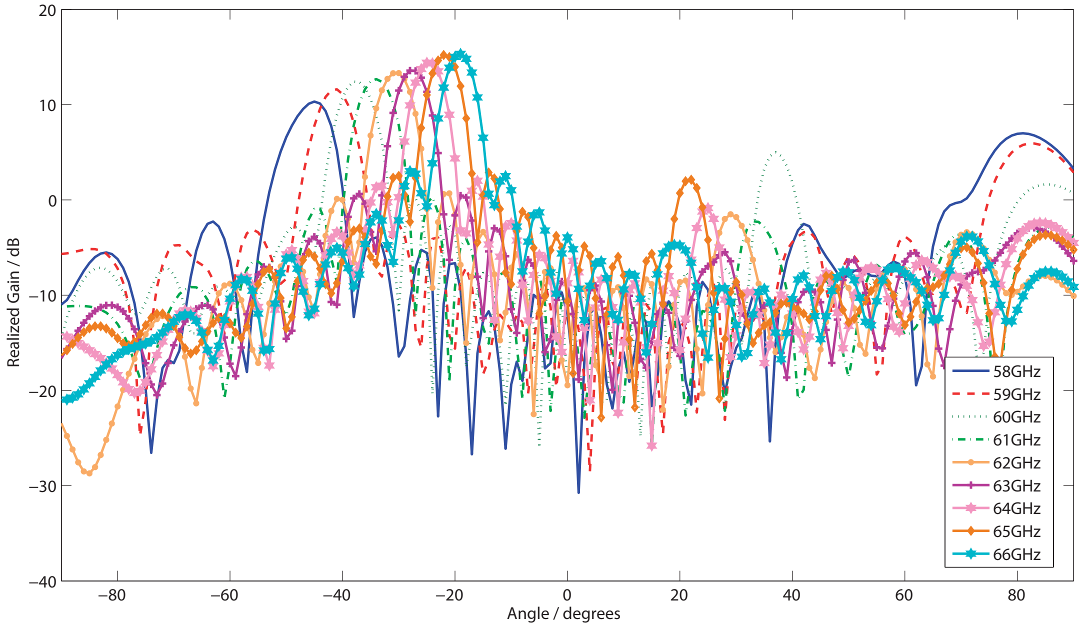

Figure 9.10: Simulated absolute radiation pattern of circularly polarised SIW slot antenna with transitions.

Table 9.3: Axial ratio of simulated radiation pattern

Frequency (GHz)	58	59	60	61	62	63	64	65	66
Axial ratio (dB)	8.2	7.2	9.1	3.2	1.8	3.4	4.1	2.9	2.1

9.3.2 Linearly polarised frequency scanning antenna

A linearly polarised SIW slot antenna was also designed. Figure 9.11 shows part of the linearly polarised SIW slot antenna. The dimensions are listed in Table 9.4. There are multiple slot pairs on the top metal layer of the substrate integrated waveguide. Quarter-guided-wavelength-spaced slot pairs introduce a reflection cancellation to achieve wide impedance bandwidth. Because two slots are spaced by a quarter guided-wavelength, round trip path-length difference between them is a half guided-wavelength and reflection waves from a pair disappear and travelling-wave excitation in the waveguide is realized [215]. Figure 9.12 shows the prototype of the linearly polarised SIW slot antenna with

SIW-to-waveguide transitions. There are 22 slot pairs in total. The overall length of the antenna is 128 mm. This antenna can be designed with shorter length and fewer slot radiating elements, but the gain of the antenna will decrease. A antenna with 12 slot pairs and the length of 80 mm was simulated, which achieves 10 dBi gain (6 dB lower than 128 mm one).

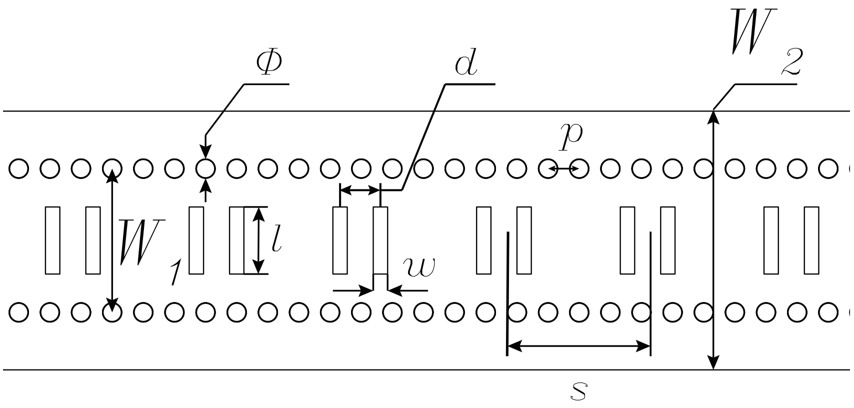

Figure 9.11: Part of linearly polarised SIW slot antenna layout with dimensions.

Table 9.4: Dimensions for the antenna shown in Figure 9.11

Parameters	W_1	W_2	Φ	l	w	d	p	s
Dimensions (mm)	3	5.4	0.4	1.4	0.84	0.3	0.65	3

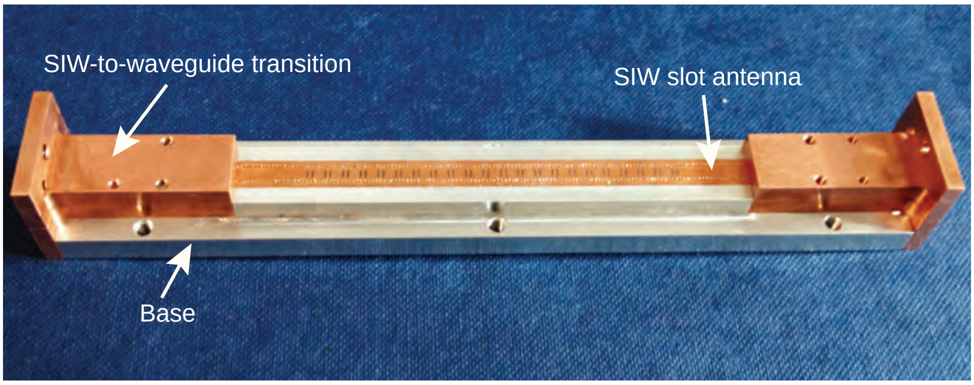

Figure 9.12: Prototype of linearly polarised SIW slot antenna with transitions.

For measurement proposes, two multi-step SIW to rectangular waveguide (WR15) transition were employed at both ends of the antenna. Figure 9.13 shows the scattering parameters of the linearly polarised SIW slot antenna. As shown in the figure, it achieves a wide impedance bandwidth from 57 GHz to 64 GHz. The measured transmission coefficient (S_{21}) is lower than the simulation, which means that less energy is transmitted from port 1 to port 2. This is because more energy is reflected at the input port and more loss is dissipated in the travelling-wave structure. Dissipation factor $tan\delta$ of the substrate material RT5880 in the simulation is 0.0009. This was tested at 10 GHz not 60 GHz. Hence, more loss is expected at 60 GHz compared to the simulation.

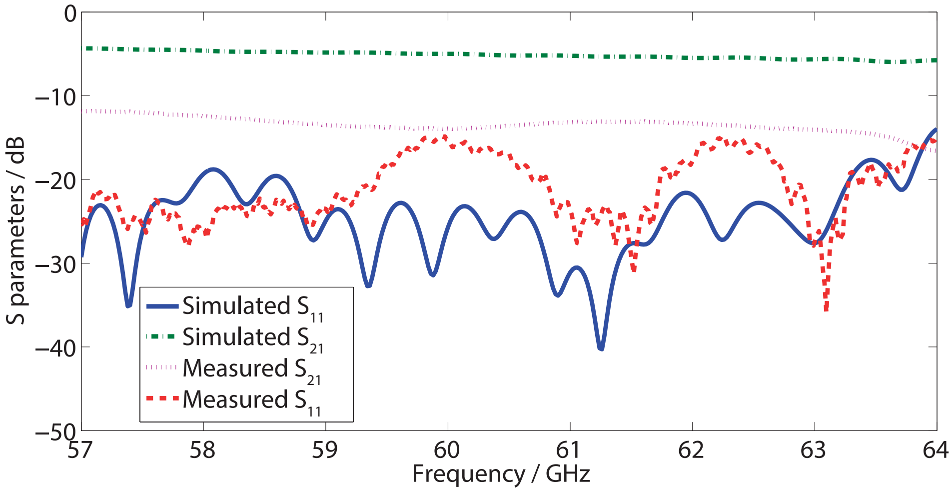

Figure 9.13: Scattering parameters of linearly polarised SIW slot antenna with transitions.

By scanning the frequency, the main beam of the radiation pattern is scanned accordingly. The coverage angle is from $-30°$ to $30°$ for both ports but the main beam of the antenna cannot cover the center ($0°$). The measured radiation pattern is shown in Figure 9.14 when one port is excited. This pattern is the E plane, which is normal to the antenna surface and along the antenna length. Due to the limitations of the measurement facilities, we cannot measure the H plane pattern. The sidelobe level is more than 10 dB lower than the main beam. The instantaneous bandwidth for each beam with certain pointing angle was calculated based on a half-power bandwidth limit from the simulated results. Table 9.5 lists the results of the simulated and measured radiation pattern and instantaneous bandwidth. From the table, the 3-dB beamwidth decreases when the main beam is scanning to the broadside.

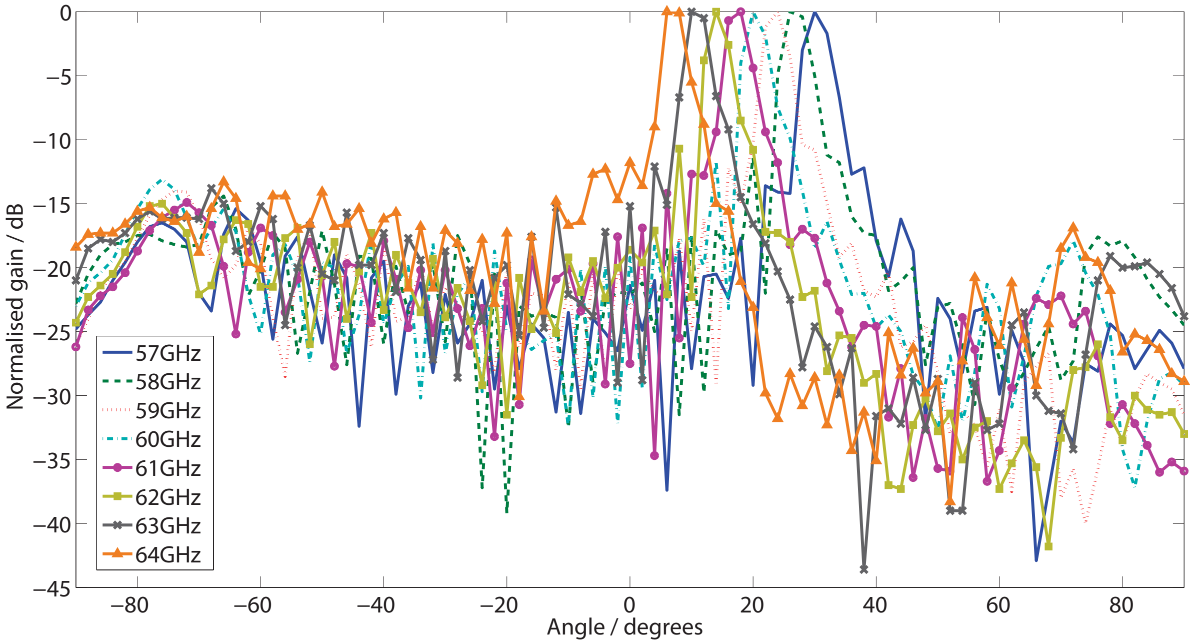

Figure 9.14: Measured radiation pattern of linearly polarised SIW slot antenna with transitions.

Table 9.5: Results of radiation pattern shown in Figure 9.14

Frequency (GHz)	57	58	59	60	61	62	63	64
Simulated beam direction (°)	31	28	25	22	18	15	12	9
Simulated gain (dBi)	14.7	15.2	15.6	15.8	15.9	16	16.1	15.9
Simulated 3-dB beamwidth (°)	4.6	4.3	4.2	4.1	3.9	3.9	3.7	3.6
Measured Beam direction (°)	30	27	24	20	18	14	10	7
Measured gain (dBi)	14.2	15.5	15	15.3	15.4	16	15.9	14.4
Instantaneous bandwidth (GHz)	1.0	1.3	1.2	1.1	1.1	1.2	1.1	1.3

The linearly polarised SIW slot antenna achieves better impedance bandwidth, higher gain and lower levels of the sidelobe compared to the circular polarised one. Hence, it was fabricated and used in the following on-body measurements.

9.4 On-body channel measurements using linearly polarised frequency scanning antenna

On-body channel measurements were conducted for a wrist-to-chest link in order to test the hypothesis that employing a reconfigurable antenna can improve the performance by using beam-scanning. As illustrated in Figure 9.15, a horn antenna was placed on the right wrist facing upwards, and the linearly polarised SIW slot antenna was placed on the right chest facing downwards. The horn was used as the transmitting antenna, and the signals received by both ports (Port1&2) of the SIW slot antenna were monitored simultaneously. In the measurement, the subject was swinging his arm sideways from the right to the left. We define the direction normal to the ground as 0°, the angle in the vertical plane on the right (the subject's right) is positive and the angle on the left is negative. The antenna placements on the real subject and body postures are shown in Figure 9.16. During the measurement, the VNA was sweeping the frequency from 57 GHz to 64 GHz and sampling 501 points, taking 135.27 ms for each sweep. The output power from the VNA was set at 10 dBm. No amplifier was used in this measurement. A through normalisation of the measured signal was performed before the measurement to eliminate the effect of the cables. The noise was -70.4 dB after normalisation. Because the VNA took time to sweep the frequency from 57 GHz to 64 GHz, it proved not to be fast enough to capture continuous motion of the arm; therefore the subject had to keep still during each frequency sweep, which means the subject performed multiple consecutive static postures. Overall, 9 postures were adopted during this arm-swing "motion". The arm lift angle was varied from approximately 40° to $-40°$ in steps of approximately 10°. To avoid slight movements affecting the results during the sweep, the sweep time was set at 135.27 ms as mentioned earlier. In order to make meaningful comparisons, the measurement was repeated by replacing the reconfigurable slot antenna with a horn antenna and subsequently with a monopole antenna. Each setup was measured three times and the average data are shown in Table 9.6 (the variances of the measured data are smaller than 6 dB). From the results, the SIW slot antenna achieved the best path gain compared to a horn or monopole in this scenario.

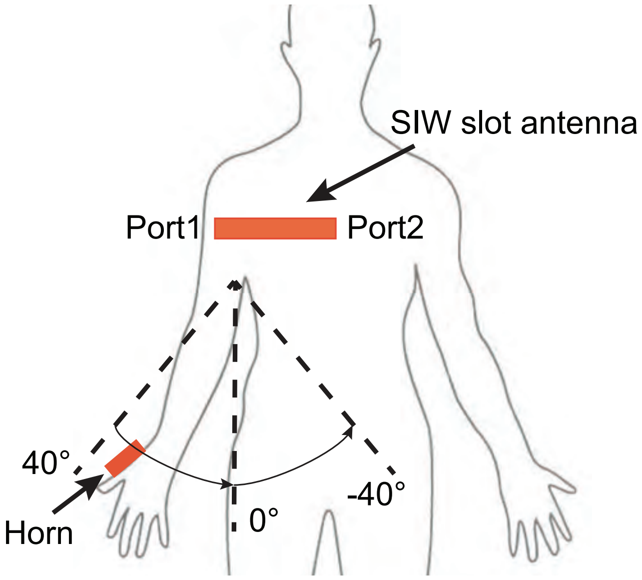

Figure 9.15: On-body channel measurement setup using frequency scanning antenna.

Table 9.6: Measured the best path gain (dB) for the wrist-chest channel

Arm position	SIW slot antenna	Horn	Monopole
40°	−43	×[1]	×
30°	−43.4	×	−60.7
20°	−41.3	−59.7	−51.4
10°	−32.9	−45.1	−43.7
0°	−50.8	−50.8	−56.8
−10°	−45.8	−50	−51.2
−20°	−51.8	−57.9	−54.2
−30°	−53.2	−58.3	−63.9
−40°	−52	×	×

[1] × signal below noise level

The results for one of measurements using the SIW slot antenna are listed in Table 9.7.


(a) (b)

Figure 9.16: Antenna placements for wrist-chest channel measurement and body posture: (a) 0°; (b) 40°.

This shows the maximum received signal and its corresponding frequency, received port and the approximate beam angle of the SIW slot antenna. These results demonstrate that a stronger received signal was achieved using beam-scanning, and the received port of the SIW slot antenna was switched from Port 1 to Port 2 during the arm-swing motion. However, it is worth mentioning that the approximate beam direction was arrived at based on the previous antenna radiation pattern measurement against frequency, so if the signal was not captured by the main beam of the SIW slot antenna, this beam direction could be wrong. For example, when the arm of the subject was swinging in the angular region between 0° and $-10°$, the main beam direction of the antenna based on the carrier frequency is expected at a wider vertical angle. Hence, it is probable that the received signal is from a sidelobe not the main beam. Another difficulty with this measurement is the antenna alignment in the H plane. There is a big chance that the main beam of the SIW slot antenna did not align with the main beam of the horn. Fortunately, the beamwidth in the H plane of the SIW slot antenna is wide, but it is very difficult to ensure that the peak of the beam is tracked correctly.

Table 9.7: Results for on-body channel measurement using the SIW slot antenna

Arm position	Maximum signal (dB)	Frequency (GHz)	Port	Beam direction
40°	−44.2	60.7	1	18°
30°	−43.2	62.4	1	12°
20°	−41.5	64	1	7°
10°	−33.7	61.7	1	15°
0°	−51.2	57	1	30°
−10°	−45.2	57	2	−30°
−20°	−51.1	62	2	−14°
−30°	−53.9	61.5	2	−15°
−40°	−52.1	60	2	−20°

9.5 Summary

In this chapter, two electrical beamforming techniques have been described. One technique is using the Butler matrix feeding network. A 4 × 4 stripline Butler matrix has been designed and simulated at 60 GHz. The simulation of a 4-element dipole array with this Butler matrix demonstrates its beam steering ability. The advantages of the Butler matrix are the ease of integration into the system and its planar low-profile form factor. The Butler matrix can normally achieve an even number of discrete beams and must work with multiple radiating elements. More importantly, to achieve a bigger number of beams, the design complexity will increase dramatically. Another technique considered is the frequency scanning. Two substrate integrated waveguide slot antennas have been proposed for the on-body communications. One is circularly polarised and the other is linearly polarised. These antennas work in a wide frequency range around 60 GHz and achieve beam-scanning with coverage of about 60°, but an angular region in the center cannot be covered by the main beam of the antennas. Some other disadvantages of the antennas are their sidelobe level is not low enough and the length of the antennas is too long, which makes them difficult to integrate into a system. Also, they have to be mounted normal to the body surface. However, on-body channel measurements of the wrist-chest channel with the arm-swing motion have been conducted with the linearly polarised SIW slot antenna and support the hypothesis that employing a reconfigurable antenna using beam-scanning can improve the performance. Results show the beam-reconfigurability of the antenna improves the link performance compared to the traditional fixed-beam antennas such as horns and monopoles.

It worth mentioning that this beam-scanning antenna is not suitable for all the on-body channels. It means that reconfigurable antennas have to be designed for specific on-body channels. Some important requirements should be considered according to the specific scenarios: conformability to the human body (depending antenna position on the body), beam scanning angle range, beamforming techniques, and beam scanning direction (endfire or broadside). In a real system, beamforming must be combined with the direction of arrival (DOA) estimation, which involves finding a spatial spectrum of the antenna array, and calculating the DOA from the peaks of this spectrum. However, this is outside the scope of this work.

CHAPTER 10

CONCLUSIONS AND FUTURE WORK

10.1 Final Conclusions

TECHNOLOGIES for wireless body area networks have been extensively developed in the past decade with the aim to provide reliable and efficient body-centric wireless communications. Wireless Body channel characterisation and compact and high efficiency antenna design for wearable electronic devices remain very challenging because of the unique properties of the human body as the primary environment for wireless communications. Some issues are still not satisfactorily solved for wireless communication systems for BANs. Privacy and security are considered key factors for wireless body area networks. Because many wireless devices are working at ISM narrow bands, interference from these systems is a big threat. Moreover, the mobility and uncoordinated operation characteristics of BANs makes interference between adjacent BANs difficult to avoid. Also, for some special applications such as in the military sector, highly secure and covert wireless communications are required. However, current standards such as Bluetooth and UWB do not provide good solutions to these problems. Besides, designing compact and high efficiency antennas for body-worn applications at these frequencies is very challenging. In addition, demand for high speed communications is increasing as more advanced cellular communication networks are deployed. This thesis proposed an alternative wireless solution for body area networks by adopting 60 GHz radio. By using 60 GHz, it can achieve high levels of electromagnetic energy control to minimise interference with other devices and susceptibility to observation and jamming. Also, antennas at 60 GHz can be made much more compact and efficient, which is very important for body-worn applications. Finally, high data rates can be achieved due to the existence of wide unlicensed spectrum around 60 GHz.

Channel measurements using a VNA with cable connections to body-worn antennas were first conducted to investigate on-body channels at 60 GHz and to establish wearable antenna design requirements. Two conventional antennas were used in the measurements: monopole antennas and horn antennas. Measurements show attenuation in the body channel at 60 GHz is much stronger than at lower frequencies, as intuitively expected. Horn antennas provide a significant advantage by improving received signal strength in the relatively stable channels such as the chest-waist channel, but they are much more susceptible to shadowing caused by body movements in the mobile channels. Results show horn antennas are problematic in establishing communication links in the highly mobile wrist-terminated channels due to their directional radiation pattern. However, monopole antennas achieved better performance than horns in these channels due to their wide radiation coverage. This suggests that the antenna radiation pattern requirement is determined by the antenna position on the body. Results also show that large signal fading is predominately caused by shadowing, antenna pointing error, polarisation mismatch, and distance changes. These variations are fairly slow with typical LCRs less than 1 s^{-1} and AFDs of more than 0.1 s. Also, multipath fading is much less prominent than at lower frequencies and only becomes significant when the signal level is low. Different polarisation combinations were investigated in terms of effect on path gain in the on-body channels. There is no single polarisation combination dominant in all on-body channels. One limitation faced in this work is the limited dynamic range of measurement system used. Some channels cannot be fully measured due to their high attenuation. Also, because of high loss in the cables relatively short cables were used in the measurements which restricts body movements to some extent. Possible solutions are replacing coaxial cables to optical fibres or using RSSI readings from stand-alone transceivers to remove cables. Finally, because the body channel performance is much more dependent to body movements at 60 GHz than at lower frequencies, the simultaneous motion characterisation with channel is recommended using motion capture technology to fully understand the correlation between channel performance and instantaneous body geometry.

Although attenuation of body channels is high, 60 GHz WBANs give lower interference and better covertness than WBANs at lower frequencies. A study was conducted to investigate interference between two persons wearing BANs in an indoor environment. Both monopole and horn antennas were used and two subjects were performing random movements in the measurements. Multiple antenna placements on the body were investigated. By adopting 60 GHz with monopole antennas, the interference signal level reduced up to 20 dB compared to 2.45 GHz. By using horn antennas at 60 GHz, a further 20 dB reduction of interference signal magnitude was observed. Hence, directional antennas can not only boost the wanted signals but also minimise the interference signals. Results also show that WBANs suffer higher levels of interference when placing an antenna on the wrist due to its highly mobile nature. CIR for multiple channels with different interferers were also investigated. Due to the limited number of antennas, a horn-monopole antenna pair at 60 GHz was placed on the each subject. The value of CIR is generally determined by the type of antennas and communication distance in the wanted channel, type of antenna for the interferer and the positions at which the antennas are placed. The best median CIR of 39.5 dB was achieved for the head-chest channel with a horn antenna interferer on the other subject at 60 GHz. The same measurements were repeated at 2.45 GHz with all antennas being monopoles on the both subjects, and best median CIR was 8.7 dB for the head-chest channel. It is expected that higher CIR can be achieved by using all directional antennas on both subjects. Due to the limitations of measurement setup, only two subjects can be considered in this study and they can only perform random movements in a small fixed area.

Covertness of WBAN communications was also investigated at the physical layer. A model of estimating the maximum detection distance at a threshold probability for detecting a WBAN wearing soldier in a battlefield was proposed based on body channel measurements at 2.45 GHz and 60 GHz in an environment with some scattering. These distances were calculated and compared for different conditions. Studies show at 0 dBm BAN transmitting power the soldier is not detectable at ranges greater than 50 m, while under the same conditions, the detection range at 2.45 GHz is up to 1540 m. Varying BAN transmit power and directivity of the detection antenna were also investigated for their effect on the detection distance. The analysis demonstrated that 60 GHz achieves much better covertness than 2.45 GHz even with higher BAN transmit powers and detection antenna directivity. In addition, a directional antenna on the soldier improves covertness and the position of antenna placement on the body has effects on the detectability. However, this model is considerably simplified because it is focused on covertness comparison for W-BAN at 60 GHz and 2.45 GHz. A further study can be done by considering more realistic system parameters such a dual polarised antenna array with high sensitivity receiver in a detection scenario.

Two high gain antennas were proposed for on-body communication channels at 60 GHz, namely a printed Yagi-Uda antenna and a substrate integrated waveguide antenna. These antennas can achieve gains greater than 10 dBi, end-fire radiation pattern and a wide impedance bandwidth. Antenna performance has been characterised with different types of phantoms to investigate their suitability for on-body applications. The presence of the phantom results in a slight terminal impedance mismatch degradation and frequency shift. Much more significant effects are observed on the radiation pattern, especially in the plane normal to the phantom. Other factors such as phantom size and antenna/phantom spacing were also investigated. Studies show spacing has significant effect on antenna performance especially when spacing is smaller than $\lambda/5$. The head-shoulder link and the belt-chest link were investigated with periodic body movements using combinations of fixed-beam antennas. Directional antennas show significant advantage of improving path gain in the belt-chest link, but in the head-shoulder link, they have more chance to lose line-of-sight communications. Due to the measurement system setup, bulky waveguide transitions were used to feed the antennas, which caused some problems in placing antennas on the body and also made separation between antennas and the body larger than expected. However, in real devices, antennas are expected to integrated on the PCB.

One major challenge for 60 GHz WBAN is only line-of-sight communications can be established and body movements deteriorate situations significantly. In order to counter the shadowing effect caused by body movements on directional antennas, reconfigurable antennas are proposed. The inspiration is when losing the line-of-sight the antenna can reconfigure its main beam direction to establish a new link. Two wideband substrate integrated waveguide slot antennas with linearly/circularly polarisation were proposed which can scan their main beam direction by changing their working frequency. The circularly polarised one is supposed to be useful for reducing depolarisation effect of on-body channels. The on-body channel measurements of the wrist-chest channel with the arm-swing motion using the linearly polarised SIW slot antenna demonstrates that the beam-reconfigurability of the antenna improves the link performance compared to the traditional fixed-beam antennas such as horns and monopoles. However, reconfigurable antennas have to be designed for specific on-body channels. Some important requirements should be considered according to the specific scenarios: conformability to the human body (depending antenna position on the body), beam scanning angle range, beamforming techniques, and beam scanning direction (endfire or broadside). In a real system, beamforming must be combined with the DOA estimation which requires more signal processing and add up system complexity.

This thesis introduces 60 GHz radio for wireless body area networks in technical details. On-body channels at 60 GHz have been characterised using monopole and horn antennas. Interference and covertness for WBAN at the physical layer have been studied. Also, fixed-beam directional antenna and reconfigurable antenna were designed and channel measurements using these antennas were conducted. Comparisons of three widely studied frequency bands for wireless body area networks are summarised in Table 10.1. Finally, based on the findings in this work, some suggestions are put forward to facilitate 60 GHz WBAN system design:

- The head-arm channel and the chest-waist channel are the most suitable for 60 GHz single-link WBANs. They are relatively stable and reliable and covert wireless communications can be established with high data rates and low levels of interference using directional antennas.
- The wrist terminated channel are problematic for 60 GHz WBANs due to its mobile nature. Beam-reconfigurable antennas or multi-link network are required to estab-

lish reliable wireless communications. Also, these channels exhibit higher levels of interference.

- Antenna design requirements are different for different channels and their positions on the body. Key parameters include the shape of radiation pattern, antenna gain, antenna polarisation, and conformability to the body. On-body channel characteristic must be taken into account in antenna design process.
- Better radiation control is achievable using beamforming techniques for 60 GHz WBANs, which can improve the channel performance and reduce the levels of interference, but requires sophisticated system design.

Table 10.1: Comparison of WBAN at different frequencies

Frequency	2.45 GHz	UWB	60 GHz
Spectrum availability	Congested	Congested	Under-utilised
Data rates	Mbps	Gbps	Gbps
Covertness	Not good	Good (Low power spectral density)	Excellent
Interference	High	Reduced interference to narrowband systems	Reduced interference (High path loss & atmospheric absorption)
Frequency reuse	Low	Low	High
Radiation control	Very limited	Limited	Good (Narrow antenna beamwidth & small antenna array)
Form factor	Bulky	Bulky	Small
Antenna efficiency	Low	Low	High

10.2 Future Work

As can be seen in the earlier chapters a significant amount of effort has been devoted to research into wearable antennas and body-area propagation at 60 GHz and compare the findings to lower frequencies. However, a number of issues still remain to investigated and resolved. A non-exhaustive list of significant issues that merit further investigation is given here:

1. **Multi-hop networks for 60 GHz WBAN**

   Previous studies show 60 GHz can only support relatively short distance communication on the human body. One possible solution is to introduce relay node in a long distance communication. For example, a node on the chest can act as a relay node for the head-to-waist link. This redundant strategy can improve reliability of 60 WBAN. Studies can be done for simultaneous, joint-link channel characterisation and correlation investigation.

2. **Wideband channel characterisation for 60 WBAN**

   All the measurements in this thesis were conducted in narrow band. Because there is 7 GHz unlicensed spectrum around 60 GHz, it is worth investigating wideband channel performance for WBAN at 60 GHz. The challenge of this study is a good channel sounder is needed with high dynamic range and fast sampling rate.

3. **Better radiation control for body area networks at 60 GHz**

   Further studies on reconfigurable antennas for 60 GHz WBAN can be done to achieve better radiation control, such as reconfigurable antenna design for different channels and different scenarios using different beamforming techniques.

4. **Antenna-channel decoupling (de-embedding)**

In the on-body propagation studies, in general, antennas are considered as a part of the channel, and therefore all these studies are, to some degree, antenna specific. If the propagation channel could be characterised independently of the antennas, this would greatly simplify the tasks of characterising the channels and communication system design. However, de-embedding the antennas from the channel has proved difficult so far because in body-area links propagation takes place through a mixture of space waves and creeping surface waves, depending on the particular channel. While the ability of an antenna to launch space waves can be described in terms of antenna gain and radiation pattern, its ability to launch surface waves is more difficult to establish, in large part because it is not clear what types of surface waves can be supported by the body at 60 GHz. Besides, the variability of antenna properties caused by changing body posture has to be taken into account. But this issue is probably simpler because normally the line-of-sight space wave is dominant propagation mode for 60 GHz WBAN channels. This issue can be further studied with the use of computer simulations as well as more theoretical analysis of the wave modes propagating around human body.

5. **Modelling on-body channels in realistic environments**

   Computer simulation is a useful tool which allows to avoid costly measurement campaigns to characterise performance of an antenna or new device in various scenarios (body movements, environments etc.) in which it may be used. So far, the simulations have been limited to the body only. At 60 GHz, only part of the body can be considered. The environment could not be included in the full-wave simulations because of its large electrical size. Ray-tracing is the simulation method which is normally applied to such large simulation problems. Ray-tracing technique is well established for outdoor and indoor channel characterisation but it is still to be adapted for body-area propagation channels.

Appendix A

List of Publications

A.1 Refereed Journal Publications

1. **Wu, X.Y.**, Hall, P.S., "Substrate integrated waveguide Yagi-Uda antenna", *Electronics Letters*, 11(23):1541–1542, 2010.
2. **Wu, X.Y.**, Akhoondzadeh-Asl, L., Hall, P.S., "Printed Yagi-Uda Array for On-Body Communication Channels at 60 GHz", *Microwave and Optical Tech-nology Letters*, 53(12): 2718–2730, 2011.
3. Nechayev, Y., **Wu, X. Y.**, Constantinou, C. C., Hall, P. S., "Millimetre-Wave Path Loss Variability Between Two Body-Mounted Monopole Antennas", *IET Microwaves, Antennas and Propagation*, 7(1):1–7, 2013.
4. Pellegrini, A., Brizzi A., Zhang, L., Ali, K., Hao, Y., **Wu, X. Y.**, Constantinou, C.C., Nechayev, Y., Hall, P.S., Chahat, N., Zhadobov, M., and Sauleau, R., "Antennas and Propagation for Body Centric Wireless Communications at Millimeter Wave Frequencies: a Review", *IEEE Antennas and Propagation Magazine*, in press.

A.2 Conference Publications

1. [1]**Wu, X.Y.**, Akhoondzadeh-Asl, L., Wang, Z.P., Hall, P.S.,"Novel Yagi-Uda antennas for on-body communication at 60 GHz", *Loughborough Antennas and Propagation Conference (LAPC)*, Loughborough, UK, Nov. 2010.

---

[1] Best Student Paper Prize

2. [2]**Wu, X.Y.**, Nechayev, Y, Hall, P. S., "Antenna Design and Channel Measure-ments for On-Body Communications at 60GHz", *The XXX URSI General Assembly and Scientific Symposium of International Union of Radio Science*, Istanbul, Turkey, Aug. 2011.
3. **Wu, X.Y.**, Nechayev, Y.I., Constantinou, C.C., Hall, P.S.,"Investigation of Inter-User Interference of Wireless Body Area Networks at 60 GHz", *2012 IEEE International Symposium on Antennas and Propagation*, Chicago, USA, Jul. 2012.
4. **Wu, X.Y.**, Nechayev, Y.I., Constantinou, C.C., Hall, P.S.,Brizzi, A. , Pellegrini, A. , Hao, Y. , Parini, C.G., "Preliminary estimate for observability of 60 GHz wireless body area networks", *2012 IEEE Asia-Pacific Conference on Antennas and Propagation (APCAP)*, Singapore, Aug. 2012.
5. Nechayev, Y.I., **Wu, X.Y.** Constantinou, C.C., Hall, P.S., "Effect of body motion on propagation path gain at 60 GHz", *2012 6th European Conference on Antennas and Propagation (EUCAP)*, Prague, Czech Republic, March, 2012.
6. Constantinou, C.C., Nechayev, Y.I., **Wu, X.Y.** Hall, P.S., "Body-area propagation at 60 GHz", *Loughborough Antennas and Propagation Conference (LAPC)*, Loughborough, UK, Nov. 2012.
7. Nechayev, Y.I., **Wu, X.Y.** Constantinou, C.C., Hall, P.S., "Effect of Wearable Antenna Polarization and Directivity on On-Body Channel Path Gain at 60 GHz", *2013 IEEE International Symposium on Antennas and Propagation*, Orlando, FL, USA, Jul. 2013.
8. Asare, P., Dickerson, R.F., **Wu, X.Y.**, Lach, J., Stankovic, J.A., "BodySim: A Multi-Domain Modeling and Simulation Framework for Body Sensor Networks Research and Design", *8th International Conference on Body Area Networks*, Boston, MA, USA, Oct. 2013.

A.3 Publications in Preparation

1. **Wu, X.Y.**, Nechayev, Y.I., Constantinou, C.C., Hall, P.S., "Investigation of Inter-user Interference for 60 GHz Wireless Body Area Networks", to be submitted to *IEEE Transactions on Antennas and Propagation.*
2. **Wu, X.Y.**, Nechayev, Y.I., Constantinou, C.C., Hall, P.S., "Investigation of Covertness for 60 GHz Wireless Body Area Networks", to be submitted to *IEEE Transactions on Antennas and Propagation.*

---

[2] Student Prize Paper Competition Finalist

Appendix B

Substrate Integrated Waveguide Design Rules

SIW is formed of two periodic rows of metallic vias or posts connecting the top and bottom ground planes on the both sides of a dielectric substrate as illustrated in Figure B.1. The diameter D of the vias, the spacing b between the vias and the spacing W between the two rows of vias are the physical parameters necessary for the design of the guide. The spacing b must be small to minimise the leakage loss between adjacent vias. However, the via diameter D is also subject to the loss problem.

Two design rules related to D and b that are used to neglect the radiation loss are formulated [217],

$$D < \lambda_g/5 \tag{B.0.1}$$

$$b \leq 2D \tag{B.0.2}$$

The cutoff frequencies of the TE_{10}-like and TE_{20}-like modes of the SIW, with respect to

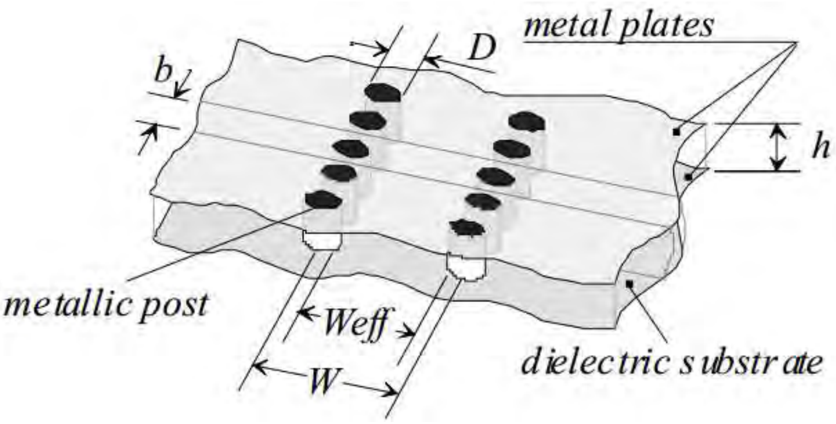

Figure B.1: Topology of an SIW guide realized on a dielectric substrate with its physical dimensions. Copy right of IEEE, reproduced from [216]

the diameter D and the spacing of the two rows of vias W are approximated in [218],

$$F_{C(\mathrm{TE}_{10})} = \frac{c_0}{2 \cdot \sqrt{\varepsilon_R}} \cdot \left(W - \frac{D^2}{0.95 \cdot b}\right)^{-1} \tag{B.0.3}$$

$$F_{C(\mathrm{TE}_{20})} = \frac{c_0}{\sqrt{\varepsilon_R}} \cdot \left(W - \frac{D^2}{1.1 \cdot b} - \frac{D^3}{6.6 \cdot b^2}\right)^{-1} \tag{B.0.4}$$

where c_0 is is the speed of light in free space. Note that Equation (B.0.3) and (B.0.4) do not depend on the thickness of the SIW h, which will only affect the Q-factor [219]. Also, the SIW is equivalent to a rectangular waveguide with the effective width W_{eff} and all the existing theoretical frameworks and design procedures developed for the rectangular waveguide can be directly applied to its synthesized counterpart. The effective width W_{eff} can be derived from Equation (B.0.3), as follows

$$W_{\mathrm{eff}} = W - \frac{D^2}{0.95 \cdot b} \tag{B.0.5}$$

provided that the spacing between the vias is sufficiently small.

APPENDIX C

HUMAN SUBJECTS CONSENT FORMS

CONSENT TO PARTICIPATE IN RESEARCH

You are asked to participate in a research study conducted by Xianyue Wu, from School of Electronic Electrical and Computer Engineering at the University of Birmingham. This study is being conducted as part of Xianyue Wu's PhD thesis. Your participation in this study is entirely voluntary. Please read the information below and ask questions about anything you do not understand, before deciding whether or not to participate.

- PURPOSE OF THE STUDY

  Investigation of radio channels for wireless body area networks

- PROCEDURES

  If you volunteer to participate in this study, you will be asked to do the following things:

  1. To put antennas on the parts of the body surface, i.e. head, arm, shoulder, wrist, chest, waist;

  2. Coaxial cables are used to connect the antennas to the Vector Network Analyser which generates radio signals at 60 GHz and 2.45 GHz;
  3. During the measurements, you will perform movements in an indoor/outdoor environments with antennas on the body.

- POTENTIAL RISKS AND CONTROL MEASURES

  There is no proved radiation harm on the body at these frequencies. The radiation power will be kept as low as possible in the measurements. And it will avoid antennas pointing to the eyes.

- PARTICIPATION AND WITHDRAWAL

  You can choose whether or not to be in this study. If you volunteer to be in this study, you may withdraw at any time without consequences of any kind or loss of benefits to which you are otherwise entitled. You may also refuse to answer any questions you do not want to answer. There is no penalty if you withdraw from the study.

I understand the procedures described above. My questions have been answered to my satisfaction, and I agree to participate in this study.

Name	Signature	Date
Yuriy I. Nechayev		01 October 2011
Xiao Li		01 October 2011

LIST OF REFERENCES

[1] Putting human bodies into the ‘internet of things’. `http://www.businessweek.com/articles/2013-06-04/putting-human-bodies-into-the-internet-of-things`. [Online; accessed 16-August-2013]. 1.1

[2] V. Oleshchuk and R. Fensli. Remote patient monitoring within a future 5G infrastructure. *Wireless Personal Communications*, 57(3):431–439, 2011. 1.1

[3] Wearable electronics - a $1.5 billion market in 2014. `http://www.eetimes.com/author.asp?section_id=36&doc_id=1286734`. [Online; accessed 13-August-2013]. 1.1

[4] Nike+. `http://nikeplus.nike.com/plus/`. [Online; accessed 13-August-2013]. 1.1

[5] Fitbit Inc. `http://www.fitbit.com/uk`. [Online; accessed 13-August-2013]. 1.1

[6] Best days for smartphone stocks have passed. `http://finance.yahoo.com/blogs/the-exchange/best-days-smartphone-stocks-passed-114506468.html`. [Online; accessed 13-August-2013]. 1.1

[7] Beyond Google Glass: Get ready for more wearable computers. `http://www.infoworld.com/t/consumer-electronics/beyond-google-glass-get-ready-more-wearable-computers-219679`. [Online; accessed 13-August-2013]. 1.1

[8] M. Patel and J. Wang. Applications, challenges, and prospective in emerging body area networking technologies. *IEEE Wireless Communications*, 17(1):80–88, 2010. 1.1

[9] proteus© digital health. `http://www.proteusdigitalhealth.com/technology/digital-health-feedback-system`. [Online; accessed 14-August-2013]. 1.1

[10] Metria^{TM} wearable sensor technology. `http://vancive.averydennison.com/en/home/solutions/metria.html`. [Online; accessed 14-August-2013]. 1.1

[11] C. Liolios, C. Doukas, G. Fourlas, and I. Maglogiannis. An overview of body sensor networks in enabling pervasive healthcare and assistive environments. In *Proceedings of the 3rd International Conference on PErvasive Technologies Related to Assistive Environments*, PETRA '10, pages 43:1–43:10, New York, NY, USA, 2010. ACM. 1.1

[12] M.A. Hanson, H.C. Powell, A.T. Barth, K. Ringgenberg, B.H. Calhoun, J.H. Aylor, and J. Lach. Body area sensor networks: Challenges and opportunities. *Computer*, 42(1):58–65, 2009. 1.1

[13] L. Wang, G.-Z. Yang, J. Huang, J. Zhang, L. Yu, Z. Nie, and D.R.S. Cumming. A wireless biomedical signal interface system-on-chip for body sensor networks. *IEEE Transactions on Biomedical Circuits and Systems*, 4(2):112–117, 2010. 1.1

[14] M.T. Lapinski. *A wearable, wireless sensor system for sports medicine*. PhD thesis, Massachusetts Institute of Technology, 2008.

[15] UCLA wireless health. `http://www.wirelesshealth.ucla.edu/`. [Online; accessed 18-September-2013].

[16] UVA center for wireless health. `http://wirelesshealth.virginia.edu/`. [Online; accessed 18-September-2013]. 1.1

[17] G.-Z. Yang. Sports body sensor networks. In *5th International Summer School and Symposium on Medical Devices and Biosensors, 2008. ISSS-MDBS 2008.*, pages 14–14, 2008. 1.1

[18] H. Ghasemzadeh, V. Loseu, E. Guenterberg, and R. Jafari. Sport training using body sensor networks: a statistical approach to measure wrist rotation for golf swing. In *Proceedings of the Fourth International Conference on Body Area Networks*, BodyNets '09, pages 2:1–2:8, ICST, Brussels, Belgium, Belgium, 2009. ICST (Institute for Computer Sciences, Social-Informatics and Telecommunications Engineering). 1.1

[19] M.A. Hanson and A.N. Miller. *Wireless Body Area Sensor Network Technology for Motion-Based Health Assessment*. BiblioBazaar, 2011. 1.2

[20] Sixthsense. `http://www.pranavmistry.com/projects/sixthsense/`. [Online; accessed 15-August-2013]. 1.2

[21] OmniTouch. `http://www.chrisharrison.net/index.php/Research/OmniTouch`. [Online; accessed 15-August-2013]. 1.2

[22] G.Z. Yang. *Body Sensor Networks*. Springer, 2007. 1.2

[23] A. Bharadwaj and J.K. Townsend. Evaluation of the covertness of time-hopping impulse radio using a multi-radiometer detection. In *IEEE Military Communications Conference, 2001. MILCOM 2001. Communications for Network-Centric Operations: Creating the Information Force*, volume 1, pages 128–134 vol.1, 2001. 2

[24] P.S. Hall and Y.Hao. *Antennas and Propagation for Body-Centric Wireless Communications*. Artech House antennas and propagation library. Artech House, 2012. 3

[25] L. Akhoondzadeh-asl, P.S. Hall, Y.I. Nechayev, and I. Khan. Depolarization in on-body communication channels at 2.45 GHz. *IEEE Transactions on Antennas and Propagation*, 61(2):882–889, 2013. 2.1, 2.3.1, 2.3.1

[26] L. Akhoondzadeh-asl, Y.I. Nechayev, P.S. Hall, and C.C. Constantinou. Parasitic array antenna with enhanced surface wave launching for on-body communications. *IEEE Transactions on Antennas and Propagation*, 61(4):1976–1985, 2013. 2.3.1, 2.4.1

[27] A. Alomainy, Y. Hao, A. Owadally, C.G. Parini, Y.I. Nechayev, C.C. Constantinou, and P.S. Hall. Statistical analysis and performance evaluation for on-body radio propagation with microstrip patch antennas. *IEEE Transactions on Antennas and Propagation*, 55(1):245–248, 2007. 2.3, 2.3.1, 2.3.1

[28] S.L. Cotton, G.A. Conway, and W.G. Scanlon. A time-domain approach to the analysis and modeling of on-body propagation characteristics using synchronized measurements at 2.45 GHz. *IEEE Transactions on Antennas and Propagation*, 57(4):943–955, 2009. 2.3, 2.3.1

[29] S.L. Cotton and W.G. Scanlon. Characterization and modeling of the indoor radio channel at 868 MHz for a mobile bodyworn wireless personal area network. *IEEE Antennas and Wireless Propagation Letters*, 6:51–55, 2007. 2.3.1

[30] S.L. Cotton and W.G. Scanlon. Channel characterization for single- and multiple-antenna wearable systems used for indoor body-to-body communications. *IEEE Transactions on Antennas and Propagation*, 57(4):980–990, 2009. 2.3.1, 2.3.1

[31] S.L. Cotton, W.G. Scanlon, and G.A. Conway. Autocorrelation of signal facing in wireless body area networks. In *2009 2nd IET Seminar on Antennas and Propagation for Body-Centric Wireless Communications*, pages 1–5, 2009.

[32] S.L. Cotton and W.G. Scanlon. An experimental investigation into the influence of user state and environment on fading characteristics in wireless body area networks at 2.45 GHz. *IEEE Transactions on Wireless Communications*, 8(1):6–12, 2009. 2.3.1

[33] S.L. Cotton, W.G. Scanlon, and J. Guy. The κ -μ distribution applied to the analysis of fading in body to body communication channels for fire and rescue personnel. *IEEE Antennas and Wireless Propagation Letters*, 7:66–69, 2008.

[34] A. Fort, C. Desset, P. Wambacq, and L.V. Biesen. Indoor body-area channel model for narrowband communications. *IET Microwaves, Antennas Propagation*, 1(6):1197–1203, 2007. 2.3.1, 2.3.1

[35] Z.H. Hu, Y.I. Nechayev, P.S. Hall, C.C. Constantinou, and Y. Hao. Measurements and statistical analysis of on-body channel fading at 2.45 GHz. *IEEE Antennas and Wireless Propagation Letters*, 6:612–615, 2007. 2.3.1, 2.3.1

[36] J. Zhang, D.B. Smith, L.W. Hanlen, D. Miniutti, D. Rodda, and B. Gilbert. Stability of narrowband dynamic body area channel. *IEEE Antennas and Wireless Propagation Letters*, 8:53–56, 2009.

[37] N. Katayama, K. Takizawa, T. Aoyagi, J.-I. Takada, H.-B. Li, and R. Kohno. Channel model on various frequency bands for wearable body area network. In *First International Symposium on Applied Sciences on Biomedical and Communication Technologies, 2008.*, pages 1–5, 2008. 2.3.1

[38] I. Khan, Y.I. Nechayev, and P.S. Hall. On-body diversity channel characterization. *IEEE Transactions on Antennas and Propagation*, 58(2):573–580, 2010. 2.3.1

[39] I. Khan, Y.I. Nechayev, and P.S. Hall. Second-order statistics of measured on-body diversity channels. *Microwave and Optical Technology Letters*, 51(10):2335–2337, 2009. 2.3.1

[40] Y.I. Nechayev, P.S. Hall, C. Constantinou, Y. Hao, A. Alomainy, R. Dubrovka, and C.G. Parini. On-body path gain variations with changing body posture and antenna position. In *2005 IEEE Antennas and Propagation Society International Symposium*, volume 1B, pages 731–734 vol. 1B, 2005. 2.3.1, 2.3.1

[41] Y.I. Nechayev, Z.H. Hu, and P.S. Hall. Short-term and long-term fading of on-body transmission channels at 2.45 GHz. In *2009 LoughboroughAntennas Propagation Conference*, pages 657–660, 2009. 2.3.1

[42] Y.I. Nechayev, P.S. Hall, and Z.H. Hu. Characterisation of narrowband communication channels on the human body at 2.45 GHz. *IET Microwaves, Antennas Propagation*, 4(6):722–732, 2010. 2.1, 2.3.1, 2.4.1

[43] D.B. Smith, J. Zhang, L.W. Hanlen, D. Miniutti, D. Rodda, and B. Gilbert. Temporal correlation of dynamic on-body area radio channel. *Electronics Letters*, 45(24):1212–1213, 2009.

[44] K. Tai, H. Harada, and R. Kohno. Channel modeling and signaling of medical implanted communication systems and a step to medical ICT. In *16th IST Mobile and Wireless Communications Summit, 2007.*, pages 1–5, 2007.

[45] K. Takizawa, T. Aoyagi, K. Hamaguchi, and R. Kohno. Performance evaluation of wireless communications through capsule endoscope. In *Annual International Conference of the IEEE Engineering in Medicine and Biology Society, 2009. EMBC 2009.*, pages 6897–6900, 2009.

[46] B. Zhen, M. Kim, J. i. Takada, and R. Kohno. Characterization and modeling of dynamic on-body propagation at 4.5 GHz. *IEEE Antennas and Wireless Propagation Letters*, 8:1263–1267, 2009. 2.3.1, 2.3.1

[47] P.S. Hall, Y. Hao, Y.I. Nechayev, A. Alomainy, C.C. Constantinou, C. Parini, M.R. Kamarudin, T.Z. Salim, D.T.M. Hee, R. Dubrovka, A.S. Owadally, W. Song, A. Serra, P. Nepa, M. Gallo, and M. Bozzetti. Antennas and propagation for on-body communication systems. *IEEE Antennas and Propagation Magazine*, 49(3):41–58, 2007. 2.3.1, 2.4.1, 8.1

[48] A. Alomainy, Y. Hao, and D.M. Davenport. Parametric study of wearable antennas with varying distances from the body and different on-body positions. In *IET Seminar on Antennas and Propagation for Body-Centric Wireless Communications*, pages 84–89, 2007. 2.4.1

[49] M. Klemm, I.Z. Kovcs, G.F. Pedersen, and G. Troster. Novel small-size directional antenna for UWB WBAN/WPAN applications. *IEEE Transactions on Antennas and Propagation*, 53(12):3884–3896, 2005. 2.4.1

[50] T. See and Z.-N. Chen. Experimental characterization of UWB antennas for on-body communications. *IEEE Transactions on Antennas and Propagation*, 57(4):866–874, 2009. 2.1, 2.3.1, 2.3.1, 2.4.1

[51] A. Alomainy, Y. Hao, C.G. Parini, and P.S. Hall. Comparison between two different antennas for UWB on-body propagation measurements. *IEEE Antennas and Wireless Propagation Letters*, 4:31–34, 2005.

[52] N. Chahat, M. Zhadobov, R. Sauleau, and K. Ito. A compact UWB antenna for on-body applications. *IEEE Transactions on Antennas and Propagation*, 59(4):1123–1131, 2011. 2.4.1

[53] A. Alomainy, A. Sani, A. Rahman, J.G. Santas, and Y. Hao. Transient characteristics of wearable antennas and radio propagation channels for ultrawideband body-centric wireless communications. *IEEE Transactions on Antennas and Propagation*, 57(4):875–884, 2009. 2.4.1

[54] Q.H. Abbasi, A. Sani, A. Alomainy, and Y. Hao. Arm movements effect on ultra wideband on-body propagation channels and radio systems. In *Loughborough Antennas Propagation Conference*, pages 261–264, 2009. 2.3.1, 2.3.1

[55] A. Alomainy, Y. Hao, X. Hu, C.G. Parini, and P.S. Hall. UWB on-body radio propagation and system modelling for wireless body-centric networks. *IEE Proceedings Communications*, 153(1):107–114, 2006. 2.3.1

[56] A. Alomainy, A. Sani, A. Rahman, J.G. Santas, and Y. Hao. Transient characteristics of wearable antennas and radio propagation channels for ultrawideband body-centric wireless communications. *IEEE Transactions on Antennas and Propagation*, 57(4):875–884, 2009. 2.3.1

[57] A. Fort, J. Ryckaert, C. Desset, P. De Doncker, P. Wambacq, and L. Van Biesen. Ultra-wideband channel model for communication around the human body. *IEEE Journal on Selected Areas in Communications*, 24(4):927–933, 2006. 2.3.1

[58] A.A. Goulianos, T. Brown, and S. Stavrou. Power delay profile modelling of the ultra wideband off-body propagation channel. *IET Microwaves, Antennas Propagation*, 4(1):62–71, 2010. 2.3.1, 2.5

[59] A.A. Goulianos, T. Brown, B.G. Evans, and S. Stavrou. Wideband power modeling and time dispersion analysis for UWB indoor off-body communications. *IEEE Transactions on Antennas and Propagation*, 57(7):2162–2171, 2009. 2.3.1, 2.5

[60] A.A. Goulianos and S. Stavrou. UWB path arrival times in body area networks. *IEEE Antennas and Wireless Propagation Letters*, 6:223–226, 2007. 2.3.1

[61] A.F. Molisch, D. Cassioli, C.-C. Chong, S. Emami, A. Fort, B. Kannan, J. Karedal, J. Kunisch, H.G. Schantz, K. Siwiak, and M.Z. Win. A comprehensive standardized model for ultrawideband propagation channels. *IEEE Transactions on Antennas and Propagation*, 54(11):3151–3166, 2006. 2.3.1

[62] A. Sani, A. Alomainy, G. Palikaras, Y. Nechayev, Y. Hao, C. Parini, and P.S. Hall. Experimental characterization of UWB on-body radio channel in indoor environment considering different antennas. *IEEE Transactions on Antennas and Propagation*, 58(1):238–241, 2010. 2.3.1

[63] S. Van Roy, C. Oestges, F. Horlin, and P. De Doncker. On-body propagation velocity estimation using ultra-wideband frequency-domain spatial correlation analyses. *Electronics Letters*, 43(25):1405–1406, 2007.

[64] S. Van Roy, C. Oestges, F. Horlin, and P. De Doncker. A comprehensive channel model for UWB multisensor multiantenna body area networks. *IEEE Transactions on Antennas and Propagation*, 58(1):163–170, 2010. 2.3.1

[65] T. Zasowski, G. Meyer, F. Althaus, and A. Wittneben. UWB signal propagation at the human head. *IEEE Transactions on Microwave Theory and Techniques*, 54(4):1836–1845, 2006.

[66] T. Zasowski and A. Wittneben. Performance of UWB receivers with partial CSI using a simple body area network channel model. *IEEE Journal on Selected Areas in Communications*, 27(1):17–26, 2009. 2.1, 2.3.1, 2.3.1

[67] Two-port Network. `http://en.wikipedia.org/wiki/Two-port_network`. [Online; accessed 20-December-2013]. 2.2.3

[68] J. Kim and Y. Rahmat-Samii. Implanted antennas inside a human body: simulations, designs, and characterizations. *IEEE Transactions on Microwave Theory and Techniques*, 52(8):1934–1943, 2004. 2.3

[69] J. Kim and Y. Rahmat-Samii. Planar inverted-F antennas on implantable medical devices: Meandered type versus spiral type. *Microwave and Optical Technology Letters*, 48(3):567–572, 2006.

[70] J. Kim and Y. Rahmat-Samii. Low-profile antennas for implantable medical devices: optimized designs for antennas/human interactions. In *IEEE Antennas and Propagation Society International Symposium, 2004.*, volume 2, pages 1331–1334 Vol.2, 2004.

[71] R. Warty, M.-R. Tofighi, U. Kawoos, and A. Rosen. Characterization of implantable antennas for intracranial pressure monitoring: Reflection by and transmission through a scalp phantom. *IEEE Transactions on Microwave Theory and Techniques*, 56(10):2366–2376, 2008.

[72] T. Dissanayake, K.P. Esselle, and M.R. Yuce. Dielectric loaded impedance matching for wideband implanted antennas. *IEEE Transactions on Microwave Theory and Techniques*, 57(10):2480–2487, 2009. 2.3

[73] S.L. Cotton, A. McKernan, and W.G. Scanlon. Received signal characteristics of outdoor body-to-body communications channels at 2.45 GHz. In *Loughborough Antennas and Propagation Conference (LAPC)*, pages 1–4, 2011. 2.3.1

[74] C. Icheln, J. Ollikainen, and P. Vainikainen. Reducing the influence of feed cables on small antenna measurements. *Electronics Letters*, 35(15):1212–1214, 1999. 2.3.1

[75] P.J. Massey and K.R. Boyle. Controlling the effects of feed cable in small antenna measurements. In *Twelfth International Conference on Antennas and Propagation, 2003. (ICAP 2003).*, volume 2, pages 561–564 vol.2, 2003.

[76] I. Kovacs, G.F. Pedersen, P. Eggers, and K. Olesen. Ultra wideband radio propagation in body area network scenarios. In *2004 IEEE Eighth International Symposium on Spread Spectrum Techniques and Applications*, pages 102–106, 2004. 2.3.1

[77] P.A. Catherwood and W.G. Scanlon. Measurement errors introduced by the use of co-axial cabling in the assessment of wearable antenna performance in off-body channels. In *Proceedings of the 5th European Conference on Antennas and Propagation (EUCAP)*, pages 3787–3791, 2011. 2.3.1

[78] S. Dusara. *Radio-over-fibre systems for body-centric communication measurements.* PhD thesis, University of Birmingham, 2011. 2.3.1

[79] N.E. Roberts, S. Oh, and D.D. Wentzloff. Exploiting channel periodicity in body sensor networks. *IEEE Journal on Emerging and Selected Topics in Circuits and Systems*, 2(1):4–13, 2012. 2.3.1

[80] A. Lea, P. Hui, J. Ollikainen, and R.G. Vaughan. Propagation between on-body antennas. *IEEE Transactions on Antennas and Propagation*, 57(11):3619–3627, 2009. 2.3.1

[81] M.U. Rehman, Y. Gao, X. Chen, C.G. Parini, Z. Ying, T. Bolin, and J. W. Zweers. On-body bluetooth link budget: Effects of surrounding objects and role of surface waves. In *Loughborough Antennas and Propagation Conference, 2008.*, pages 97–100, 2008. 2.3.1, 2.4

[82] J. Ryckaert, P. De Doncker, R. Meys, A. de Le Hoye, and S. Donnay. Channel model for wireless communication around human body. *Electronics Letters*, 40(9):543–544, 2004. 2.3.1, 2.3.2

[83] R. Paknys and D.R. Jackson. The relation between creeping waves, leaky waves, and surface waves. *IEEE Transactions on Antennas and Propagation*, 53(3):898–907, 2005. 2.3.1

[84] Lida Akhoondzadehasl. *Polarization behaviour of on-body communication channels at 2.45 GHz.* PhD thesis, University of Birmingham, July 2011. 2.3.1

[85] H. Nikookar and R. Prasad. *Introduction to Ultra Wideband for Wireless Communications.* Signals and Communication Technology Series. Springer London, Limited, 2008. 2.3.1

[86] Y. P. Zhang and Q. Li. Performance of UWB impulse radio with planar monopoles over on-human-body propagation channel for wireless body area networks. *IEEE Transactions on Antennas and Propagation*, 55(10):2907–2914, 2007. 2.3.1

[87] T. Aoyagi, K. Takizawa, T. Kobayashi, J.-I. Takada, and R. Kohno. Development of a WBAN channel model for capsule endoscopy. In *IEEE Antennas and Propagation Society International Symposium*, pages 1–4, 2009. 2.3.2

[88] J. Bringuier and R. Mittra. A new hybrid technique for handling fine features in FDTD and its application to body-centric communications. In *Asia Pacific Microwave Conference*, pages 2204–2207, 2009. 2.3.2

[89] J. Bringuier, R. Mittra, and N. Farahat. A novel approach to constructing the green's function for layered media and its application to MMIC, RFIC, and EMC problems. In *IEEE Antennas and Propagation Society International Symposium*, pages 1853–1856, 2007. 2.3.2

[90] J.N. Bringuier, R. Mittra, and J. Wiart. Efficient modeling of body area networks using the parallized FDTD, it's serial parallel extension and the time domain Green's function method. In *The Second European Conference on Antennas and Propagation*, pages 1–5, 2007. 2.3.2

[91] R. Dubrovka, C. Parini, Y. Hao, A. Alomainy, P. Hall, C. Constantinou, and Y. Nechayev. On-body propagation loss estimation using method of equivalent sources. *Electronics Letters*, 42(9):506–508, 2006. 2.3.2

[92] M. Gallo, P.S. Hall, Y.I. Nechayev, and M. Bozzetti. Use of animation software in simulation of on-body communications channels at 2.45 GHz. *IEEE Antennas and Wireless Propagation Letters*, 7:321–324, 2008. 2.3.2

[93] M. Gallo, P.S. Hall, Q. Bai, Y.I. Nechayev, C.C. Constantinou, and M. Bozzetti. Simulation and measurement of dynamic on-body communication channels. *IEEE Transactions on Antennas and Propagation*, 59(2):623–630, 2011. 2.3.2

[94] A. Khaleghi and I. Balasingham. Non-line-of-sight on-body ultra wideband (1-6 GHz) channel characterisation using different antenna polarisations. *IET Microwaves, Antennas Propagation*, 3(7):1019–1027, 2009. 2.3.2

[95] A. Khaleghi and I. Balasingham. Improving in-body ultra wideband communication using near-field coupling of the implanted antenna. *Microwave and Optical Technology Letters*, 51(3):585–589, 2009.

[96] Q. Wang, T. Tayamachi, I. Kimura, and J. Wang. An on-body channel model for UWB body area communications for various postures. *IEEE Transactions on Antennas and Propagation*, 57(4):991–998, 2009. 2.3.2

[97] A. Sani, A. Alomainy, and Y. Hao. Numerical characterization and link budget evaluation of wireless implants considering different digital human phantoms. *IEEE Transactions on Microwave Theory and Techniques*, 57(10):2605–2613, 2009.

[98] A. Sani, Y. Zhao, and Y. Hao. Analysis of on-body propagation channel using a hybrid technique combining the equivalence principle and FDTD. In *International Workshop on Antenna Technology: Small Antennas and Novel Metamaterials, 2008.*, pages 502–505, 2008. 2.3.2

[99] W.G. Scanlon, B. Burns, and N.E. Evans. Radiowave propagation from a tissue-implanted source at 418 MHz and 916.5 MHz. *IEEE Transactions on Biomedical Engineering*, 47(4):527–534, 2000.

[100] G. Koutitas. Multiple human effects in body area networks. *IEEE Antennas and Wireless Propagation Letters*, 9:938–941, 2010. 2.3.2

[101] K. I. Ziri-Castro, W.G. Scanlon, and N. E.Evans. Indoor radio channel characterization and modeling for a 5.2-GHz bodyworn receiver. *IEEE Antennas and Wireless Propagation Letters*, 3(1):219–222, 2004. 2.3.2

[102] H. Terchoune, D. Lautru, A. Gati, A. Carrasco, M.F. Wong, J. Wiart, and V.F. Hanna. On-body radio channel modeling for different human body models using FDTD techniques. *Microwave and Optical Technology Letters*, 51(10):2498–2501, 2009. 2.3.2

[103] T. Tayamachi, Q. Wang, and J. Wang. Transmission characteristic analysis for UWB body area communications. In *International Symposium on Electromagnetic Compatibility, 2007. EMC 2007.*, pages 75–78, 2007. 2.3.2

[104] J. Wang and Q. Wang. Channel modeling and BER performance of an implant UWB body area link. In *2nd International Symposium on Applied Sciences in Biomedical and Communication Technologies*, pages 1–4, 2009.

[105] Q. Wang and J. Wang. Performance of on-body chest-to-waist UWB communication link. *IEEE Microwave and Wireless Components Letters*, 19(2):119–121, 2009. 2.3.2

[106] W.-B. Yang, K. Sayrafian-Pour, J. Hagedorn, J. Terrill, and K.Y. Yazdandoost. Simulation study of body surface RF propagation for UWB wearable medical sensors. In *2nd International Symposium on Applied Sciences in Biomedical and Communication Technologies, 2009.*, pages 1–6, 2009. 2.3.2

[107] Y. Zhao, Y. Hao, A. Alomainy, and C. Parini. UWB on-body radio channel modeling using ray theory and subband FDTD method. *IEEE Transactions on Microwave Theory and Techniques*, 54(4):1827–1835, 2006. 2.3.2

[108] Y. Zhao, A. Sani, Y. Hao, S.-L. Lee, and G.-Z. Yang. A subject-specific radio propagation study in wireless body area networks. In *Loughborough Antennas Propagation Conference, 2009.*, pages 80–83, 2009. 2.3.2

[109] Y. Zhao, A. Sani, Y. Hao, S.-L. Lee, and G.-Z. Yang. A simulation environment for subject-specific radio channel modeling in wireless body sensor networks. In *Sixth International Workshop on Wearable and Implantable Body Sensor Networks, 2009. BSN 2009.*, pages 23–28, 2009. 2.3.2

[110] CST Microwave Studio©. `http://www.cst.com/Content/Products/MWS/Overview.aspx`. [Online; accessed 13-August-2013]. 2.3.2

[111] XFdtd© EM Simulation Software. `http://www.remcom.com/xf7`. [Online; accessed 13-August-2013]. 2.3.2

[112] A. Brizzi, A. Pellegrini, L. Zhang, and Y. Hao. Statistical path-loss model for on-body communications at 94 GHz. *Antennas and Propagation, IEEE Transactions on*, PP(99):1–1, 2013. 2.3.2

[113] ©Vicon Motion Systems Ltd. `http://www.vicon.com/`. [Online; accessed 13-December-2013]. 2.3.3

[114] S. Swaisaenyakron, P.R. Young, and J.C. Batchelor. Animated human walking movement for body worn antenna study. In *2011 Loughborough Antennas and Propagation Conference (LAPC)*, pages 1–4, 2011. 2.3.3, 2.3

[115] Y. Nechayev, C. Constantinou, S. Swaisaenyakorn, O. Rakibet, J. Batchelor, P.S. Hall, C. Parini, and J. Hunt. Use of motion capture for path gain modelling of millimetre-wave on-body communication links. In *2012 International Symposium on Antennas and Propagation (ISAP)*, pages 987–990, 2012. 2.3.3, 5.2

[116] G.A. Conway and W.G. Scanlon. Antennas for over-body-surface communication at 2.45 GHz. *IEEE Transactions on Antennas and Propagation*, 57(4):844–855, 2009. 2.4.1

[117] A.R. Chandran, G.A. Conway, and W.G. Scanlon. Pattern switching compact patch antenna for on-body and off-body communications at 2.45 GHz. In *3rd European Conference on Antennas and Propagation*, pages 2055–2057, 2009. 2.4.1

[118] D. Psychoudakis and J.L. Volakis. Conformal asymmetric meandered flare (AMF) antenna for body-worn applications. *IEEE Antennas and Wireless Propagation Letters*, 8:931–934, 2009. 2.4.1

[119] Y.-J. Ren, C.-P. Lai, P.-H. Chen, and R.M. Narayanan. Compact ultrawideband UHF array antenna for through-wall radar applications. *IEEE Antennas and Wireless Propagation Letters*, 8:1302–1305, 2009. 2.4.1

[120] M.R. Kamarudin and P.S. Hall. Switched beam antenna array with parasitic elements. *Progress In Electromagnetics Research B*, 13:187–201, 2009. 2.4.1

[121] H.G. Schantz and L. Fullerton. The diamond dipole: a Gaussian impulse antenna. In *IEEE Antennas and Propagation Society International Symposium, 2001.*, volume 4, pages 100–103 vol.4, 2001. 2.4.1

[122] X. Han, L. Juan, C. Cui, and Y. Lin. UWB dual-polarized Vivaldi antenna with high gain. In *2012 International Conference on Microwave and Millimeter Wave Technology (ICMMT)*, volume 3, pages 1–4, 2012. 2.4.1

[123] L. Abdelghani, T.A. Denidni, and M. Nedil. Design of a new ultra-wideband 4 × 4 Butler matrix for beamforming antenna applications. In *IEEE Antennas and Propagation Society International Symposium (APSURSI)*, pages 1–2, 2012. 2.4.1

[124] C. Hertleer, A. Tronquo, H. Rogier, L. Vallozzi, and L. Van Langenhove. Aperture-coupled patch antenna for integration into wearable textile systems. *IEEE Antennas and Wireless Propagation Letters*, 6:392–395, 2007. 2.4.2

[125] I. Locher, M. Klemm, T. Kirstein, and G. Troster. Design and characterization of purely textile patch antennas. *IEEE Transactions on Advanced Packaging*, 29(4):777–788, 2006. 2.4.2

[126] D.L. Paul, H. Giddens, M.G. Paterson, G.S. Hilton, and J.P. McGeehan. Impact of body and clothing on a wearable textile dual band antenna at digital television and wireless communications bands. *IEEE Transactions on Antennas and Propagation*, 61(4):2188–2194, 2013.

[127] M.L. Scarpello, I. Kazani, C. Hertleer, H. Rogier, and D. Vande Ginste. Stability and efficiency of screen-printed wearable and washable antennas. *IEEE Antennas and Wireless Propagation Letters*, 11:838–841, 2012. 2.4.2

[128] R. Moro, S. Agneessens, H. Rogier, and M. Bozzi. Wearable textile antenna in substrate integrated waveguide technology. *Electronics Letters*, 48(16):985–987, 2012. 2.4.2

[129] A. Chauraya, W.G. Whittow, J.C. Vardaxoglou, Y. Li, R. Torah, K. Yang, S. Beeby, and J. Tudor. Inkjet printed dipole antennas on textiles for wearable communications. *IET Microwaves, Antennas Propagation*, 7(9):–, 2013. 2.4.2

[130] Q. Bai and R. Langley. Crumpling of PIFA textile antenna. *IEEE Transactions on Antennas and Propagation*, 60(1):63–70, 2012. 2.4.2

[131] T. Maleszka and P. Kabacik. Bandwidth properties of embroidered loop antenna for wearable applications. In *2010 European Wireless Technology Conference (EuWIT)*, pages 89–92, 2010. 2.4.2

[132] J.A. Dobbins, A.W. Chu, P.W. Fink, T.F. Kennedy, G.Y. Lin, M.A. Khayat, and R.C. Scully. Fabric equiangular spiral antenna. In *IEEE Antennas and Propagation Society International Symposium 2006*, pages 2113–2116, 2006. 2.4.2

[133] S. Zhu and R. Langley. Dual-band wearable textile antenna on an EBG substrate. *IEEE Transactions on Antennas and Propagation*, 57(4):926–935, 2009. 2.4.2

[134] L.W. Hanlen, D. Miniutti, D. Rodda, and B. Gilbert. Interference in body area networks: Distance does not dominate. In *2009 IEEE 20th International Symposium on Personal, Indoor and Mobile Radio Communications*, pages 281–285, 2009. 2.5, 2.5.1

[135] A. Yener, R.D. Yates, and S. Ulukus. Interference management for CDMA systems through power control, multiuser detection, and beamforming. *IEEE Transactions on Communications*, 49(7):1227–1239, 2001. 2.5

[136] P. Van Torre, L. Vallozzi, C. Hertleer, H. Rogier, M. Moeneclaey, and J. Verhaevert. Indoor off-body wireless MIMO communication with dual polarized textile antennas. *IEEE Transactions on Antennas and Propagation*, 59(2):631–642, 2011. 2.5

[137] P. Van Torre, L. Vallozzi, L. Jacobs, H. Rogier, M. Moeneclaey, and J. Verhaevert. Characterization of measured indoor off-body MIMO channels with correlated fading, correlated shadowing and constant path loss. *IEEE Transactions on Wireless Communications*, 11(2):712–721, 2012.

[138] S.L. Cotton and W.G. Scanlon. Measurements, modeling and simulation of the off-body radio channel for the implementation of bodyworn antenna diversity at 868 MHz. *IEEE Transactions on Antennas and Propagation*, 57(12):3951–3961, 2009. 2.5

[139] M.M. Khan, Q.H. Abbasi, A. Alomainy, Y. Hao, and C. Parini. Experimental characterisation of ultra-wideband off-body radio channels considering antenna effects. *IET Microwaves, Antennas Propagation*, 7(5):–, 2013. 2.5

[140] L.W. Hanlen, D. Miniutti, D. Smith, D. Rodda, and B. Gilbert. Co-channel interference in body area networks with indoor measurements at 2.4ÂăGHz: Distance-to-interferer is a poor estimate of received interference power. *International Journal of Wireless Information Networks*, 17(3-4):113–125, 2010. 2.5.1

[141] A. Zhang, L.W. Hanlen, D. Miniutti, D. Rodda, and B. Gilbert. Interference in body area networks: Are signal-links and interference-links independent? In *2009 IEEE 20th International Symposium on Personal, Indoor and Mobile Radio Communications*, pages 456–460, 2009. 2.5.1

[142] I. Khan, Y.I. Nechayev, K. Ghanem, and P.S. Hall. BAN-BAN interference rejection with multiple antennas at the receiver. *IEEE Transactions on Antennas and Propagation*, 58(3):927–934, 2010. 2.5.1

[143] J. Hauer and D. Willkomm. An empirical study of urban 2.4 GHz RF noise from the perspective of a body sensor network. In *Wearable and Implantable Body Sensor Networks (BSN), 2012 Ninth International Conference on*, pages 73–78, 2012. 2.5.1

[144] H. Xiong, W. Zhang, Z. Du, B. He, and D. Yuan. Front-end narrowband interference mitigation for DS-UWB receiver. *IEEE Transactions on Wireless Communications*, PP(99):1–10, 2013. 2.5.2

[145] X. Cheng and Y. Guan. Narrow-band interference suppression in impulse radio ultra-wideband systems. *IEEE Transactions on Vehicular Technology*, PP(99):1–1, 2013. 2.5.2

[146] Report: Ultrawideband dies by 2013. `http://www.eetimes.com/document.asp?doc_id=1170933`. [Online; accessed 02-September-2013]. 2.6

[147] S.K.S. Gupta, T. Mukherjee, and K.K. Venkatasubramanian. *Body Area Networks: Safety, Security, and Sustainability.* Cambridge University Press, 2013. 3.1

[148] P. Smulders. Exploiting the 60 GHz band for local wireless multimedia access: prospects and future directions. *IEEE Communications Magazine*, 40(1):140–147, 2002. 3.1, 3.2

[149] N. Guo, R.C. Qiu, S. Mo, and K. Takahashi. 60-GHz millimeter-wave radio: Principle, technology, and new results. *EURASIP Journal on Wireless Communications and Networking*, 2007(1):48–48, 2007. 3.1

[150] IEEE standard 802.15.3c-2009. `http://standards.ieee.org/findstds/standard/802.15.3c-2009.html`. [Online; accessed 17-August-2013]. 3.1

[151] IEEE standard 802.11ad. `http://en.wikipedia.org/wiki/Wireless_Gigabit_Alliance`. [Online; accessed 17-August-2013]. 3.1, 3.3

[152] H. Xu, V. Kukshya, and T.S. Rappaport. Spatial and temporal characteristics of 60-GHz indoor channels. *IEEE Journal on Selected Areas in Communications*, 20(3):620–630, 2002. 3.1

[153] R.C. Daniels, J.N. Murdock, T.S. Rappaport, and R.W. Heath. 60 GHz wireless: Up close and personal. *IEEE Microwave Magazine*, 11(7):44–50, 2010. 3.2

[154] T. Manabe, Y. Miura, and T. Ihara. Effects of antenna directivity and polarization on indoor multipath propagation characteristics at 60 GHz. *IEEE Journal on Selected Areas in Communications*, 14(3):441–448, 1996. 3.2

[155] H. Yang, M. Herben, and P. Smulders. Impact of antenna pattern and reflective environment on 60 GHz indoor radio channel characteristics. *IEEE Antennas and Wireless Propagation Letters*, 4:300–303, 2005. 3.2

[156] S. Collonge, G. Zaharia, and G.E. Zein. Influence of the human activity on wideband characteristics of the 60 GHz indoor radio channel. *IEEE Transactions on Wireless Communications*, 3(6):2396–2406, 2004. 3.2

[157] P. Smulders and L.M. Correia. Characterisation of propagation in 60 GHz radio channels. *Electronics Communication Engineering Journal*, 9(2):73–80, 1997. 3.3

[158] Millimeter waves may be the future of 5G phones. `http://spectrum.ieee.org/telecom/wireless/millimeter-waves-may-be-the-future-of-5g-phones`. [Online; accessed 18-August-2013]. 3.3

[159] K.C. Huang and D.J. Edwards. *Millimetre Wave Antennas for Gigabit Wireless Communications: A Practical Guide to Design and Analysis in a System Context.* Wiley, 2008. 3.4

[160] C. Gustafson and F. Tufvesson. Characterization of 60 GHz shadowing by human bodies and simple phantoms. In *2012 6th European Conference on Antennas and Propagation (EUCAP)*, pages 473–477, 2012. 3.4

[161] H. Chu, Y.-X. Guo, and Z. Wang. 60-GHz LTCC wideband vertical off-center dipole antenna and arrays. *IEEE Transactions on Antennas and Propagation*, 61(1):153–161, 2013. 3.4

[162] C. Karnfelt, P. Hallbjorner, H. Zirath, and A. Alping. High gain active microstrip antenna for 60-GHz WLAN/WPAN applications. *IEEE Transactions on Microwave Theory and Techniques*, 54(6):2593–2603, 2006. 3.4

[163] L. Pazin and Y. Leviatan. A compact 60-GHz tapered slot antenna printed on LCP substrate for WPAN applications. *IEEE Antennas and Wireless Propagation Letters*, 9:272–275, 2010. 3.4

[164] M. Sun, Y.-P. Zhang, K.M. Chua, L.L. Wai, D. Liu, and B.P. Gaucher. Integration of Yagi antenna in LTCC package for differential 60-GHz radio. *IEEE Transactions on Antennas and Propagation*, 56(8):2780–2783, 2008. 3.4

[165] W. Menzel, D. Pilz, and M. Al-Tikriti. 60 GHz triple folded reflector antenna. *Electronics Letters*, 38(19):1075–1076, 2002. 3.4

[166] B. Pan, Y. Li, G.E. Ponchak, J. Papapolymerou, and M.M. Tentzeris. A 60-GHz CPW-fed high-gain and broadband integrated horn antenna. *Antennas and Propagation, IEEE Transactions on*, 57(4):1050–1056, 2009. 3.4

[167] Q. Lai, C. Fumeaux, W. Hong, and R. Vahldieck. 60 GHz aperture-coupled dielectric resonator antennas fed by a half-mode substrate integrated waveguide. *IEEE Transactions on Antennas and Propagation*, 58(6):1856–1864, 2010. 3.4

[168] X. Wu, G.V. Eleftheriades, and T.E. van Deventer-Perkins. Design and characterization of single- and multiple-beam mm-wave circularly polarized substrate lens antennas for wireless communications. *IEEE Transactions on Microwave Theory and Techniques*, 49(3):431–441, 2001. 3.4

[169] W. Lee, J. Kim, C.-S. Cho, and Y.J. Yoon. Beamforming lens antenna on a high resistivity silicon wafer for 60 GHz WPAN. *IEEE Transactions on Antennas and Propagation*, 58(3):706–713, 2010. 3.4

[170] P.S. Hall and S.J. Vetterlein. Review of radio frequency beamforming techniques for scanned and multiple beam antennas. *IEE Proceedings H Microwaves, Antennas and Propagation*, 137(5):293–303, 1990. 3.4

[171] G.H. Zhai, W. Hong, K. Wu, J. X. Chen, P. Chen, J. Wei, and H.-J. Tang. Folded half mode substrate integrated waveguide 3 dB coupler. *IEEE Microwave and Wireless Components Letters*, 18(8):512–514, 2008. 3.4

[172] Y.-J. Cheng, P. Chen, W. Hong, T. Djerafi, and K. Wu. Substrate-integrated-waveguide beamforming networks and multibeam antenna arrays for low-cost satellite and mobile systems. *IEEE Antennas and Propagation Magazine*, 53(6):18–30, 2011.

[173] Y.J. Cheng, W. Hong, and K. Wu. Millimeter-wave half mode substrate integrated waveguide frequency scanning antenna with quadri-polarization. *IEEE Transactions on Antennas and Propagation*, 58(6):1848–1855, 2010.

[174] W. Shen, W.-Y. Yin, and X.-W. Sun. Miniaturized dual-band substrate integrated waveguide filter with controllable bandwidths. *IEEE Microwave and Wireless Components Letters*, 21(8):418–420, 2011.

[175] C.-J. Chen and T.-H. Chu. Design of a 60-GHz substrate integrated waveguide butler matrix – a systematic approach. *IEEE Transactions on Microwave Theory and Techniques*, 58(7):1724–1733, 2010. 3.4

[176] A.E.I. Lamminen, J. Saily, and A.R. Vimpari. 60-GHz patch antennas and arrays on LTCC with embedded-cavity substrates. *IEEE Transactions on Antennas and Propagation*, 56(9):2865–2874, 2008. 3.4

[177] R. Li, G. DeJean, M. Maeng, K. Lim, S. Pinel, M.M. Tentzeris, and J. Laskar. Design of compact stacked-patch antennas in LTCC multilayer packaging modules for wireless applications. *IEEE Transactions on Advanced Packaging*, 27(4):581–589, 2004.

[178] I.K. Kim, N. Kidera, S. Pinel, J. Papapolymerou, J. Laskar, J.-G. Yook, and M.M. Tentzeris. Linear tapered cavity-backed slot antenna for millimeter-wave LTCC modules. *IEEE Antennas and Wireless Propagation Letters*, 5(1):175–178, 2006.

[179] E. Cohen, M. Ruberto, M. Cohen, O. Degani, S. Ravid, and D. Ritter. A CMOS bidirectional 32-element phased-array transceiver at 60 GHz with LTCC antenna. *IEEE Transactions on Microwave Theory and Techniques*, 61(3):1359–1375, 2013.

[180] C. Liu, Y.-X. Guo, X. Bao, and S.-Q. Xiao. 60-GHz LTCC integrated circularly polarized helical antenna array. *IEEE Transactions on Antennas and Propagation*, 60(3):1329–1335, 2012. 3.4

[181] J. Xu, Z.N. Chen, X. Qing, and W. Hong. 140-GHz planar broadband LTCC SIW slot antenna array. *IEEE Transactions on Antennas and Propagation*, 60(6):3025–3028, 2012. 3.4

[182] Millitech© Orthomode Transducers. `http://www.millitech.com/pdfs/specsheets/IS000023-OMT.pdf`. [Online; accessed 24-September-2013]. 5.1

[183] Millitech© Scalar and Conical Horn Antennas. `http://www.millitech.com/pdfs/specsheets/IS000018-SFH-CHA.pdf`. [Online; accessed 24-September-2013]. 5.2

[184] Y.I. Nechayev, X.Y. Wu, C.C. Constantinou, and P.S. Hall. Millimetre-wave path-loss variability between two body-mounted monopole antennas. *IET Microwaves, Antennas Propagation*, 7(1):1–7, 2013. 1

[185] I. Khan. *Diversity and MIMO for body-centric wireless communication channels.* PhD thesis, University of Birmingham, December 2009. 5.3

[186] S.L. Cotton, W.G. Scanlon, and B.K. Madahar. Millimeter-wave soldier-to-soldier communications for covert battlefield operations. *IEEE Communications Magazine*, 47(10):72–81, 2009. 7.1

[187] S. Alipour, F. Parvaresh, H. Ghajari, and F.K. Donald. Propagation characteristics for a 60 GHz wireless body area network (WBAN). In *MILITARY COMMUNICATIONS CONFERENCE, 2010 - MILCOM 2010*, pages 719–723, 2010. 7.1

[188] J.V. DiFranco, R. Difranco, and W.L. Rubin. *Radar Detection.* SciTech radar and defense series. SciTech Publishing, Incorporated, 2004. 7.2

[189] M.I. Skolnik. *Introduction to radar systems.* McGraw-Hill, 1962.

[190] M.I. Skolnik. *Radar Handbook.* Electronic engineering series. McGraw-Hill, 1990. 7.2

[191] M.A. Richards. *Fundamentals of Radar Signal Processing.* Professional Engineering. McGraw-Hill, 2005. 7.2

[192] D.K. Barton. *Modern radar system analysis.* Artech House Radar Library. Artech House, 1988. 7.1

[193] Electronic warfare support measures. `http://en.wikipedia.org/wiki/Electronic_warfare_support_measures`. [Online; accessed 21-July-2013]. 7.3

[194] G.-Y. Lee, D. Psychoudakis, C.-C. Chen, and J.L. Volakis. Channel decomposition method for designing body-worn antenna diversity systems. *IEEE Transactions on Antennas and Propagation*, 59(1):254–262, 2011. 7.3

[195] M. Hiebel. *Fundamentals of Vector Network Analysis.* Rohde & Schwarz, 2007. 7.5

[196] C.A. Balanis. *Antenna Theory: Analysis and Design.* Wiley, 2012. 7.5

[197] I. Khan, P.S. Hall, A.A. Serra, A.R. Guraliuc, and P. Nepa. Diversity performance analysis for on-body communication channels at 2.45 GHz. *IEEE Transactions on Antennas and Propagation*, 57(4):956–963, 2009. 8.2

[198] A. Brizzi, A. Pellegrini, and Y. Hao. Design of a cylindrical resonant cavity antenna for BAN applications at V band. In *2012 IEEE International Workshop on Antenna Technology (iWAT)*, pages 152–155, 2012. 8.2

[199] P.R. Grajek, B. Schoenlinner, and G.M. Rebeiz. A 24-GHz high-gain Yagi-Uda antenna array. *IEEE Transactions on Antennas and Propagation*, 52(5):1257–1261, 2004. 8.3

[200] RT duroid 5880 high frequency laminates data sheet. `http://www.rogerscorp.com/documents/606/acm/RT-duroid-5870-5880-Data-Sheet.pdf`. [Online; accessed 27-June-2013]. 8.3, 8.4

[201] W.R. Deal, N. Kaneda, J. Sor, Y. Qian, and T. Itoh. A new quasi-Yagi antenna for planar active antenna arrays. *IEEE Transactions on Microwave Theory and Techniques*, 48(6):910–918, 2000. 8.3

[202] D.L. Sengupta. On uniform and linearly tapered long Yagi antennas. *IRE Transactions on Antennas and Propagation*, 8(1):11–17, 1960. 8.3

[203] K.C. Gupta. *Microstrip Lines and Slotlines*. The Artech House Microwave Library. Artech House, Incorporated, 1996. 8.3

[204] M. Bozzi, L. Perregrini, K. Wu, and P. Arcioni. Current and future research trends in substrate integrated waveguide technology. *Radioengineering*, 18(2):201–209, 2009. 8.4

[205] N. Rais, P.J. Soh, F. Malek, S. Ahmad, N. Hashim, and P.S. Hall. A review of wearable antenna. In *2009 Loughborough Antennas Propagation Conference (LAPC)*, pages 225–228, 2009. 8.5.1

[206] K.W. Kim and Y. Rahmat-Samii. Directional handset antennas and human head at Ka-band: Importance of skin layer. In *1998 IEEE Antennas and Propagation Society International Symposium*, volume 1, pages 122–125 vol.1, 1998. 8.5.1

[207] A. Hadjem, D. Lautru, C. Dale, M.-F. Wong, V.F. Hanna, and J. Wiart. Study of specific absorption rate (SAR) induced in two child head models and in adult heads using mobile phones. *IEEE Transactions on Microwave Theory and Techniques*, 53(1):4–11, 2005. 8.5.1

[208] N. Chahat, M. Zhadobov, L. Le Coq, and R. Sauleau. Wearable endfire textile antenna for on-body communications at 60 GHz. *IEEE Antennas and Wireless Propagation Letters*, 11:799–802, 2012. 8.5.1

[209] N. Chahat, M. Zhadobov, L. Le Coq, S.I. Alekseev, and R. Sauleau. Characterization of the interactions between a 60-GHz antenna and the human body in an off-body scenario. *IEEE Transactions on Antennas and Propagation*, 60(12):5958–5965, 2012. 8.5.1

[210] N. Chahat, M. Zhadobov, and R. Sauleau. Broadband tissue-equivalent phantom for BAN applications at millimeter waves. *IEEE Transactions on Microwave Theory and Techniques*, 60(7):2259–2266, 2012. 8.5.1

[211] J. Butler and R. Lowe. Beam-forming matrix simplifies design of electronically scanned antennas. *Electronic Design*, 9:170–173, 1961. 9.2

[212] C.-H. Tseng, C.-J. Chen, and T.-H. Chu. A low-cost 60-GHz switched-beam patch antenna array with Butler matrix network. *IEEE Antennas and Wireless Propagation Letters*, 7:432–435, 2008. 9.2

[213] M. Danielsen and R. Jorgensen. Frequency scanning microstrip antennas. *IEEE Transactions on Antennas and Propagation*, 27(2):146–150, 1979. 9.3

[214] J.L. Volakis. *Antenna Engineering Handbook, Fourth Edition*. McGraw-Hill, 2007. 9.3.1

[215] K. Sakakibara, J. Hirokawa, M. Ando, and N. Goto. A linearly-polarized slotted waveguide array using reflection-cancelling slot pairs. *IEICE transactions on communications*, 77(4):511–518, apr 1994. 9.3.2

[216] K. Wu, D. Deslandes, and Y. Cassivi. The substrate integrated circuits - a new concept for high-frequency electronics and optoelectronics. In *6th International Conference on Telecommunications in Modern Satellite, Cable and Broadcasting Service*, volume 1, pages P–III–P–X vol.1, 2003. B.1

[217] D. Deslandes and K. Wu. Design consideration and performance analysis of substrate integrated waveguide components. In *32nd European Microwave Conference*, pages 1–4, 2002. B

[218] Y. Cassivi, L. Perregrini, P. Arcioni, M. Bressan, K. Wu, and G. Conciauro. Dispersion characteristics of substrate integrated rectangular waveguide. *IEEE Microwave and Wireless Components Letters*, 12(9):333–335, 2002. B

[219] D. Deslandes and K. Wu. Integrated transition of coplanar to rectangular waveguides. In *2001 IEEE MTT-S International Microwave Symposium Digest*, volume 2, pages 619–622 vol.2, 2001. B